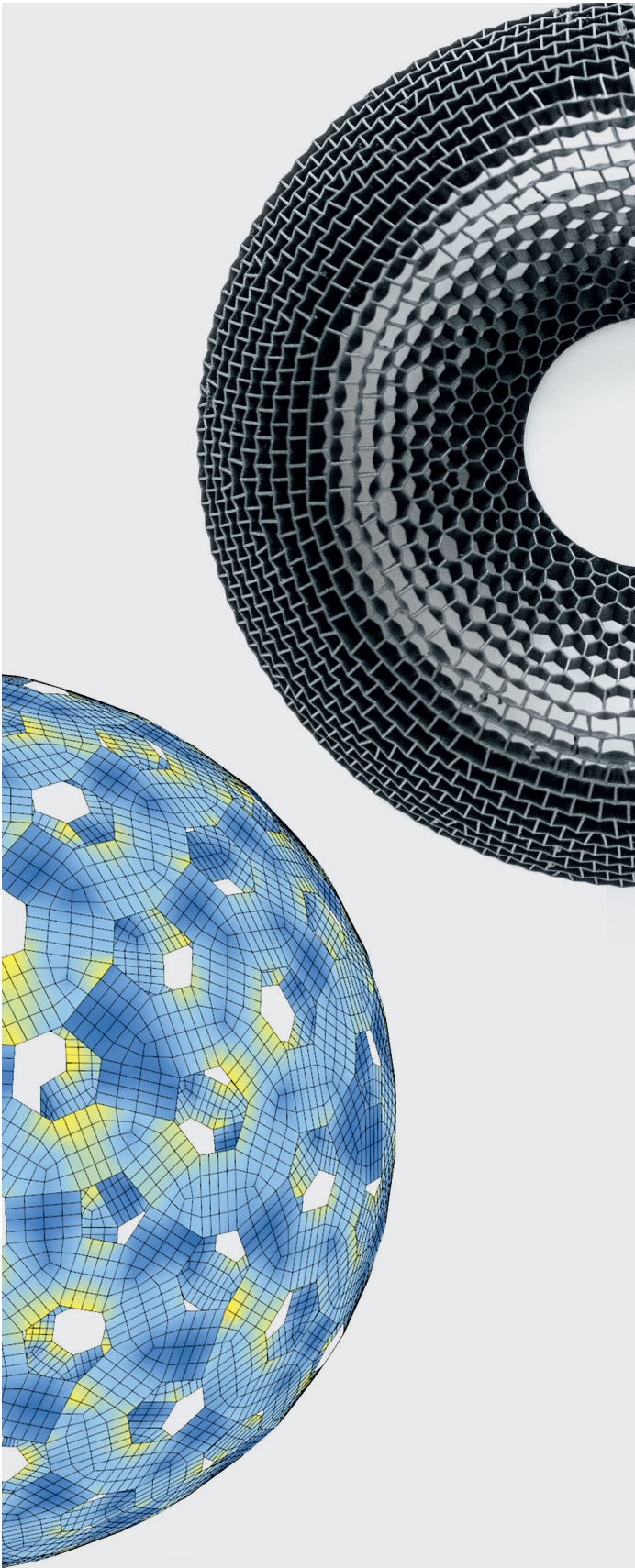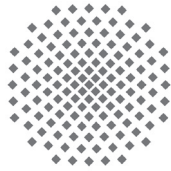itke   Universität Stuttgart Forschungsberichte

Riccardo La Magna

Bending-Active Plates

Strategies for the Induction of Curvature
through the Means of Elastic Bending
of Plate-based Structures.

Forschungsberichte itke

aus dem Institut für Tragkonstruktionen
und Konstruktives Entwerfen,
Universität Stuttgart

Herausgeber:
Professor Dr.-Ing. Jan Knippers

Bending-Active Plates

Strategies for the induction of curvature through the means
of elastic bending of plate-based structures

Von der Fakultät Architektur und Stadtplanung der Universität Stuttgart
zur Erlangung der Würde eines Doktor-Ingenieurs
(Dr.-Ing.) genehmigte Abhandlung

Vorgelegt von
Riccardo La Magna
aus Verona

Hauptberichter: Prof. Dr.-Ing. Jan Knippers
Mitberichter: Prof. Dr.-Ing. Christoph Gengnagel

Tag der mündlichen Prüfung: 21. Juni 2017

Institut für Tragkonstruktionen und Konstruktives Entwerfen der
Universität Stuttgart, 2017

Acknowledgements

This thesis is the result of my research work developed over the years at the Institute of Building Structures and Structural Design of the University of Stuttgart.

In the first place, I would like to sincerely thank my supervisor and head of the ITKE Prof. Dr.-Ing. Jan Knippers. My biggest gratitude goes to him for having given me the opportunity to be part of his team and believing in my work until the very end. His support and insight have been invaluable throughout the years. The development of this thesis has only been made possible by the positive culture of freedom and experimentation of the Institute. In this sense, I am glad and proud that this work "fits very well within the ITKE", as once expressed by him.

To my co-advisor, Prof. Dr.-Ing Christoph Gengnagel, I would like to extend my gratitude for having invested his time to review and correct my thesis. I've enjoyed many fruitful conversations and interesting discussions with him which have helped me to improve my work and focus on the most critical aspects of it.

This work would not have been possible without the financial support of the DAAD scholarship program. Special thanks also go to Pier 9 for providing the tools, spaces, expertise and a great time in San Francisco.

Thank you to my family and especially mom and dad for believing in me and having supported me for all these years. You've always given me the best feedback and motivation to go further. A big thank you also to Carola Plappert who has helped me so much during the development of my work. Her patience, support and skills have played an important role in the development of this thesis.

I would like to thank all my colleagues and friends at the University of Stuttgart for these amazing years together. In particular my colleagues of ITKE from day one Julian Lienhard, Amin Li, Simon Schleicher, Frédéric Waimer and, more recently, Axel Körner and Daniel Sonntag with whom I've shared great moments and many conversations. I wish to extend my gratitude also to former students Nicola Haberbosch and Andreas Schönbrunner for helping with the development of the first ideas and prototypes. Finally, a big thank you to all of my ITKE family. It's been a great journey!

Zusammenfassung

Biegeaktiv beschreibt eine Reihe von Tragwerksystemen, deren Formen durch gezielte Bauteilverformungen erzeugt werden. Bei dieser neuartigen Konstruktionsweise ist es von Bedeutung die Geometrie und Tragfunktion der Systeme gemeinsam zu betrachten. Das Ziel der Arbeit ist das konstruktive und architektonische Gestaltungspotenzial biegeaktiver Strukturen zu erforschen und gängige Tragwerksklassifizierungen um eine neue Kategorie zu erweitern.

Der Schwerpunkt dieser Arbeit liegt dabei auf biegeaktiven Konstruktionen, die flächige Bauteilen verwenden und nicht wie in vorangegangenen Studien aus verformten Stäben und Latten zusammengesetzt sind. Auf Grund dieser Eigenschaft lassen sich die hier vorgestellten Beispiele und Prototypen der besonderen Kategorie der biegeaktiven Plattenkonstruktionen zuweisen.

Das erste Kapitel der Arbeit geht daher auf das allgemeine Thema der biegeaktiven Tragsysteme und deren Klassifizierung ein. Einleitend werden dazu jüngst gebaute Projekte vorgestellt und der Rahmen des Forschungsvorhabens genauer eingegrenzt. In den folgenden Kapiteln werden die theoretischen Grundlagen zur Geometrie und des mechanischen Verhaltens von Flächen- und Plattenstrukturen im Detail diskutiert. Diese duale und sich ergänzende Betrachtung ist dabei ein notwendiger Schritt zum besseren Verständnis der grundsätzlichen Verformbarkeit von flächigen Bauteilen und die sich daraus ergebenen Gestaltungsmöglichkeiten.

Das darauf folgende Kapitel befasst sich mit der ersten Designstrategie die im Rahmen dieser Arbeit erforscht wurde. Hierbei handelt es sich um die sogenannte *form conversion*, bei der ein direkter Zusammenhang zwischen ursprünglicher Fläche und deren Unterteilung in biegeaktive Bauteile besteht. Um diesen Ansatz genauer zu beschreiben werden eine Reihe von Prototypen präsentiert, die mit dieser Technik entworfen und gebaut wurden. Zusammenfassend werden die geometrische und mechanische Eigenschaften der so entstandenen Strukturen diskutiert.

Im nächsten Kapitel wird die zweite Designstrategie vorgestellt, die sogenannte *embedded approach*. Hierbei werden grundsätzliche Verformungseigenschaften von explizit gestalteten Materialmustern zu Nutze gemacht, um gebogene Strukturen zu erstellen. Prototypen erläutern diesen Ansatz und zeigen mögliche Designpotenziale.

Die Arbeit endet mit einer kritischen Auseinandersetzung mit den hier vorgestellten Methoden zur Gestaltung biegeaktiver Tragstrukturen und diskutiert mögliche Entwicklungen für die zukünftige Forschung.

Abstract

Commonly referred to as *bending-active*, the term has come to describe a wide variety of systems that employ the large deformation of their constituent components as a primary shape-forming strategy. It is generally impossible to separate the structure from its geometry, and this is even more true for bending-active systems.

Placed at the intersection between geometry, design and engineering, the principle objective of this thesis is to develop an understanding of the structural and architectural potential of bending-active systems beyond the established typologies which have been investigated so far. The main focus is set on systems that make use of surface-like elements as principle building blocks, as opposed to previous and existing projects that predominantly employed linear components such as rods and laths. This property places the analysed test cases and developed prototypes within a specific category of bending-active systems known as bending-active plate structures.

The first chapters serve as a general introduction to the topic. An overview of relevant recent projects is presented in the introduction, followed by a discussion on the scope of research on bending-active structures. The following chapters lay the theoretical basis in terms of geometry of surfaces and mechanical behaviour of plates. This dual and complementary description serves as the necessary background to understand the limits and potential associated to the deformability of plate elements.

The following chapter delves into the first of the two strategies developed as part of this research. Termed *form conversion*, this approach establishes a one-to-one relationship between the initial base surface and its bending-active counterpart. The chapter proceeds with the presentation of a series of full-scale prototypes that were realised to test the validity of the form conversion approach. Geometrical and mechanical features are discussed in the conclusion of the chapter.

The second developed method, named *embedded approach*, is presented in the next section. This approach takes advantage of the inherent deformation properties of explicitly designed material patterns. The description of the method is followed by the presentation and discussion of the prototypes chosen to test the embedded approach.

Finally, the thesis concludes with a critical discussion of the presented methods and a reflection on potential developments for future research.

Contents

1. Introduction

The tight correlation between form and structure is sublimely condensed in the research on bending-active systems. By deriving shape through a process of form finding, an inseparable relationship between geometry and structure is achieved. These dual aspects are deeply rooted in the foundations of engineering and architecture, and provide the fundamental and mutually complementary knowledge for the understanding of structures as physical manifestations of built geometries.

Geometry plays a leading role in the load bearing and kinetic mechanism of any type of structure, whether manmade or found in nature. The study of structures that owe their shape to the elastic behaviour of their constituent elements requires an even greater understanding of such underlying principles. In this sense, elasticity and geometry are tightly connected and form a coherent and consistent body of knowledge on which the scientific framework of this research is based upon.

1.1   Motivation

The recent rise of new simulation paradigms and computational tools has lately sparked a renewed interest in engineering and architectural systems that employ form-finding as a shape-forming strategy. The term bending-active has been specifically coined to describe a wide range of systems that employ bending, and in general large deformations, as a means to induce form and structural qualities. Although the underlying mechanical principles are very well understood, a comprehensive overview of the structural and formal potential of bending-active structures is still open to exploration.

The relationship between geometry and structure is particularly relevant in the case of elastically formed systems, as it is the limits of the material which dictate the global design of the system rather than the other way round. Formfinding represents the main strategy to successfully design structural systems that take advantage of the deformation properties of materials. As a consequence, bending-active structures shift the design paradigm from a top-down to a bottom-up approach. This process-based approach requires a detailed understanding of the behaviour of the system in all its parts, and lies at the very foundation of form-finding as a building strategy employed in engineering and architecture.

For this very reason it is crucial to develop a thorough understanding of the mechanisms involved in the elastic deformation of building components in order to be able to create better performing structures compliant with the mechanical limits of materials.

In the light of these arguments, the current work aims at expanding the knowledge on bending-active structures through a series of built prototypes accompanied by simulations and their results. The methods of analysis are quite varied, and draw from different disciplines to develop a comprehensive understanding of the topic. Building on analytical principles of geometry and mechanics, the rapid increase in complexity required the introduction of numerical simulations to capture salient features otherwise impossible to study and analyse.

The main aspects which motivated the development of this work emerge from considerations on previous research conducted in the field and the associated developed prototypes. The most prominent examples of bending-active structures realised so far mainly made use of linear elements, where the end geometry was the result of a form-finding process performed on physical prototypes or digital models. Focusing on these aspects, two ideas can be identified as the main drivers of this research: the extension of bending-active structures to surface-like elements and the induction of Gaussian curvature through the means of elastic bending as the result of a prescribed geometry. In the quest of expanding the formal potential of bending-active structures, this work contributes by elucidating the mechanical implications of inextensible deformations and by suggesting new ways of employing bending as a shape giving strategy.

1.2   Research objectives

The principle objective of this thesis is to develop an understanding of the structural and architectural potential of bending-active systems beyond the established typologies which have been investigated so far. In particular, the main focus is set on structural systems that make use of surface-like elements as principle building blocks, as opposed to previous and existing projects that predominantly employed linear components as rods and laths. This aspect places the analysed test cases and developed prototypes within a specific category of bending-active systems which will be referred to as bending-active plate structures to draw a distinction from other more general terminology.

As opposed to membranes, plates possess a non-vanishing bending-stiffness. This strongly reduces the formability potential of plates which can only undergo restricted modes of deformation. Although limited in terms of achievable geometric configurations, this property of plates makes it easier to predict and control the final shape of the bent elements. Exploiting this aspect, it becomes possible to impose a predefined target shape to the system, rather than obtaining a structure which is the outcome of a form-finding process which involves no or very little shape control on behalf of the designer. Due to this peculiar characteristic, the test cases and prototypes developed in this research are meant to explore both the structural behaviour of elastically bent systems but also their shape forming potential. For the test cases, double curved geometries have been privileged as they pose non-trivial challenges to their construction, and especially for the renewed interest in building complex freeform surfaces which has risen recently. Double curved structures are particularly attractive for architects and engineers as they offer large expressive freedom in terms of design but also higher stiffness emerging from intrinsic geometric properties. Despite such appealing aspects, the complexity associated to the planning, engineering and manufacturing of double curved structures strongly reduced their application in the building industry by privileging standardised and cheap alternatives. The intrinsic characteristic of bending-active systems to assume complex shapes starting from initially flat and inexpensive configurations make them particularly attractive to overcome these limitations and infuse more life in the research of shell structures.

Within the broader question of assessing the shape forming potential of bending systems, an important aspect of this research focuses on the analysis of the mechanical behaviour of the structures. A fundamental question is how does the bending process affect the load bearing capacity of the structure and how can this be quantified. Due to the inherent limitations on the formability of plates, a series of strategies have been developed to expand the range of achievable geometries. These strategies have a non-negligible effect on the behaviour of the structure, as they approximate the starting shape into discrete elements which locally undergo bending. Throughout this strategy a discrete and discontinuous version of the initial surface is obtained. The discrete shell imposes force flows that deviate from the expected behaviour of its continuous shell counterpart. Scope of this research will also be to highlight in which ways the operations of discretization and bending globally affect the behaviour of the shell.

1.3 Methodology

Considering the importance of validating theoretical results with experimental results, this thesis does not make any exception. The results emerging from extensive simulations of the investigated phenomena have been thoroughly tested through a series of prototypes meant to validate the potential exposed in the theoretical work conducted here. The current work presents an extensive body of simulations which have served as main driver to test the developed ideas. The implementation of simulation technology within the design process is becoming more and more common practice, especially due to the larger availability of dedicated software and to new approaches which are making this integration more agile and intuitive. As a strong focus of this work is set on the validation between digital and physical, to achieve the maximum degree of confidentiality in the produced results all the simulations presented were run using the Finite Element Method. Despite spread accordance in the scientific community on the general validity of Finite Elements, their use within the design process still suffers implementation flaws which often derive from old legacy code which does not bind well with modern design packages and poor interoperability capacity. Regardless of these evident limits, the use of Finite Element technology was still deemed the most appropriate choice for the further development of the work. In order to overcome these limitations, extensive effort was required to create dedicated code libraries to enable a better and seamless communication between design and simulation packages.

The combination of theoretical background, analytical principles, simulation technology and physical prototyping mutually support the arguments developed in this research, and have been treated as a uniform body of work rather than distinct aspects independent from one another. This approach directly reflects the nature of research on bending-active structures, where the theory is generally validated through numerical testing and finally assessed by building prototypes. The topics discussed in the first three introductory chapters are meant to define the theoretical framework of this research, highlighting the most important aspects that capture the limits and potentials of the structural systems object of discussion. This first part of the work paves the way to the second part which will specifically focus on the devised generative methods which are the main objective of the research conducted here. The methods are presented describing the developed work pipeline and its application to freeform geometries. The description of these methods is accompanied by the presentation of the built prototypes along with discussions on the

form-finding and the structural performance of the objects. The work of this thesis is organised in the following chapters:

Chapter 2 is devoted to describing the general context of the research. An introduction about the topic and previous work is presented, highlighting the historical context, the benchmark constructions and the state of the art in terms of design approaches. Fundamental aspects regarding the limitations of the design methods adopted so far are discussed. This chapter serves as introduction to the topic and outlines the framework of the research.

Given the tight correlation of the treated topic to geometry, chapter 3 provides the fundamental concepts that guide the general scope of this work. The central concept of curvature will be discussed in its classical form, which assumes everywhere a continuous and differentiable surface, and also in its discrete form for discontinuous, locally non-differentiable manifolds. This distinction arises from the very nature of the Finite Element Method which requires a discrete version of its continuous, real counterpart. To fill the gap between simulation results and geometric information it was therefore deemed necessary to implement alternative methods of geometry analysis. In this chapter an important result from differential geometry will be discussed which traces a link between bending, strain and curvature. In a slightly different form and following different arguments, the same result will be derived in the next chapter on the mechanical behaviour of plates.

In chapter 4 an overview of the main mechanical principles of bending-active structures is introduced. The linear and non-linear theory of plates is presented discussing the main difference between bending and membrane strain. Owing to the richer nature of the non-linear theory of plates, the results seen in the chapter devoted to the differential geometry of surfaces will be derived anew, this time following arguments directly from mechanics. This extraordinary correspondence between geometry and mechanics demonstrates how tightly interconnected these two disciplines are, and will serve as a main driver for the development of the following topics discussed here. The chapter continues by drawing a distinction on the different modes of deformation which may be employed in the form-finding process of bending-active structures. In particular, bending and torsional actions will be analysed for the case of plate structures and their effects on the global geometry explained. This overview is accompanied by a thorough explanation of the setup adopted for the simulations contained in the thesis.

The following chapters are devoted to the elaborated strategies developed for the construction of bending-active surfaces. Chapter 5 presents the form conversion strategy for plate structures. The main geometric principles for the conversion of any arbitrary shape are introduced and explained. The implications deriving from the process of form conversion are presented accompanied by a series of numerical simulations meant to clarify the structural role of the bending and torsional deformation of the elements. These theoretical aspects are accompanied by the presentation of the prototypes which were built to test the presented ideas. The exposition follows the methodology of parallel presentation of the numerical results along with the built prototypes to draw conclusions on the validity of the simulations and the construction approach.

Chapter 6 concludes the discussion on shape forming strategies by introducing the embedded approach developed as part of this research. As opposed to the previous method, the embedded approach takes advantage of the inherent mechanical properties of certain classes of cellular structures. These enhanced properties have been exploited to conduct a series of experiments on the intrinsic shape-shifting capabilities of these structures. The prototypes built for testing the embedded approach are discussed along with a brief introduction on employed materials and adopted printing technology. The simulation results are again presented in parallel to validate the experimental results and gain insight on the complex deformation mechanisms involved.

Finally, in chapter 7 conclusions are drawn from the above research regarding the design, analysis and behaviour of bending-active plate structures and reviews the theoretical, methodological, and technological contributions of this work. This final chapter also aims to sketch an outline of future work and research to be conducted in the field. In doing so, this chapter does not attempt to be a concluding summary, but rather a starting point and invitation for future scholars to contribute to the topic in their own way.

2. Background

The development of architectural and structural systems runs in parallel with the technological advancements of each historical period. New materials have constantly changed the dominant paradigms of the way of building throughout history. Mankind has witnessed the shift from stone and wood architecture, to the birth of concrete and steel in the 19th century, up to contemporary fibre-reinforced polymers and smart materials yet to come. Advanced manufacturing techniques have steadily propelled the production of new materials and triggered their adoption in the building industry. The development of new materials has been constantly accompanied by novel and more refined theories meant to explain the mechanical principles of the load-bearing behaviour of structures and their related phenomena. These complementary aspects of technological advancement and theoretical description have been the main drivers of the major changes that occurred in architecture and engineering since the need of mankind to build and provide shelter.

The search for larger and lighter structures has been a recurring mantra in the history of building engineering. Refined mechanical and mathematical models have been the main instrument to draft, design, plan and build since the early studies of Galileo Galilei on the behaviour of the cantilever beam (Fig. 2.1) [Galilei 1638]. With deeper understanding of the principles of structural behaviour, greater freedom in planning could be achieved thanks to an improvement of the adopted predictive models. In this way, engineers have been able to experiment and push the boundaries of the existing structural typologies. In 1675 English scientist Robert Hooke discovers the relationship between arches and hanging chains (Fig. 2.2), which he summarises in his famous *"ut pendet continuum flexile, sic habit contiguum rigidum inversum"*, which translates to "as hangs the flexible line, so but inverted will stand the rigid arch" [Heyman 1998]. Both the hanging chain and the arch must be in equilibrium, and the forces are simply reversed [Block et al. 2006]. The realisation of the interplay between geometry, material and mechanics would have an enormous impact on the understanding of structures and the further development of new structural typologies in the times to come.

From Hooke's idea of the inverted catenary, a renewed understanding of the influence of form over structure rapidly developed. The introduction of advanced methods for the

FIG. 2.1

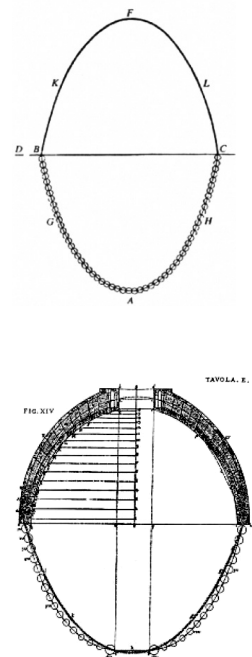Galileo Galilei's sketch for the study of the cantilever beam

FIG. 2.2

Poleni's sketch of Hooke's analogy between an arch and a hanging chain and his analysis of the Dome of Saint Peter's in Rome (1748)

FIG. 2.3

Antoni Gaudí's hanging chain model for the stone Church of Colònia Güell (1898)

FIG. 2.4

Heinz Isler, Autobahnraststätte Deitingen-Süd (1968)

FIG. 2.5

Frei Otto, Multihalle Mannheim (1974)

equilibrium analysis of structural systems, spanning from graphic statics to the theory of elasticity, enormously improved the array of tools available to engineers to plan and predict the behaviour of structures. Despite rapid advances in the theory of structures, the overwhelming complexity of the underlying mathematical framework (often involving the solution of higher order partial differential equations) effectively hindered the adoption of analytical methods for the definition of optimal structural forms. To overcome such limitations, the determination of optimal structural forms has historically been pursued through the aid of physical models up until recently. The key passage of Hooke's quote *"as hangs the flexible line [...]"* contains the essence of this method, which relies on empirical observations of the physical behaviour of idealised structural models. The procedure of designing structures based directly on the material response of a scaled model is commonly referred to as *form-finding*.

Form-finding is the process of finding an 'optimal' geometry of a structure which is in static equilibrium with a design loading [Adriaenssens 2014]. This process has been mainly employed for the design and construction of compressive shells and tensile membrane structures. Antoni Gaudí is famously noted for using natural, hanging chains for the determination of the shape of his masterpieces (Fig. 2.3). In more recent years, membrane and shell structures pioneers like Heinz Isler (Fig. 2.4), Frei Otto (Fig. 2.5) and Felix Candela, often derived the shape of their designs from model-based form-finding processes or using pure geometrical approaches [Chilton and Isler 2000, Otto 2005, Garlock and Billington 2008]. However, the practical and intellectual complexity which can be recognised in seminal works like the Multihalle Mannheim [Happold and Liddell 1975], noticeably reduced the chances of realisation to a selected number of individuals devoted to this type of experimentation and research. Until recently, the lack of more accessible engineering and simulation tools has strongly inhibited the adoption of this approach.

In recent years, a new wave of freeform architectural projects was largely prompted by the wider availability of tools for the design community. This has sparked research in engineering and architecture to find better, although often coarse solutions for the construction of complex freeform geometries. In most cases, the complexity of the design would overrule the natural integration between form and structure, often relying exclusively on the strength of material to carry loads rather than attempting to achieve a good structural design. Despite this initial enthusiasm for freeform architectures, a renewed sensibility towards form and material is making the design community reconsider the role of structural design.

New tools are providing a fresh awareness of structures as a fundamental aspect of design. In this sense the research on bending-active structures fully captures the zeitgeist of the moment, condensing form, structure, material and analysis into one, holistic approach.

2.1   Definition of bending-active structures

With the rise of new simulation methods and computational tools, a new generation of architects and engineers is getting more interested in form-finding strategies for architectural and structural systems. The key motivation of this approach is to determine a force equilibrium to generate and stabilise a structure by its own geometry. While the membrane and shell structures of pioneers like Frei Otto, Heinz Isler, and Felix Candela were often derived from model based and physical form-finding, today's structures often arise from advanced digital simulations and the integration of material behaviour within the form-finding process [Menges 2012].

A good example for the new possibilities emerging from a physically informed digital design process is the research on bending-active structures. Bending-active describes a wide range of structural systems that employ large deformations as a form giving and self-stabilizing strategy [Lienhard 2014]. These systems use the elastic deformation of planar, off-the-shelf building materials to generate structures emerging from the combination of curved elements [Knippers et al. 2011]. While the traditional maxim in engineering is to limit the amount of bending in structures, this typology actually harnesses bending for the creation of complex and extremely lightweight designs.

Many aspects qualify a structure as bending-active, the large elastic deformation of its constituent elements being the most prominent and the main constraint for a proper design. To maintain the strain within the elastic limits of the material, the building elements must be necessarily thin and slender, making this type of structures extremely lightweight. The requirement of thin cross-sections is opposed by the necessity of withstanding external loads to be considered structurally efficient. This inherent contradiction is at the heart of bending-active systems, which need to counterbalance the drastic reduction of available material by employing alternative measures. The answer to this lies in the geometric configuration of the structure, as different assemblies have a major influence on the global behaviour of the system. Geometry is therefore the fundamental aspect for the correct design of bending-active structures.

Mudhif houses

2.2 Historical overview

The first examples of bending-active structures are to be found in various types of vernacular architecture constructions. Traditional hut and shelter making techniques typically employ elastically bent elements for the construction of curved arches and shell structures (Fig. 2.6). The adoption of elastically formed elements for construction purposes is here mainly motivated by economic reasons and fabrication constraints. This category of structures adopts an intuitive use of bending for the erection process and relies only on hands-on experience regarding the deformation behaviour of the used building elements [Lienhard et al. 2013]. These represent the most basic and elementary examples of structures actively employing the elastic deformation of materials.

A real impulse in the research on bending-active structures emerged at the beginning of the second half of the last century. Buckminster Fuller was one of the first to embrace the idea of exploiting the elastic properties of materials to build geometry driven shapes with architectural potential. As part of his studies on geodesic domes, noteworthy in this context are his Plydome experiments. At the time of Fuller's development a complete description of the mechanical behaviour and material constraints of these structural systems did not follow, and his ideas were rather approached following a purely geometric, but nonetheless rigorous methodology. Further context and information on his work will be provided in the following chapter.

On the flow of renewed interest for research on structural geometry, starting around 1960 Frei Otto introduced fundamental concepts that would radically change the established ideas of design, engineering and architecture. His material oriented approach to architecture and the introduction of form-finding as a design tool have had long lasting consequences on the way architecture is produced. The main intellectual contribution of his work is embodied in the paradigm shift that goes from a top-down design approach to a process based one. It is the material that informs the structure and its geometry. In this way the design is not imposed on the material but is rather the outcome of the interaction between material, geometry and boundary conditions. A substantial number of experiments were conducted by Otto on elastic gridshells. Unlike geometry imposed gridshells, elastic gridshells employ the elastic deformation of rods or laths during the erection process to achieve form. In 1974 the Multihalle Mannheim, the first large span gridshell was completed by Frei Otto in collaboration with Buro Happold as engineering consultant. Tapping into the great knowledge on physical form-finding and photogrammetric survey of Otto's team, the geometry of the gridshell

was entirely form-found using hanging chain models (Fig. 2.7). The computational power and simulation knowledge at that time was still not advanced enough to allow such a complex project to be solved numerically in a reasonable way. Following the seminal experience of the Multihalle, many other notable gridshells have been built in the following decades, providing the perfect platform to test new ideas and theories for the numerical simulation of large elastic deformations.

Besides several built gridshells and active research in the field, not many other prominent typologies exploiting bending as the main form-giving strategy have been developed lately. An exception can be found in several bamboo architectures which have emerged in the last years as part of a rediscovery of the excellent building qualities of this natural material. In most cases though, the achieved geometries are the result of a simple superposition and connection of linear elements bent along one axis. This has mainly led to the construction of rotationally symmetric, donut-like shapes employing the linear bamboo rods to form a structural grid. Much more effort has been invested in the engineering and mechanical research of the material's properties. Nonetheless, the built examples display remarkable architectural qualities and considerable spans.

The advent of new simulation strategies and the wider availability of tools has lately sparked much interest around bending-active structures within the research community. Arguably, the strongest impulse on the topic has come from research projects developed within academic contexts in recent years. Several projects have been realised in the form of small and medium scale pavilions to test materials and tools which have emerged and are being currently developed in academia and outside the academic environment. It is also not a coincidence that the term bending-active itself originated recently within the research framework of former colleague Dr. Julian Lienhard at the Institute of Building Structures and Structural Design (ITKE) of the University of Stuttgart to describe this specific class of structures. Despite the speculative nature of the projects, these studies have served as perfect test cases to investigate new and disruptive ideas and technologies which might have the potential to be scaled up to fully functional structural typologies. Finally, the introduction of powerful computational models in the design workflow is enabling explorations previously strongly limited by the complexity of the task.

An overview of relevant projects will be presented in the upcoming section. Following the well-established tradition of disclaiming that a complete overview of past and existing projects is utterly impossible, the few projects reviewed next have been chosen for their impact on the topic treated here.
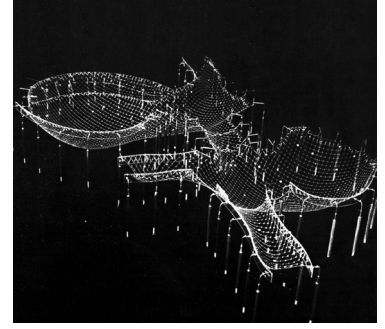

FIG. 2.7

Frei Otto, hanging chain model for the Multihalle Mannheim

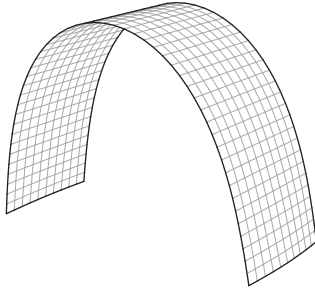ICD/ITKE Research Pavilion 2010

The ICD/ITKE 2010 Pavilion exclusively employs pure bending as a form-giving strategy

2.2.1 ICD/ITKE Research Pavilion 2010

The ICD/ITKE Research Pavilion 2010 features a radial arrangement of 6.5 mm birch plywood strips, coupled together to form a series of self-equilibrating system of arches that form a 10 m wide torus (Fig. 2.8). To lock kinematic modes potentially occurring along the line of contact between the strips, the location of the connection points between the elements shift vertically along the structure. The double curved global shape of the pavilion is achieved through a process of discretization following the radial direction of the torus. In this way, the single bent strips approximate the global surface and restore the continuity of the structure [Lienhard et al. 2011].

The pavilion makes use of thin, long strips which behave more similarly to flat plates rather than one-dimensional rods. This conferred to the pavilion its characteristic full surface appearance as opposed to the typical aesthetics of gridshells. The width of the strips is largely sufficient to guarantee enough rotational inertia orthogonally to the plane of the strip, therefore privileging one axis as the main direction of bending. The layout of the structure and the geometry of the strips exclusively induce pure bending in the elements (Fig. 2.9). No other actions are recognizable in the actuation method. Specifically, the elements undergo cylindrical bending, as the local deformed geometry can be assimilated to portions of cylinders with varying radii. The stress state arising in the strips is only deriving from the bending, and is therefore directly proportional to the local bending radius and the thickness of the strip. Despite the simple mode of actuation, the global geometry, the varying bending radii and the connection details between the strips made the ICD/ITKE 2010 Research Pavilion the first prototype to relaunch a widespread interest in the research for bending-active plate-based structures.

2.2.2 Thematic Pavilion Expo 2012

For the Expo 2012 in Yeosu, South Korea, the architecture
office soma realised the main thematic pavilion "Ocean One".
The central highlight of this building is its kinetic facade with
108 individually steerable lamellas (Fig. 2.10). The lamellas
are part of an adaptive facade system that controls the solar
exposure of the building during daytime and provides kinetic
effects for the public in the exterior. The office Knippers Hel-
big Advanced Engineering developed the technical concept
and structural planning for this facade. The facade has a total
length of 140 m and is designed to withstand very high wind
loads up to 35 m/s at the Korean coast [Knippers et al. 2012].

      The final lamella concept is a single curved plate, sup-
ported by two hinged corners at the top and the bottom. On
the adjacent corners two servomotors apply a compressive
force which leads to a linear displacement of the corner points
and to a controlled buckling deformation. The 108 elastically
deformable lamellas were hand-laminated out of GFRP and
ranged in length between 3 m and 14 m. Apart from an edge
stiffener to limit deformations, the lamellas required a thick-
ness of only 9 mm to comply with the high structural needs.
Despite being single curved, the lamellas behave similarly to
flat plates as their cylindrical geometry is isometric to a plane.
The lateral buckling effect derives from the eccentric actua-
tion of the elements, which induces a combined bending and
torsional deformation mechanism in the lamellas (Fig. 2.11).
This combined action allows to achieve apertures between the
lamellas, which in their deformed state deviate considerably
from the section of a cylinder. To the knowledge of the author,
this is one of the first examples of bending-active structures
that actively employs bending and torsion as principal actuat-
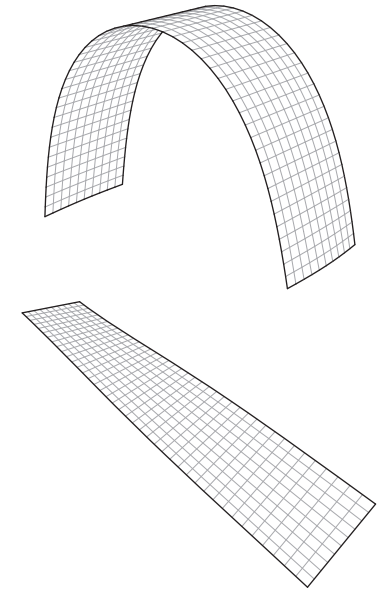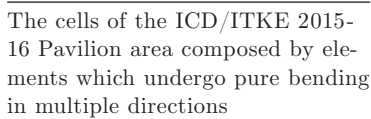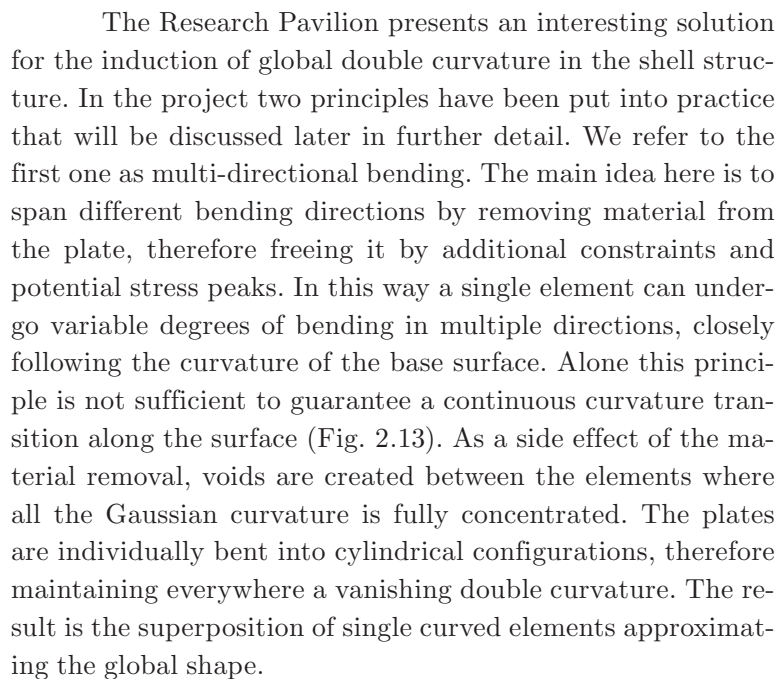ing mechanism.

FIG. 2.12

ICD/ITKE Research Pavilion
2015-16

2.2.3 ICD/ITKE Research Pavilion 2015-2016

For the ICD/ITKE Research Pavilion 2015-16 a singular fabrication technique was developed which enabled the production of elastically bent, double-layered segments made from custom-laminated, beech plywood. The building elements consist of thin wood strips custom-laminated so that the grain direction and thickness corresponds with the differentiated stiffness required to form parts with varying radii. Therefore, the initially planar strips can be elastically bent to find the specific shape embedded in the laminate. The pavilion consists of 151 segments that were prefabricated by robotic sewing (Fig. 2.12). Each of them is made out of three individually laminated beech plywood strips. The entire structure covers an area of 85 m² and spans 9.3 meters [Bechert et al. 2016].

  The Research Pavilion presents an interesting solution for the induction of global double curvature in the shell structure. In the project two principles have been put into practice that will be discussed later in further detail. We refer to the first one as multi-directional bending. The main idea here is to span different bending directions by removing material from the plate, therefore freeing it by additional constraints and potential stress peaks. In this way a single element can undergo variable degrees of bending in multiple directions, closely following the curvature of the base surface. Alone this principle is not sufficient to guarantee a continuous curvature transition along the surface (Fig. 2.13). As a side effect of the material removal, voids are created between the elements where all the Gaussian curvature is fully concentrated. The plates are individually bent into cylindrical configurations, therefore maintaining everywhere a vanishing double curvature. The result is the superposition of single curved elements approximating the global shape.

FIG. 2.13

The cells of the ICD/ITKE 2015-16 Pavilion area composed by elements which undergo pure bending in multiple directions

14

2.3 Design approaches to bending-active structures

Bending-active structures are often designed by following either a behaviour-based, geometry-based, or integral approach [Lienhard et al. 2013]. While the first category refers to a traditional, intuitive use of bending, the latter two categories describe a more scientific take on the design of bending-active structures. Here, experimental, analytical and numerical form-finding techniques are employed to inform and drive the design process.

2.3.1 Behaviour based approach

Bending is used intuitively during the construction process and relies exclusively on hands-on experience regarding the deformation behaviour of the used building material. Limited knowledge on the material's behaviour and no structured design process is involved in this type of method. This is the most basic design approach for the creation of bending-active structures. For references see the previously mentioned examples found in vernacular architecture.

2.3.2 Geometry based approach

The system's geometry is predefined on analytical geometry or experimental form-finding methods. Both these aspects are employed to approximate and control the actual bending geometry. Material limitations are considered analytically and are mostly based on simplified assumptions such as the moment-curvature relationships. One example of bending-active structures which follows a geometry-based design approach is Buckminster Fuller's Plydome [Fuller 1959]. This construction principle is based on approximating the basic geometry of a sphere with a regular polyhedron. Its edges and angles are then used to arrange multiple plates into a spatial tiling pattern, which is fastened together by bending the plates at their corners (Fig. 2.14). The resulting structure is made out of identical plates that were joined together by placing bolts at predefined positions. Even though this technique allowed Fuller to construct a double-curved spherical shape out of initially planar and then single-curved plates, this methodology also had several shortcomings. First and foremost, it is limited to basic polyhedral shapes. Only due to the repetitive angles was it possible to use identical plates, something which would be impossible in the case of a freeform surface due to the changing curvatures along the surface. Furthermore, at his time Fuller was forced to compute the needed overlap of the plates and the exact position of the pre-drilled holes mathematically. The only way to calibrate this data was by producing Plydomes in series and improving the details over time.
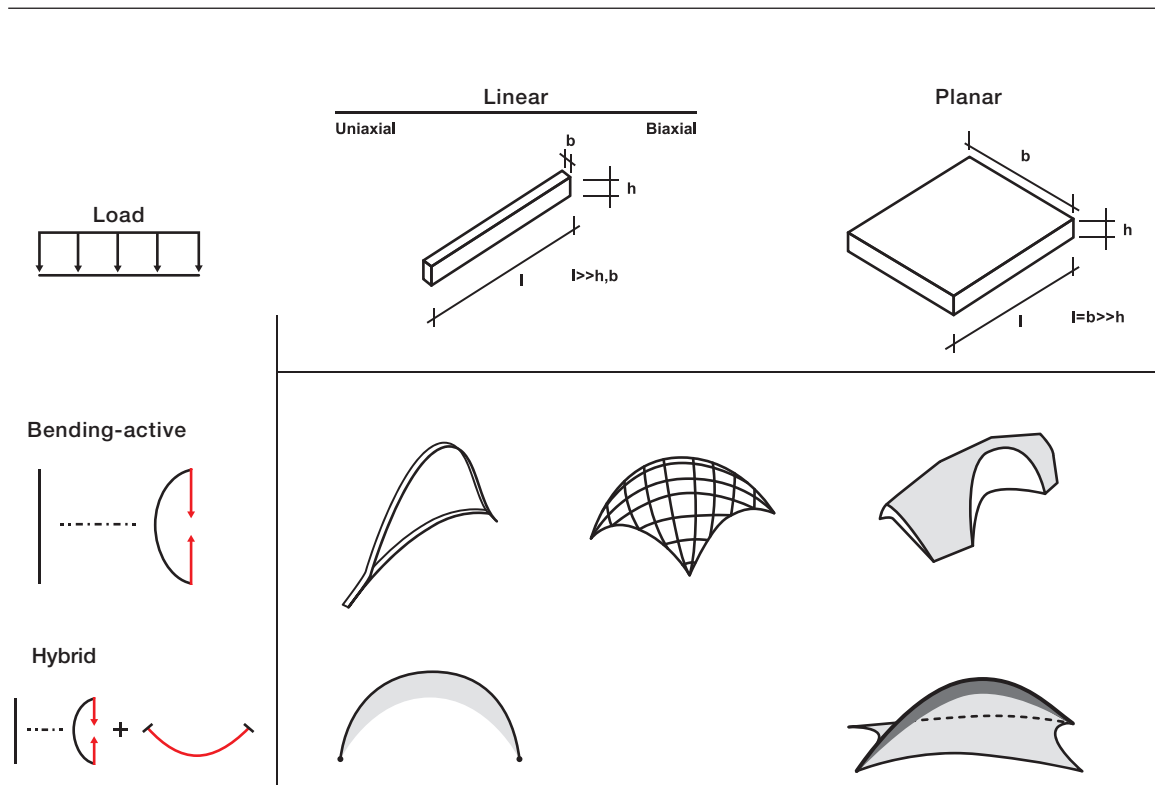

FIG. 2.14

Buckminster Fuller, Plydome (1957)

2.3.3 Integral approach

The elastic bending deformation is analysed through numerical form-finding, which enables full control of material behaviour based geometry. Material characteristics and limitations are included in the numerical analysis model. Compared to that, following an integral design approach for bending-active plate structures provides more flexibility and renders the opportunity for computational automation. The 2010 ICD/ITKE Research Pavilion (Fig. 2.8) is one prominent example of this approach. As characteristic for an integrative approach, the project started with intensive laboratory testing to better understand the limiting material behaviour of the used plywood. The results of these physical experiments were then integrated as constraints into parametric design tools and used to calibrate Finite-Element simulations. Synchronizing physical and digital studies ensured that the form-finding techniques provided an accurate description of the actual material behaviour while at the same time giving more feedback on the resulting geometry of the structure. This project even went so far to re-create the actual bending process by simulating the deformation of every strip into a cross-connected and elastically pre-stressed system [Lienhard et al. 2012].

While the last project is definitely innovative, it should be pointed out that the integral approach was used here mainly in a bottom-up way and thus narrowed the possible design space. For the future development of bending-active plate structures it may be desirable to prioritise a top-down approach, which gives more weight to the target geometry and thus more freedom to the designer. However, the key challenge remains and boils down to the question of how to assess both the global shape as well as the local features of the constituent parts for structures in which geometrical characteristics and material properties are inevitably linked together and similarly affect the result. For this purpose two new approaches have been developed in the framework of this research with the aim of approximating the target surface as close as possible. The first approach has been termed *form conversion*, as a one-to-one correspondence exists between the target surface and the bending-active approximation. This exclusively top-down method delivers a very close duplicate of the original surface, and the outcome is completely predictable. The second approach was named *embedded approach*, as it makes use of the inherent properties of certain classes of cellular structures to assume shapes otherwise counterintuitive. The outcome of the embedded approach is not as easily predictable and results need to be validated through form-finding.

Load · Linear (Uniaxial / Biaxial) · Planar

b, h, l>>h,b — b, h, l=b>>h

Bending-active

Hybrid

2.4 Classification of bending-active structures

Bending-active structures can be categorised following different principles. The first criteria of classification refers to the type of structural elements used. In Fig. 2.15 from [Knippers et al. 2011] a division between bending-active and hybrid systems is drawn. Pure bending-active systems exclusively employ flexible elements that can withstand very large deformations without incurring in failure before reaching their final structural configuration. Such elements possess a moderate to low bending stiffness in order to allow the deformation process to take place. Along the line of this distinction, the other typology that can be identified within the family of bending-active structure are the so-called hybrid structures. Unlike pure bending-active, hybrid structures combine the structural qualities of bending elements together with the stabilising effects of restraining membrane elements. The idea of hybrid structures traces back to antiquity and has seen growing interest and application in recent prototypes and research structures.

An alternative way to classify bending-active structures is by geometric properties. By categorising Bending-Active systems depending on the geometrical dimension of their constituent elements, it is possible to distinguish between 1D and 2D systems. Rods and elastic gridshells typically belong to the first category, whilst plate structures to the latter. Structural systems that achieve form and stability through the elastic deformation of thin plates fall into the category of

bending-active plate structures. The most prominent example can be found in Buckminster-Fuller's 1957 Plydome and more examples have been emerging recently. Plate-dominant bending-active structures have not yet received much attention and are generally considered difficult to design. One reason is that plates have a limited formability since they deform mainly along the axis of weakest inertia and thus cannot easily be forced into complex geometries. Although less investigated and put into practice, undergoing research and a series of recent prototypes have been exploring the structural and form inducing potential of bending-active plate structures. The main objective of this research is focused on bending-active plate structures and plate-based structural elements and the devised strategies to induce curvature in these systems.

The central difference between 1D and 2D structural elements relies on the deformation space that each one of these can trace. Considering a linear element like a slender beam, the bending can occur along both y and z axis, where x is aligned with the main axis of the beam and y and z forming an orthonormal frame of reference. In this way we define bending as the rotation along the non-aligned axes of the beam. Rotation along the x axis produces torsion in the element. In the case of non-circular cross-sections, torsional effects can have a major contribution on the form-giving process, providing multiple planes of alignment in space. The ability of spanning such a large configuration space is due to the fact that the bending stiffness of a straight beam is generally of comparable magnitude in both y and z directions. The same is true for the torsional stiffness and the torsional effects, as they are of similar nature as the bending actions. For a beam or a rod the strongest direction is the longitudinal one, i.e. axial effects aligned with the x axis will exclusively produce tension or compression over the full cross-section of the element.

In the case of bi-dimensional thin elements as a sheet of flexible material, the geometrical situation is slightly different. In comparison to the slender beam discussed previously, a plate is defined as a structural element in which two dimensions are much larger than the third one. It is usual to term the two large dimensions as width and length, and the smaller one as thickness. We place an external frame of reference with x and y aligned with length and width and z with the thickness of the plate so to uniquely define the normal of the surface. We first consider plate-like elements with length bigger than width but both much larger than thickness. These elements are commonly referred to as strips. In the case of a strip the allowable kinematics are rotations around the x and y axis. Similarly to rods we call these actions torsion and bending. We explicitly omit rotations around the z axis, as in this

case the moment of inertia around z is way higher with respect to the other two. This assumption does not imply that bending around the z axis cannot occur, but rather that for the purpose of bending-active structures the degree of deformation is not appreciable enough to be actively exploited. Rigorous arguments on the allowed kinematics will be provided in the next chapter. We finally consider the case of plates with similar length and width but thickness much smaller compared to the previous two. The kinematics here reduce to only bending around the x and y axis, as rotation around the z axis and torsional effects around the x and y directions can be disregarded in the context of large deformations. It is necessary to specify that the bending deformations for a plate in x and y are almost mutually exclusive. This means that for a plate element, bending can only occur in one of the two directions and not both at the same time. The reason for this is that attempting to bend a plate in two directions will induce a non-sustainable stress state in the material, eventually leading to its failure. For the purposes of bending-active structures then, a plate element behaves just as a strip element and no practical distinction can be drawn between the two. A comparison between the deformation spaces of both elements highlights how limited the formability potential of plates is. It is therefore no wonder that until now rods have been primarily favoured against plates.

The classification presented here highlights fundamental qualities of the building elements and their suitability to be employed as bending-active elements. From this brief introduction on the allowable kinematics of each geometric category, different typologies can be derived. Slender rods possess the highest degrees of freedom and kinematic capabilities, which makes them apt for applications where the geometric variations of the structure are more pronounced. Generally speaking, sharp changes in Gaussian curvature can be more easily achieved through rod systems, typically elastic gridshells or similar. It is therefore not a coincidence that the structural system of Otto's Multihalle Mannheim was conceived as a gridshell, partly due to the geometric complexity of the building itself. The reduced kinematics of strips obviously has a detrimental effect on the formability of the elements. With only two axes of rotation allowed, the spanned space is severely limited, and thus the geometric diversity. On the other hand, the limitations deriving from the reduced kinematic space have a direct effect on the control over the global form, as the deformation process is more easily predictable. The formal freedom sacrificed in the choice of building element is therefore recovered on the side of enhanced shape control.

2.5   Materials for bending-active structures

To be suitable for bending-active structures, a material needs to display a series of specific qualities. In particular, the relationship between stiffness and maximum allowable stress is a relevant measure of how adequate a material is for bending-active purposes. We recall here Ashby's diagrams which provide a handy and direct feedback to identify material classes (Fig. 2.16). In the diagrams are depicted fields in the material property-space and sub-fields by individual materials. Search regions introduced in his work outline areas in the diagrams which identify materials fit for a certain application.

Based on previous work by Lienhard et al. [Lienhard 2014] and experience conducted in the course of development of this work, the most suitable type of materials for bending-active structures falls in between the area marked with the dashed lines in Ashby's diagrams. The most common materials which have been employed so far in the research on bending-active structures are normally wood, plywood and GFRP. The materials contained in this category have in common characteristics of high flexural strength and moderate stiffness. High flexural strength is in general a sought quality for any kind of building material. In the context of bending-active structures though, it acquires even higher relevance as the mechanical reserves of the material are already used for the form-finding process. This means that for tight radii, and consequently high bending stress, the material might already reach a high degree of utilisation, leaving a reduced margin of material reserve available. Depending on the characteristics of elements, material, geometry and additional side factors, up to 60% utilisation of the material might be reached under form-finding. Wood and GFRPs are known to be susceptible to long lasting creeping effects, especially in combination with high strain and deformations which is typically the case of bending-active structures. Despite being a fundamental aspect for the proper design of bending-active structures, creeping effects and their influence on the global structural behaviour are not considered in the further development of this work. It is nonetheless advised to continue the research on the topic in order to develop fundamental knowledge for the further advancement of bending-active structural systems.

Concerning the characteristic of moderate flexural stiffness, this quality is partially motivated by the ease of formability of the material. This aspect is particularly relevant when considering the erection process of such systems. High material stiffness means higher energy needs to be input in the system to reach the desired deformation. Besides large spanning gridshells which have been commonly erected with the
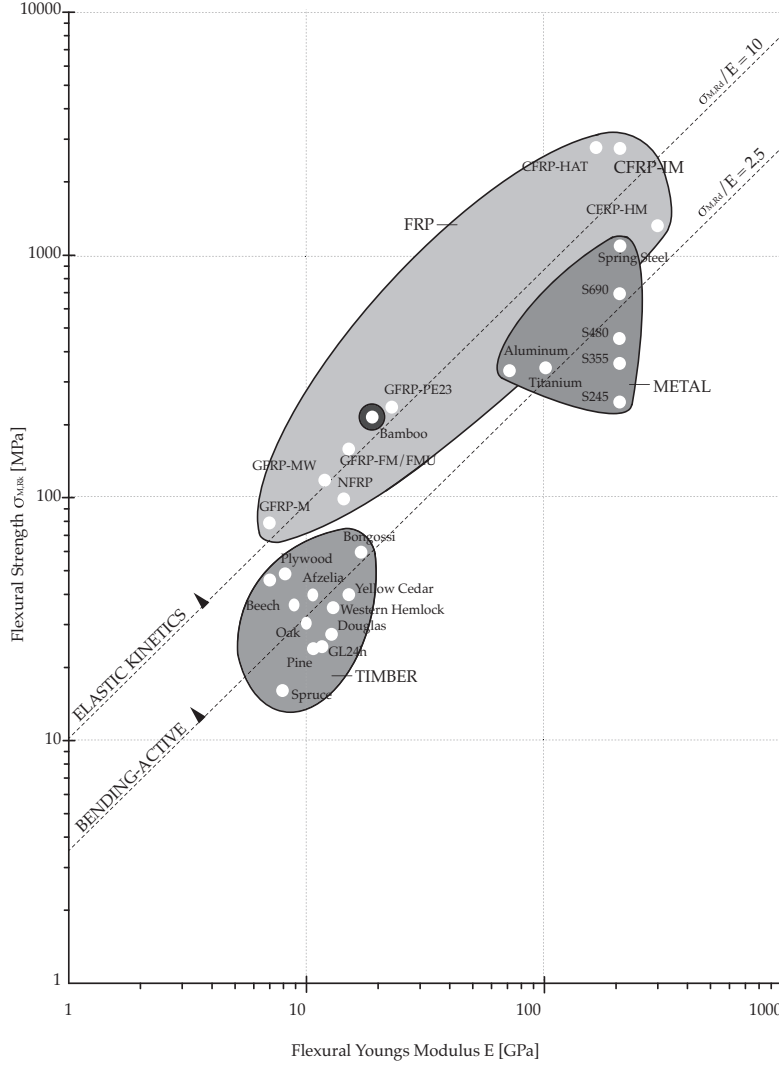
FIG. 2.16

Ratio of strength $\sigma_{M,RK}$ [MPa] to stiffness E [GPa] of common building materials (from Lienhard 2014)

Flexural Strength $\sigma_{M,R}$ [MPa]

Flexural Youngs Modulus E [GPa]

$\sigma_{M,RK}/E = 10$

$\sigma_{M,RK}/E = 2.5$

CFRP-HAT CFRP-IM
CFRP-HM
FRP
Spring Steel
S690
S480
Aluminum S355
Titanium METAL
S245
GFRP-PE23
Bamboo
GFRP-MW GFRP-FM/FMU
NFRP
GFRP-M
Bongossi
Plywood
Afzelia Yellow Cedar
Beech Western Hemlock
Oak Douglas
Pine GL24h
Spruce TIMBER

ELASTIC KINETICS
BENDING-ACTIVE

aid of a crane or a boom by lifting the grid and then forcing the sides into place, most bending-active research projects realised so far have primarily made use of manual labour for the erection process, often in the form of teams of motivated students. It is therefore clear that under these circumstances the least amount of effort that needs to be input to build the system is highly appreciated. This is also a defining aspect of bending-active structures, which make use of planar, easily formable sheets of material to achieve structural equilibrium. Not being able to easily form the building elements would in a way defeat one of the main purposes these structures were first conceived for. The central problem arising from using materials with low to moderate Young's modulus is obviously the reduction in global stiffness of the outcome structure. This is for sure the inherent controversy of the nature of bending-active structures: to be able to undergo large deformations the elements need to be slender or soft enough to not reach a critical state under form-finding, but to fulfil its goal

the global structure needs to withstand general loading conditions. Unfortunately this is a complicated conundrum difficult to solve. This intrinsic contradiction is partially resolved by a delicate balance of material characteristics and structural qualities, letting the geometry do the work of tying all these aspects together and providing structural capacity. In a way it can be said that it is geometry that does all the work. This statement will become clearer in the following chapters and in relationship to the prototypes that build up the core case studies of this thesis.

To conclude this paragraph a remark on the applicability of Ashby's diagram. For typical architectural scale applications wood, plywood and GFRPs have been identified as the most suitable materials due to a perfect ratio between flexural strength and material stiffness. For architectural prototypes the bending radii are normally in the range of 5 m to 30 m. For these values GFRP and wood are appropriate and deliver a good compromise between formability and strength. Considering smaller curvatures, and therefore larger bending radii (being curvature the inverse of the osculating circle at the point), softer materials might become more suitable for the purpose as the bending stresses after form-finding will be way lower. The same reasoning applies to smaller systems, at the scale of which the tight curvatures required may render impossible the realisation through the commonly used materials.

3. Differential geometry

3.1 Differential geometry of continuous surfaces

Differential geometry is the study of curved objects in space. These include, amongst others, curves and surfaces embedded in a 3-dimensional Euclidean space, which is also the framework that elasticity and this research fall into. In this chapter we will focus on a few, fundamental properties of surfaces, as curves are beyond the scope of this work. It might seem counterintuitive to introduce concepts of differential geometry to study flat surfaces, however, this chapter shall clarify the key ideas necessary to establish the behaviour and the structural possibilities associated with planar elements and their combination.

The following paragraphs pursue the excellent introduction to differential geometry contained in [Williams 2014]. Other great texts exist on the topic, some to be praised for their simple and intuitive approach [Pressley 2012] and others specifically focusing on the underlying mathematics [Struik 1988]. Classical books on differential geometry typically follow the analytical derivation of Gauss, but do not establish the modern tensor notation. The decision of following [Williams 2014] is motivated by the clear and concise exposition of the topic, and also by the use of the tensor notation introduced in the book's chapter devoted to differential geometry. As in the words of the author, the tensor notation is used "mainly because [...] it is ideal for writing structural equations as well as geometric relationships" [Williams 2014]. The advantage of using the tensor notation essentially lies in the elegant and concise way the fundamental quantities of surfaces are derived.

The topics discussed in this chapter are meant to clarify intrinsic properties of surfaces that will be employed in the upcoming sections. A direct connection to the mechanics of plates will be discussed in the following chapter. Nonetheless, it is interesting to notice how the same concepts can be treated from a pure geometrical perspective, but also emerge as a consequence of the mechanical description of plates. Remarks on the extension of these properties to discrete surfaces will close the exposition of this chapter. The development of the following sections on classical differential geometry was made possible by the precious insight provided by Dr. Dragos Naicu.

3.1.1 Covariant and contravariant base vectors

A point on a surface can be written in parametric form as:

$$\mathbf{r}(u,v) = x(u,v)\mathbf{i} + y(u,v)\mathbf{j} + z(u,v)\mathbf{k}, \tag{3.1}$$

where u and v are the familiar surface parameters, and $\mathbf{i}$, $\mathbf{j}$ and $\mathbf{k}$ unit vectors oriented with the Cartesian coordinate axes x, y and z. Here bold roman letters are employed to indicate vectors.

Many texts use u and v as surface parameters, but for consistency with [Williams 2014] we introduce here a change in notation, where u is replaced by θ^1 and v by θ^2. Therefore (3.1) is rewritten as:

$$\mathbf{r}(\theta^1, \theta^2) = x(\theta^1, \theta^2)\mathbf{i} + y(\theta^1, \theta^2)\mathbf{j} + z(\theta^1, \theta^2)\mathbf{k}. \tag{3.2}$$

Note that this particular notation uses superscripts for the parameters, and does not mean θ raised to the power 1 or squared.

With θ^1 = constant, $\mathbf{r}$ creates a parametric curve on the surface. By varying the constant a family of curves is produced. In the same way when θ^2 is kept constant a second family is formed. The two families populate the surface with a net of parametric curves. For any point P on the surface two parametric curves are uniquely defined. In general, the two curves will not be perpendicular to each other. Nonetheless this curvilinear net of coordinates is a very simple and powerful way to determine lengths and angles on a surface, as well as changes of these quantities when the surface undergoes deformation.

In Fig. 3.1 a point P on a general surface is defined, as well as an arbitrary curve C lying on the surface and passing through P. The curve C is parametrised by the parameter u such that $\theta^1 = \theta^1(u)$ and $\theta^2 = \theta^2(u)$. Varying the parameter u, i.e. travelling along the curve C, leads to a change in θ^1 and θ^2 on the surface, which in turn means x, y and z vary in Cartesian coordinates.

Having parametrised the surface through the parameters θ^1 and θ^2, for each point on the surface the set of base vectors aligned with the parametric curves are called *covariant base vectors* and are given by:

$$\mathbf{g}_i = \frac{\partial \mathbf{r}}{\partial \theta^i} = \frac{\partial x}{\partial \theta^i}\mathbf{i} + \frac{\partial y}{\partial \theta^i}\mathbf{j} + \frac{\partial z}{\partial \theta^i}\mathbf{k}, \tag{3.3}$$

for i = 1 and j = 2. In general, $\mathbf{g}_1$ and $\mathbf{g}_2$ are neither unit vectors, nor are they perpendicular to each other. The covariant base vectors are aligned with tangent directions defined by the surface's parameterisation.
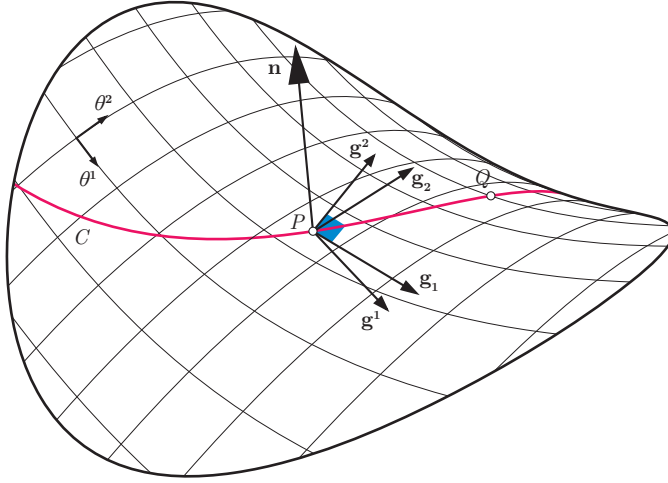
As the covariant base vectors $\mathbf{g}_1$ and $\mathbf{g}_2$ lie on the tangent plane to the point P, the unit normal to the surface $\mathbf{n}$ at P will be perpendicular to this plane and is defined through the normalised cross product between the two vectors:

$$\mathbf{n} = \frac{\mathbf{g}_1 \times \mathbf{g}_2}{|\mathbf{g}_1 \times \mathbf{g}_2|}. \tag{3.4}$$

It is also useful to introduce a second set of base vectors on the surface known as the *contravariant base vectors*, $\mathbf{g}_1$ and $\mathbf{g}_2$. These are denoted by superscripts, as opposed to the subscript notation for the covariant base vectors, and given by:

$$\mathbf{g}_i \cdot \mathbf{g}^j = \delta^i_j, \qquad \mathbf{g}^i \cdot \mathbf{n} = 0, \tag{3.5}$$

where the Kronecker delta is defined as:

$$\delta^i_j = \begin{cases} 1, & \text{if } i = j, \\ 0, & \text{if } i \neq j. \end{cases} \tag{3.6}$$

Here the dot denotes the usual scalar product between two vectors. It follows from (3.5) that $\mathbf{g}^1$ and $\mathbf{g}^2$ lie in the same plane as $\mathbf{g}_1$ and $\mathbf{g}_2$, i.e. the tangent plane, as the scalar product of the contravariant vectors with the surface normal returns a vanishing quantity. Also, $\mathbf{g}^1 \perp \mathbf{g}_2$ while $\mathbf{g}^2 \perp \mathbf{g}_1$ as a consequence of how the Kronecker delta is defined (Fig. 3.1). The magnitude of $\mathbf{g}^1$ is determined by $\mathbf{g}_1 \cdot \mathbf{g}^1 = 1$. The magnitude of $\mathbf{g}^2$ is determined in a similar way.

The metric tensor is a function which tells how to compute quantities on a surface independently from its specific parameterisation. Given a surface arbitrarily parameterised, the metric tensor allows to calculate quantities such as the distance between two points lying on the surface, the angle

between two vectors on the tangent plane and the area of portions of the surface. By taking the scalar products of the covariant base vectors, a set of scalar quantities known as the *covariant components* of the metric tensor is produced:

$$g_{ij} = g_{ji} = \mathbf{g}_i \cdot \mathbf{g}_j, \tag{3.7}$$

and the *contravariant components* of the metric tensor are retrieved analogously:

$$g^{ij} = g^{ji} = \mathbf{g}^i \cdot \mathbf{g}^j. \tag{3.8}$$

In the following sections the Einstein summation convention is used, which states that an index is summed if it is repeated in the same term as a subscript and superscript. A change between the covariant and the contravariant vectors is possible by using the components of the metric tensor. These are related in the following way:

$$\mathbf{g}^i = \sum_{j=1}^{2} \left(g^{ji} \mathbf{g}_j \right) = g^{ji} \mathbf{g}_j,$$
$$\mathbf{g}_i = \sum_{j=1}^{2} \left(g_{ji} \mathbf{g}^j \right) = g_{ji} \mathbf{g}^j. \tag{3.9}$$

Additionally, since the square of the magnitude of the expression $\mathbf{g}_1 \times \mathbf{g}_2$ is:

$$(\mathbf{g}_1 \times \mathbf{g}_2) \cdot (\mathbf{g}_1 \times \mathbf{g}_2) = (\mathbf{g}_1 \cdot \mathbf{g}_1)(\mathbf{g}_2 \cdot \mathbf{g}_2) - (\mathbf{g}_1 \cdot \mathbf{g}_2)^2 =$$
$$= g_{11} g_{22} - (g_{12})^2, \tag{3.10}$$

and by introducing the quantity $g = g_{11} g_{22} - (g_{12})^2$, the unit normal can be rewritten using the covariant components:

$$\mathbf{n} = \frac{\mathbf{g}_1 \times \mathbf{g}_2}{\sqrt{g}}. \tag{3.11}$$

Finally, by using the first relationship of (3.5) $g^{ij} g_{jk} = \delta_k{}^i$ [Williams 2014], the contravariant components can be found:

$$g^{11} = \frac{g_{22}}{g}, \qquad g^{12} = -\frac{g_{12}}{g}, \qquad g^{22} = \frac{g_{11}}{g}. \tag{3.12}$$
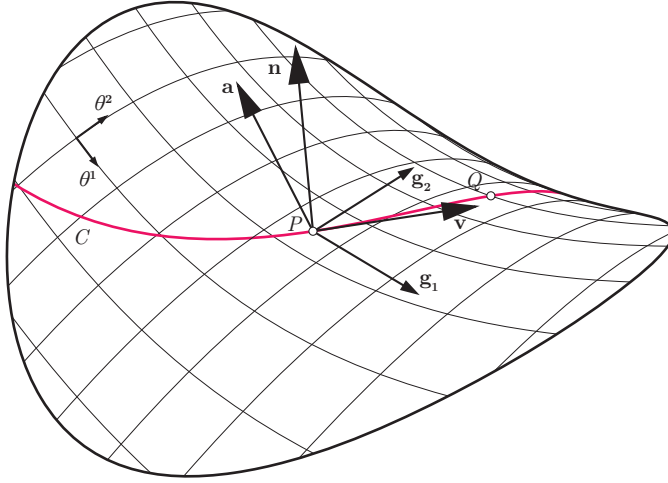
FIG. 3.2

Orthonormal frame on the surface at point P composed of vectors $\mathbf{a}$, $\mathbf{n}$ and $\mathbf{v}$ and covariant base vectors (adapted from [Williams 2014] and [Naicu 2016])

3.1.2 First fundamental form of surfaces

Fig. 3.2, shows only the covariant base vectors along with vectors $\mathbf{a}$, $\mathbf{n}$ and $\mathbf{v}$ at point P, with $\mathbf{a}$ and $\mathbf{v}$ yet to be defined. The vector tangent to curve C at point P is defined as:

$$\frac{d\mathbf{r}}{du} = \frac{\partial \mathbf{r}}{\partial \theta^1} \frac{d\theta^1}{du} + \frac{\partial \mathbf{r}}{\partial \theta^2} \frac{d\theta^2}{du} = \sum_{i=1}^{2} \mathbf{g}_i \frac{d\theta^i}{du}, \qquad (3.13)$$

or, by using the Einstein summation convention:

$$\frac{d\mathbf{r}}{du} = \mathbf{g}_i \frac{d\theta^i}{du}. \qquad (3.14)$$

The squared length of the infinitesimal line segment $PQ = \delta s$ which lies on the curve C can be calculated with:

$$\delta s^2 = \delta \mathbf{r} \cdot \delta \mathbf{r} = \sum^{2} \sum^{2} \left[\left(g_i \delta \theta^i \right) \cdot \left(g_j \delta \theta^j \right) \right], \qquad (3.15)$$

or, by using the Einstein summation convention:

$$\delta s^2 = \mathbf{g}_i \cdot \mathbf{g}_j \delta \theta^i \delta \theta^j = g_{ij} \delta \theta^i \delta \theta^j. \qquad (3.16)$$

(3.16) is known as the *first fundamental form*, and the scalar product coefficients $g_{ij} = g_{ji}$ are the *coefficients of the first fundamental form* also known as the *components of the metric tensor* [Williams 2014]. The first fundamental form completely describes the metric properties of a surface. Thus, it enables one to calculate the lengths of curves on the surface and the areas of regions on the surface. In literature it is very common to find the coefficients of the first fundamental form expressed as $g_{11} = E$, $g_{12} = g_{21} = F$, $g_{22} = G$ [Pressley 2012].

This follows the classic nomenclature adopted by Gauss himself. The use of indices reflects the modern tensor notation adopted here.

The unit tangent to the curve can now be calculated using the first fundamental form as following:

$$
\mathbf{v} = \frac{d\mathbf{r}}{ds} = \frac{d\mathbf{r}}{du}\frac{du}{ds} = \frac{\left(\dfrac{d\mathbf{r}}{du}\right)}{\left(\dfrac{ds}{du}\right)} = \frac{\mathbf{g}_i \dfrac{d\theta^i}{du}}{\sqrt{g_{jk}\dfrac{d\theta^j}{du}\dfrac{d\theta^k}{du}}}. \tag{3.17}
$$

A third unit vector $\mathbf{a}$, defined as $\mathbf{a} = \mathbf{n} \times \mathbf{v}$, together with $\mathbf{n}$ and $\mathbf{v}$ make a set of three mutually perpendicular unit vectors on the curve, but defined by making use exclusively of surface coordinates [Naicu 2016].

3.1.3 Second fundamental form of surfaces

Referring to Fig. 3.2, we now consider the curvature vector of the curve C at point P. Since $\mathbf{v}$ is the unit tangent vector of the curve at P, then:

$$
\kappa = \frac{d\mathbf{v}}{ds}, \tag{3.18}
$$

is the curvature vector. The curvature vector $\mathbf{\kappa}$ is perpendicular to $\mathbf{v}$ so that $\mathbf{v} \cdot \mathbf{\kappa} = 0$ and the magnitude of $\mathbf{\kappa}$ is equal to one over the radius of curvature of C. The curvature vector is decomposed into a normal component $\mathbf{\kappa}_{\text{normal}}$ and a geodesic component $\mathbf{\kappa}_{\text{geodesic}}$ so that $\mathbf{\kappa} = \mathbf{\kappa}_{\text{normal}} + \mathbf{\kappa}_{\text{geodesic}}$ [Pressley 2012]. The geodesic curvature is the curvature in the local tangent plane to the surface and the normal curvature is the curvature perpendicular to the surface. The normal curvature vector is in the direction of the surface normal at P so that:

$$
\mathbf{\kappa}_{normal} = \kappa_{normal}\mathbf{n}, \tag{3.19}
$$

where the quantity $\mathbf{\kappa}_{\text{normal}}$ is called the normal curvature. The normal curvature can be found from [Naicu 2016, Struik 1988]:

$$
\kappa_{normal} = -\frac{\delta\mathbf{r} \cdot \delta\mathbf{n}}{\delta\mathbf{r} \cdot \delta\mathbf{r}} = -\frac{b_{ij}\delta\theta^i\delta\theta^j}{g_{mn}\delta\theta^m\delta\theta^n}, \tag{3.20}
$$

where the following coefficients are introduced:

$$
b_{ij} = b_{ji} = \mathbf{n} \cdot \mathbf{g}_{i,j} = -\mathbf{n}_j \cdot \mathbf{g}_i. \tag{3.21}
$$
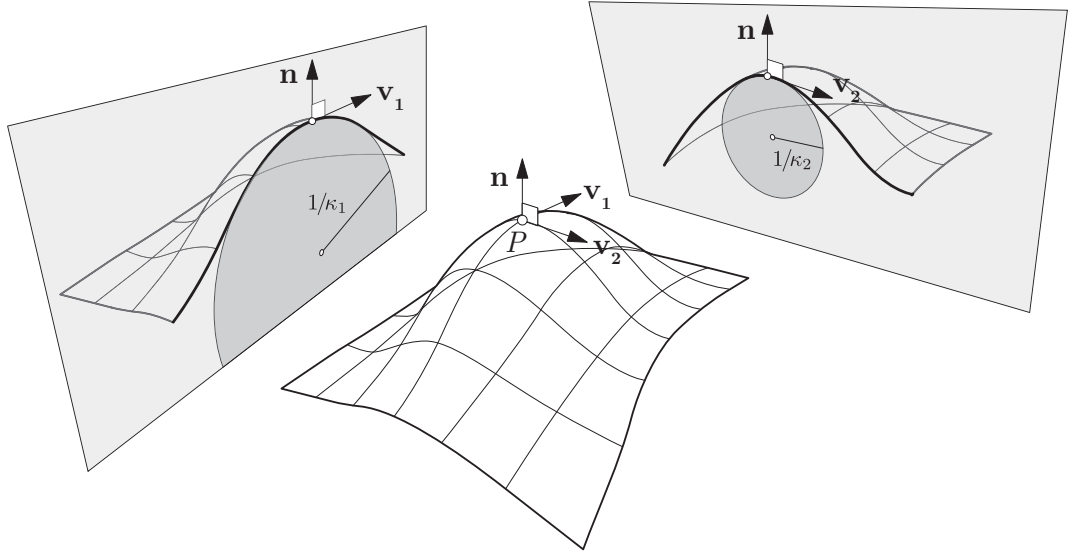
The enumerator in equation (3.20) is known as the *second fundamental form* and the quantities b_{ij} are called the *coefficients of the second fundamental form*. Together with the first fundamental form, it serves to define intrinsic invariants of the surface, for instance its principal curvatures. As for the coefficients of the first fundamental form, Gauss' classical notation makes use of the following: $b_{11} = L$, $b_{12} = b_{21} = M$, $b_{22} = N$ [Pressley 2012].

In conclusion, we derived the first and second fundamental forms on which a surface depends, which completely define the intrinsic geometrical properties of the surface:

$$
\begin{aligned}
I &= \delta\mathbf{r} \cdot \delta\mathbf{r} = g_{ij}\delta\theta^i\delta\theta^j, \\
II &= \delta\mathbf{r} \cdot \delta\mathbf{n} = -b_{ij}\delta\theta^i\delta\theta^j.
\end{aligned}
\tag{3.22}
$$

3.1.4   Curvature of continuous surfaces

The decomposition of the curvature vector $\boldsymbol{\kappa}$ leads to the normal curvature being defined in the direction of the surface normal $\mathbf{n}$, while the geodesic curvature lies in the local tangent plane to the surface at P. The normal curvature can be visualised in Fig. 3.3 Given a surface and a point P on it, there is an infinite number of planes perpendicular to the surface revolving around the normal vector $\mathbf{n}$ at point P. A natural question arising is whether there are privileged directions which define curvatures with special properties. These directions exist and are called the directions of principal curvature, and the two extremal normal curvatures, denoted by $\boldsymbol{\kappa}_1$ and $\boldsymbol{\kappa}_2$, corresponding to the aforementioned directions, are called principal curvatures (Fig. 3.3). The existence of principal curvature directions can be explained in the light of the *shape tensor* defined as following:

$$\mathbf{b} = b_{ij}\mathbf{g}^i\mathbf{g}^j. \tag{3.23}$$

The shape tensor $\mathbf{b}$ is a second-order symmetric tensor, and as such it behaves just like similar entities as the stress and strain tensors [Williams 2014]. For every second-order symmetric tensor a pair of eigenvalues and associated eigenvectors can be found by solving the roots of a quadratic relation known as secular equation. A fundamental property of a tensor's eigenvalues is that, of all possible values, they will always be the minimum and maximum. For the associated eigenvectors it can be proven that they will always form a pair of orthogonal directions.

The two eigenvalues are the roots of the quadratic which is written here in determinant form as:

$$\begin{vmatrix} (b_{11} - \kappa g_{11}) & (b_{12} - \kappa g_{12}) \\ (b_{12} - \kappa g_{12}) & (b_{22} - \kappa g_{22}) \end{vmatrix} = 0, \tag{3.24}$$

which can be expanded to:

$$\left(g_{11}g_{22} - (g_{12})^2\right)\kappa^2 - \left(g_{11}b_{22} - 2g_{12}b_{12} + g_{22}b_{11}\right)\kappa + \\ + \left(b_{11}b_{22} - (b_{12})^2\right). \tag{3.25}$$

The principal curvatures can be used to define fundamental properties of the surface. There are two particularly important ones which are useful in analysis and are derived as follows. The *mean curvature* defined as:

$$\kappa_H = \frac{\kappa_1 + \kappa_2}{2} = \frac{g_{11}b_{22} - 2g_{12}b_{12} + g_{22}b_{11}}{2\left(g_{11}g_{22} - (g_{12})^2\right)}, \tag{3.26}$$

and the *Gaussian curvature* is:

$$\kappa_G = \kappa_1\kappa_2 = \frac{b_{11}b_{22} - (b_{12})^2}{g_{11}g_{22} - (g_{12})^2}. \tag{3.27}$$

Minimal surfaces such as soap films have $H = 0$. Dome shapes, also known as synclastic surfaces have $K > 0$ whilst saddle surfaces, or anticlastic surfaces have $K < 0$. In the case of Gaussian curvature $K = 0$ a surface is known as a developable surface (Fig 3.4). The only surfaces that have a vanishing Gaussian curvature are the plane, cylinders and cones. It will be shown that these special classes of surfaces are intimately tied together.

3.1.5 Gauss' Theorema Egregium

We conclude this chapter by introducing Gauss's *Theorema Egregium*. *Egregium* is Latin for remarkable, as Gauss himself wrote. Gauss's Theorema is one of the most interesting and elegant results in the field of differential geometry, and it is of central importance in the discussion on the mechanics of plates and especially to understand the limits of their deformation.

We first introduce the Christoffel symbols of the first and second kind, which depend exclusively on the coefficients of the first fundamental form and their first derivatives:

$$
\begin{aligned}
\Gamma_{ijm} &= \mathbf{g}_m \cdot \mathbf{g}_{i,j} = \frac{1}{2}(g_{im,j} + g_{mj,i} - g_{ij,m}), \\
\Gamma_{ij}^k &= \Gamma_{ji}^k = \mathbf{g}^k \cdot \mathbf{g}_{i,j} = -\mathbf{g}_{,j}^k \cdot \mathbf{g}_i = g^{km}\Gamma_{ijm}.
\end{aligned}
\tag{3.28}
$$

The coefficients g_{ij} depend only on $\mathbf{g}_i$ and $\mathbf{g}_j$ while the coefficients b_{ij} also depend on the second derivatives $\mathbf{g}_{i,j}$ where the comma indicates derivation in accordance to the tensor notation adopted. Christoffel's symbols are properties of the coordinate system which describe how it bends and stretches along the surface. The three vectors $\mathbf{g}_1$ and $\mathbf{g}_2$ together with $\mathbf{n}$ constitute a moving trihedron, but in this case they are not mutually perpendicular nor are they all unit vectors.

By differentiating the covariant base we retrieve the change in the covariant vectors with respect to the parameters θ^1 and θ^2. Differentiation is expressed with a comma, thus leading to the so-called Gauss's equations [Struik 1988]:

$$
\begin{aligned}
\mathbf{g}_{1,1} &= \Gamma_{11}^1 \mathbf{g}_1 + \Gamma_{11}^2 \mathbf{g}_2 + b_{11}\mathbf{n}, \\
\mathbf{g}_{1,2} &= \Gamma_{12}^1 \mathbf{g}_1 + \Gamma_{12}^2 \mathbf{g}_2 + b_{12}\mathbf{n}, \\
\mathbf{g}_{2,2} &= \Gamma_{22}^1 \mathbf{g}_1 + \Gamma_{22}^2 \mathbf{g}_2 + b_{22}\mathbf{n}.
\end{aligned}
\tag{3.29}
$$

which using the summation convention can be rewritten as:

$$
\mathbf{g}_{i,j} = \frac{\partial^2 \mathbf{r}}{\partial \theta^i \partial \theta^j} = \Gamma_{ij}^k \mathbf{g}_k + b_{ij}\mathbf{n}.
\tag{3.30}
$$

We now compute the derivative of the Weingarten equations, $\mathbf{n}_{,i}$ which express the change in the normal vector with respect to the parameters θ^1 and θ^2 [Naicu 2016]:

$$
\begin{aligned}
\mathbf{n}_{,1} &= -b_1^1 \mathbf{g}_1 - b_1^2 \mathbf{g}_2, \\
\mathbf{n}_{,2} &= -b_2^1 \mathbf{g}_1 - b_2^2 \mathbf{g}_2, \qquad \text{with } b_j^i = g^{ik}b_{jk}.
\end{aligned}
\tag{3.31}
$$

or using Einstein's summation convention:

$$\mathbf{n}, i = -b_i^k \mathbf{g}_k. \tag{3.32}$$

By differentiating Gauss's equations once more, the compatibility conditions that ensure a surface fits together are obtained:

$$\begin{aligned}\mathbf{g}_{k,ij} =& \frac{1}{2}(g_{nk,ij} + g_{in,kj} - g_{ki,nj})\mathbf{g}^n + \\ &+ \Gamma_{kin}\mathbf{g}_{,j}^n + b_{ki,j}\mathbf{n} + b_{ki}\mathbf{n}_{,j},\end{aligned} \tag{3.33}$$

and by setting $\mathbf{g}_{k,ij} - \mathbf{g}_{k,ji} = 0$. This gives two expressions in terms of the three base vectors, $\mathbf{g}_1$, $\mathbf{g}_2$ and $\mathbf{n}$, which can always be satisfied only if the coefficients in front of the three base vectors are identically zero [Williams 2014]. Mathematically this is written as:

$$\begin{aligned}&\left(R_{ijkm} - (b_{ki}b_{jm} - b_{kj}b_{im})\right)\mathbf{g}^m + \\ &+ (b_{ki,j} + b_{jp}\Gamma_{ki}^p - (b_{kj,i} + b_{ip}\Gamma_{kj}^p))\mathbf{n} = 0,\end{aligned} \tag{3.34}$$

where:

$$\begin{aligned}R_{ijkm} =& \frac{1}{2}(g_{im,kj} + g_{kj,mi} - g_{ki,mj} - g_{jm,ki}) + \\ &+ g^{np}(\Gamma_{kjn}\Gamma_{mip} - \Gamma_{kin}\Gamma_{mjp}),\end{aligned} \tag{3.35}$$

are the components of the Riemann-Christoffel tensor. The compatibility conditions from the coefficients of the base vectors then lead to the two Mainardi-Codazzi equations:

$$b_{ki,j} + b_{jp}\Gamma_{ki}^p = b_{kj,i} + b_{ip}\Gamma_{kj}^p, \tag{3.36}$$

and to Gauss' Theorem:

$$R_{ijkm} = b_{ki}b_{jm} - b_{kj}b_{im}. \tag{3.37}$$

The Riemann-Christoffel tensor presents a number of symmetries which means that, in two dimensions, the only relevant term is explicitly:

$$\begin{aligned}R_{1212} =& \frac{1}{2}(2g_{12,12} - g_{11,22} - g_{22,11}) + \\ &+ g^{np}(\Gamma_{12n}\Gamma_{12p} - \Gamma_{11n}\Gamma_{22n}),\end{aligned} \tag{3.38}$$

and, upon further manipulation:

$$R_{1212} = b_{11}b_{22} - (b_{12})^2. \tag{3.39}$$

Finally, Gauss's Theorema Egregium can be rewritten as:

$$\kappa_G = \frac{R_{1212}}{g}. \tag{3.40}$$

This derivation demonstrates that the Gaussian curvature κ_G only depends on the coefficients of the first fundamental form, g_{ij}, and their derivatives. This is the essence of Gauss's Theorema Egregium, which implies that the Gaussian curvature of a surface is a bending invariant [Struik 1988]. The Gaussian curvature is an intrinsic property of the surface, as any property expressible in terms of bending invariants is called intrinsic. Deforming a surface without tearing, stretching or shrinking does not change the Gaussian curvature. And conversely, a change of Gaussian curvature can only be achieved by changing lengths on a surface.

3.1.6 Plane isometries

As seen in the previous chapter, the Thereoma Egregium states that the Gaussian curvature of a surface does not change if one bends the surface without stretching it. In modern mathematical language the theorem can be expressed by saying that the Gaussian curvature of a surface is *invariant under local isometry*. An isometry is a transformation which maintains distances and lengths on a surface unchanged, i.e. it is a distance-preserving transformation.

We are now interested in determining the isometric transformations of the plane. Recalling that the Gaussian curvature only depends on the first fundamental form, it can be concluded that all surfaces which have the same first fundamental form can be isometrically transformed into one another. Since the lengths of a curve on a surface are computed as the integral of the square root of the first fundamental form, it is plausible that the first fundamental form of the two surfaces should be the same [Pressley 2012]. A general plane is parameterised by the following:

$$\mathbf{r}(\theta^1, \theta^2) = \mathbf{a} + \theta^1 \mathbf{b} + \theta^2 \mathbf{c}, \tag{3.41}$$

with $\mathbf{b}$ perpendicular to $\mathbf{c}$. Differentiating with respect to θ^1 and θ^2 we obtain:

$$\begin{aligned} \mathbf{g_1} &= \frac{\partial \mathbf{r}}{\partial \theta^1} = \mathbf{b}, \\ \mathbf{g_2} &= \frac{\partial \mathbf{r}}{\partial \theta^2} = \mathbf{c}. \end{aligned} \tag{3.42}$$

Recalling relationship (3.7), the covariant components of the metric tensor of the parameterised plane are:

$$g_{11} = \mathbf{b} \cdot \mathbf{b} = ||\mathbf{b}||^2 = 1,$$
$$g_{12} = g_{21} = \mathbf{b} \cdot \mathbf{c} = 0, \qquad (3.43)$$
$$g_{22} = \mathbf{c} \cdot \mathbf{c} = ||\mathbf{c}||^2 = 1,$$

from which we can now calculate the first fundamental form of the plane. This reads:

$$I = d\theta^1 d\theta^1 + d\theta^2 d\theta^2 = (d\theta^1)^2 + (d\theta^2)^2, \qquad (3.44)$$

where $d\theta^1$ and $d\theta^2$ must not be confused as $d\theta$ to the power of one and two respectively.

A generalised cylinder is defined as any ruled surface spanned by a one-parameter family of parallel lines. An arbitrary curve γ is extruded along the direction $\mathbf{a}$. A parameterisation of the generalised cylinder therefore reads:

$$\mathbf{r}(\theta^1, \theta^2) = \boldsymbol{\gamma}(\theta)^1 + \theta^2 \mathbf{a}, \qquad (3.45)$$

and differentiating with respect to θ^1 and θ^2:

$$\mathbf{g_1} = \frac{\partial \mathbf{r}}{\partial \theta^1} = \dot{\boldsymbol{\gamma}},$$
$$\mathbf{g_2} = \frac{\partial \mathbf{r}}{\partial \theta^2} = \mathbf{a}. \qquad (3.46)$$

where we've denoted d/du by a dot. Assuming that γ is a unit speed curve [Pressley 2012], that $\mathbf{a}$ is a unit vector and that γ is contained in a plane perpendicular to $\mathbf{a}$, the components of the metric tensor of the generalised cylinder assume the form:

$$g_{11} = \dot{\boldsymbol{\gamma}} \cdot \dot{\boldsymbol{\gamma}} = ||\dot{\boldsymbol{\gamma}}||^2 = 1,$$
$$g_{12} = g_{21} = \dot{\boldsymbol{\gamma}} \cdot \mathbf{a} = 0, \qquad (3.47)$$
$$g_{22} = \mathbf{a} \cdot \mathbf{a} = ||\mathbf{a}||^2 = 1.$$

Finally, for the above, the first fundamental form for the cylinder is:

$$I = d\theta^1 d\theta^1 + d\theta^2 d\theta^2 = (d\theta^1)^2 + (d\theta^2)^2, \qquad (3.48)$$

which is identical to the first fundamental form of the plane seen in equation (3.44). A similar proof can be conducted for the cone and another class of surfaces known as tangent developables. The cylinder, the cone and tangent developable surfaces are the only classes of surfaces which can be isometrically transformed into the plane.

We have here demonstrated that a plane and a cylinder share the same first fundamental form. Intuitively this means that a plane piece of paper can be wrapped on a cylinder in the obvious way without crumpling the paper. If we draw a

FIG. 3.4

The only plane isometries are the cylinder and the cone. For an isometric mapping, a curve s drawn on a surface will preserve its length upon transformation

curve on the plane, then after wrapping it becomes a curve on the cylinder and neither stretching nor shrinking occurs (Fig. 3.4). On the other hand, experience suggests that it is impossible to wrap a plane sheet of paper around a sphere without crumpling it. Thus, we expect that a plane and a sphere do not have the same first fundamental form.

In conclusion, the only other configurations achievable from a planar sheet of material without incurring in excessive strain are cylindrical and conical surfaces.

3.2 Differential geometry of discrete surfaces

In the previous sections fundamental properties of smooth, continuous, differentiable surfaces were derived. The Gaussian curvature plays a fundamental role in the load bearing behaviour of shell structures and it is the main property used to describe their shape. In this work we are primarily concerned with the relationship between curvature and the deformation of thin plates. As the extensive simulation work done to describe the behaviour of bending-active plate structures was developed with Finite Element technology, a natural discrepancy exists between the smooth mathematical surfaces and the discrete models employed for the simulations. In the case of a triangulated discrete version of a surface, i.e. a triangular mesh, every point on the mesh will obviously return a zero Gaussian curvature, as a triangle is by definition planar. Obviously, our natural intuition tells us that the discrete surface must possess a similar degree of Gaussian curvature as its continuous counterpart despite being locally planar at each element. The study of these invariant properties form the foundation of what is commonly referred to as the field of discrete differential geometry [Bobenko et al. 2008].

The research in discrete differential geometry has been extremely prolific in recent years, especially triggered by applications in computer science. Nonetheless, this research field is still a relatively young one, the first theoretical works having emerged only recently. Despite the large amount of scientific work and the many code packages developed, 3d-modelling software are still lacking a solid implementation of these methods. For this reason, the necessary code was implemented by the author to run within the Rhino and Grasshopper environments. Specifically, the code developed is embedded within the half-edge mesh library Plankton developed by Will Pearson and Daniel Piker of McNeel.

To study the geometric properties of bending-active structures, we introduce a series of tools derived from the literature on discrete differential geometry which allow to describe such invariant characteristics. In particular, the main
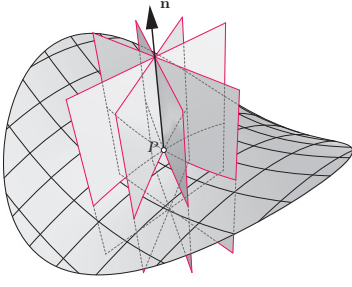
Normal curvatures around the normal support **n** at point P

focus is set on the derivation of a general strategy to study the Gaussian curvature of discrete meshes. Many approaches exist and a general consensus in the scientific community on the best approach does not exist, as new algorithms and methods are still being developed on a regular basis. The method presented in the following sections are taken from [Meyer et al. 2003] which, at the time of writing, sports an astonishing 1493 citations. Based on this authority (but also on the results obtained) their method was implemented and employed as a tool to evaluate the simulation geometries contained in this work.

3.2.1 Fundamental quantities of smooth surfaces

We begin with a review of several important quantities from the differential geometry of smooth surfaces which will be needed to establish the fundamental relationships of surfaces represented by a discrete triangular mesh. This is followed by a technique for extending these quantities to the discrete domain using spatial averaging.

Let S be a surface described by an arbitrary parameterisation of 2 variables θ^1 and θ^2. For each point on S, we can locally approximate the surface by the tangent plane uniquely defined by the normal vector **n**. We recall the definition of the normal curvature $\kappa_{normal}(\varphi)$, which is the curvature of the curve that belongs to both the surface and the sectioning plane containing the normal **n** and the orientation vector of the plane $\mathbf{e}_\varphi$. Here, the normal curvature and the orientation vector have been defined as depending on the orientation angle φ. The two principal curvatures κ_1 and κ_2 of the surface S, with their associated orthogonal principal directions $\mathbf{e}_1$ and $\mathbf{e}_2$ are the extreme values of all the normal curvatures (Fig. 3.5). The mean curvature κ_H is also defined as the average of the normal curvatures. This can be obtained by integrating the curvature values along each direction:

$$\kappa_H = \frac{1}{2} \int_0^{2\pi} \kappa^N(\theta) d\theta. \tag{3.49}$$

Expressing the normal curvature in terms of the principal curvatures using Euler's Theorem, $\kappa_{normal}(\varphi) = \kappa_1 \cos^2(\varphi) + \kappa_2 \sin^2(\varphi)$, where φ is the angle between the direction $d\theta^2/d\theta^1$, leads to the definition (3.26): $\kappa_H = (\kappa_1 + \kappa_2)/2$. The Gaussian curvature κ_G is again defined as the product of the two principle curvatures (3.27): $\kappa_G = \kappa_1 \kappa_2$.

Surfaces with $\kappa_H = 0$ have been called minimal back in chapter 3.1.4. This is due to the fact that, given a certain boundary condition, surfaces with 0 mean curvature are the ones which minimise the area, i.e. $\kappa_H = 0$ is the condition for area minimisation. This fact gave rise to a considerable body

of literature on minimal surfaces and provides a direct relationship between surface area minimization and mean curvature flow:

$$2\kappa_H \mathbf{n} = \lim_{diam(\mathcal{A}) \to 0} \frac{\nabla \mathcal{A}}{\mathcal{A}}, \qquad (3.50)$$

where A is an infinitesimal area around a point P on the surface, $diam(A)$ its diameter, and ∇ is the gradient with respect to the x, y, z coordinates of P [Meyer et al. 2003]. We introduce the Laplace-Beltrami operator for the surface S, which maps a point P to the vector $\mathrm{K}(P) = 2\kappa_{\mathrm{H}}(P)\mathbf{n}(P)$, i.e. for each point on the surface it associates the normal vector scaled by twice the mean curvature at the point. This quantity will be used extensively in the following sections. Just like the mean curvature, also the Gaussian curvature can be expressed as a limit:

$$\kappa_G = \lim_{diam(\mathcal{A}) \to 0} \frac{\mathcal{A}^{\mathcal{G}}}{\mathcal{A}}, \qquad (3.51)$$

where A^G is the area of the image of the Gauss map (also called the spherical image) associated with the infinitesimal surface A. The above definitions, as well as many more details, can be found in literature on differential geometry [Pressley 2012].

3.2.2 Discrete mean curvature

We first define the 1-ring neighbourhood as all the triangular elements neighbouring a vertex P (Fig 3.6a). The Voronoi region for the vertex P is defined as the sum of the Voronoi areas of each triangle belonging to the 1-ring neighbourhood (Fig. 3.6b). Summing these areas for the whole 1-ring neighbourhood, we can write the Voronoi area for a vertex $\mathbf{x}_i$ as a function of the neighbours $\mathbf{x}_j$ (Fig 3.6c):

$$\mathcal{A}_{Voronoi} = \frac{1}{8} \sum_{j \in N_1(i)} (\cot \alpha_{ij} + \cot \beta_{ij}) ||\mathbf{x}_i - \mathbf{x}_j||^2 \qquad (3.52)$$

Meyer et al. [Meyer et al. 2003] proved that if there is an obtuse triangle among the 1-ring neighbours or among the triangles edge adjacent to the 1-ring triangles, the formula for the Voronoi region no longer holds. The meshes employed for Finite Element simulations are generally regular enough, so that (3.52) is still valid.

Having defined the Voronoi area, the mean curvature normal operator $\mathbf{K}$ can be written using the following expression:

$$\mathbf{K}(\mathbf{x}_i) = \frac{1}{2\mathcal{A}_{Mixed}} \sum_{j \in N_1(i)} (\cot \alpha_{ij} + \cot \beta_{ij})(\mathbf{x}_i - \mathbf{x}_j). \qquad (3.53)$$
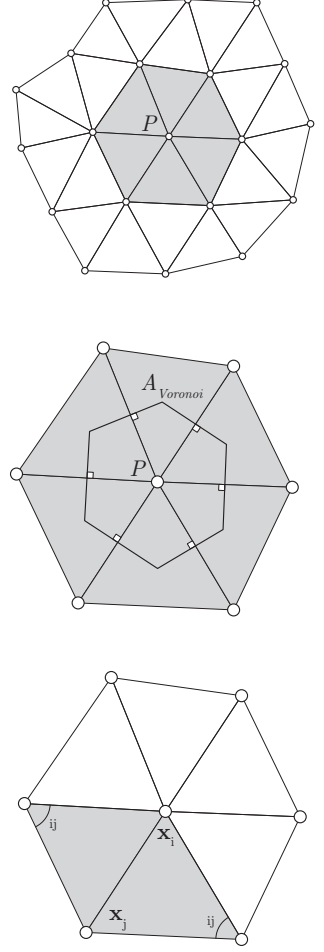
FIG. 3.6

a. 1-ring neighbourhood at vertex P, b. Voronoi area of vertex P, c. Angles of the neighbourhood employed for the cotangent formula

37

$$\int \kappa(\text{🐰})dA$$

$$=$$

$$\int \kappa(\text{🐄})dA$$

$$=$$

$$\int \kappa(\text{⚪})dA$$

$$= \quad 4\pi$$
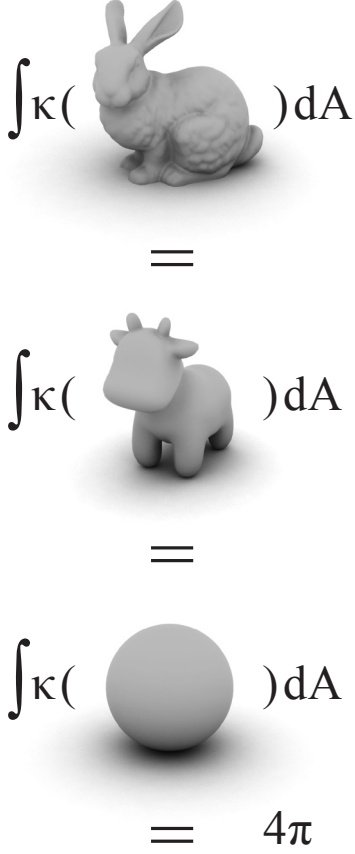
FIG. 3.7

The Gauss-Bonnet Theorem states that for a closed surface of genus 1 the integral of the Gaussian curvature over the surface is two times the Euler characteristic, in this case 4π (model b courtesy K. Crane)

The mean curvature κ_H can be easily computed from this expression by taking half of the magnitude of the mean curvature normal. The normal vector is found by simply normalising the resulting vector $\mathbf{K}(\mathbf{x}_i)$.

3.2.3 Discrete Gaussian curvature

Having derived the relationships for the mean curvature operator and the mean curvature value, we now proceed to find the discrete version of the Gaussian curvature. To do so we first need to find an exact value of the integral of the Gaussian curvature κ_G over a finite-volume region on a piecewise linear surface. To do so we make use of the Gauss-Bonnet Theorem [Pressley 2012]. The Gauss-Bonnet Theorem is an important result in differential geometry which relates the average of the Gaussian curvature to the Euler characteristic χ. The importance of the theorem relies in the connection that it establishes between the geometrical properties of a surface and its topological properties. In its continuous version the Gauss-Bonnet Theorem assumes the following form:

$$\int_M \kappa_G dA = 2\pi\chi(M), \tag{3.54}$$

where M is a continuous surface, κ_G the Gaussian curvature, dA the infinitesimal area of the surface and $\chi(M)$ the Euler characteristic of the surface. In simple terms, the theorem states that the integral of the Gaussian curvature over the surface is equal to twice the Euler characteristic times π (Fig. 3.7). Applied to our discrete triangulated surface, for the 1-ring neighbourhood of a vertex $\mathbf{x}_i$ the Gauss-Bonnet theorem can be reformulated as:

$$\int_{\mathcal{A}_V} \kappa_G dA = 2\pi - \sum_{j=1}^{\#f} \theta_j, \tag{3.55}$$

where A_V is the Voronoi area of the 1-ring, φ_j is the angle of the j-th face at the vertex $\mathbf{x}_i$, and $\#f$ denotes the number of faces around this vertex [Meyer et al. 2003]. The integral of the Gaussian curvature is sometimes also called total curvature. Note again that this formula holds for any surface patch within the 1-ring neighbourhood.

Our Gaussian curvature discrete operator can thus be expressed as:

$$\kappa_G(\mathbf{x}_i) = (2\pi - \sum_{j=1}^{\#f} \theta_j)/\mathcal{A}_{Voronoi}. \tag{3.56}$$

In the case of flat surfaces, this operator will return zero, guaranteeing a satisfactory behaviour for trivial cases.

3.2.4 Discrete principal curvatures

Having retrieved the mean and Gaussian curvature for the case of discrete surfaces (Fig. 3.8), the last important quantities that need to be computed are the principal curvatures along with their associated directions. The principal curvatures can be easily determined from the values of the mean and Gaussian curvatures determined in the previous sections. A separate treatment will be reserved to the determination of the principal directions as these are not as trivial to retrieve as the principal values alone.

As seen previously, the mean and Gaussian curvature are easy to express in terms of the two principal curvatures κ_1 and κ_2. Therefore, since both κ_H and κ_G have already been derived for triangulated surfaces, we can define the discrete principal curvatures as following:

$$\begin{aligned} \kappa_1(\mathbf{x}_i) &= \kappa_H(\mathbf{x}_i) + \sqrt{\Delta(\mathbf{x}_i)}, \\ \kappa_2(\mathbf{x}_i) &= \kappa_H(\mathbf{x}_i) - \sqrt{\Delta(\mathbf{x}_i)}, \end{aligned} \tag{3.57}$$

with:

$$\begin{aligned} \Delta(\mathbf{x}_i) &= \kappa_H^2(\mathbf{x}_i) - \kappa_G(\mathbf{x}_i), \\ \kappa_H(\mathbf{x}_i) &= \frac{1}{2}||\mathbf{K}(\mathbf{x}_i)||. \end{aligned} \tag{3.58}$$

3.2.5 Discrete principal curvature directions

In order to find the two orthogonal principal curvature directions we construct the symmetric curvature tensor $\mathbf{B}$ as being defined by three unknowns a, b, c:

$$B = \begin{bmatrix} a & b \\ b & c \end{bmatrix}. \tag{3.59}$$

This tensor provides the normal curvature in any direction in the tangent plane for each point P on the triangulated mesh. Therefore, when selecting an arbitrary direction of the edges of the 1-ring neighbourhood, we can compute the normal curvature as:

$$\mathbf{d}_{i,j}^T \, B \, \mathbf{d}_{i,j} = \kappa_{i,j}^N, \tag{3.60}$$

where $\mathbf{d}_{i,j}$ is the unit direction in the tangent plane of the edge $\mathbf{x}_i\mathbf{x}_j$. Since we know the normal vector $\mathbf{n}$ to the tangent plane, this direction is calculated using a simple projection onto the tangent plane:
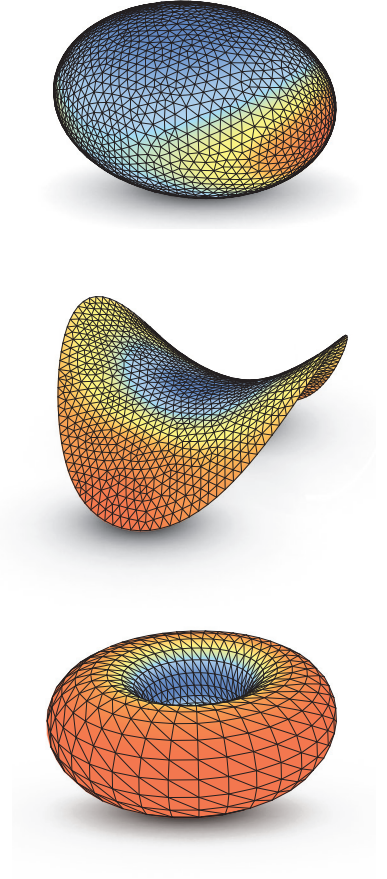
FIG. 3.8

Examples of discrete Gaussian curvature of triangular mesh surfaces

39

$$\mathbf{d}_{i,j} = \frac{(\mathbf{x}_j - \mathbf{x}_i) - [(\mathbf{x}_j - \mathbf{x}_i) \cdot \mathbf{n}] \; \mathbf{n}}{||(\mathbf{x}_j - \mathbf{x}_i) - [(\mathbf{x}_j - \mathbf{x}_i) \cdot \mathbf{n}] \; \mathbf{n}||}. \tag{3.61}$$

To find the principal directions, a least-square approximation can be employed to minimise the error E as suggested by [Meyer et al. 2003]:

$$E(a, b, c) = \sum_j w_j \left(\mathbf{d}_{i,j}^T \; B \; \mathbf{d}_{i,j} - \kappa_{i,j}^N \right)^2. \tag{3.62}$$

Moreover, two constraints can be added to ensure coherent results: $a + b = 2\kappa_H$ and $ac - 2b = \kappa_G$. Adding these constraints turns the minimisation problem into a third degree polynomial root finding problem, therefore simplifying the problem which can be directly solved algebraically. Having found the three coefficients of the curvature tensor $\mathbf{B}$, we find the two principal axes $\mathbf{e}_1$ and $\mathbf{e}_2$ as the two (orthogonal) eigenvectors the tensor.

4. Mechanics of plates

In the present chapter fundamental structural mechanics concepts are introduced to build the framework on which this work is based upon. Relying in particular on the contents of the previous chapter, the intrinsic geometric nature of plates and their structural behaviour will be highlighted in the following sections.

This chapter will start with an overview of the different sources of nonlinearity which can normally be encountered in the response of structures. This section will serve as a general introduction to establish the framework of analysis and justify the simulation tools which were employed in the development of the current work.

The following sections will then focus on the mechanical description of the behaviour of plate structures. In the first part the classical theory of plates as known from the work of Kirchhoff and Love will be introduced. The essential mechanical quantities and the equations of equilibrium will be derived along with considerations on the validity of this mechanical model and references to alternative formulations. The second part will concentrate on the nonlinear theory of plate structures as derived by Föppl and von Kármán. The reason for the extension of the linear framework to the full nonlinear theory of plates is justified by the richer mathematical nature of the latter and the deeper insight that it provides. In particular it will be demonstrated how the results derived in chapter 3 on the differential geometry of surfaces, and specifically Gauss' Theorema Egregium, find a direct counterpart in the nonlinear mechanical description of plates. This link between the geometry and the mechanics of plates will wrap up the considerations pertaining the deformation of planar elements and their form-inducing abilities.

The concluding sections will then be devoted to explaining the framework that was employed for the simulations contained in the upcoming chapters. A brief introduction of the Finite Element Method will be followed by the explanation of the calculation routines developed for the simulations and the methods adopted for the structural form-finding. Two aspects will be of particular relevance, the first being the form-finding strategies developed within the context of this research and the routines implemented to optimise and speed up calculation time.
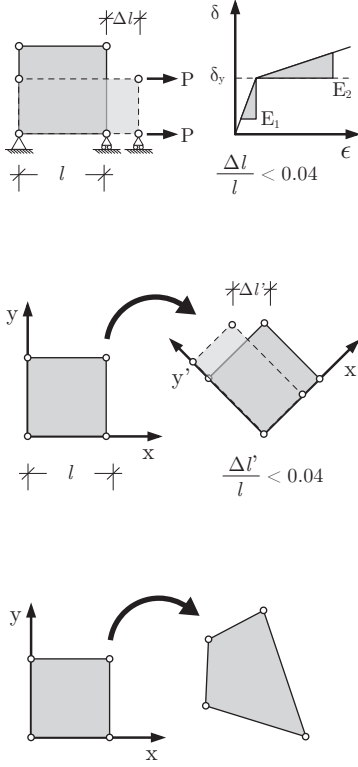
FIG. 4.1

Sources of nonlinearity. a. Materially nonlinear, b. Geometrically nonlinear, c. Materially and geometrically nonlinear

4.1 Sources of nonlinearity

In structural analysis several sources of nonlinear behaviour can be identified. Felippa defines the sources of nonlinearity as following: *geometric, material, force boundary condition and displacement boundary condition* [Felippa 2012]. *Geometric* nonlinearities arise when non-neglectable changes in geometry occur under loading and must therefore be taken into account. Typical applications of geometric nonlinear theory can be found in the modelling of slender elements, tensile structures, cable nets, inflatable membranes. *Material* nonlinearities draw a dependence of the material behaviour on the current deformation state and the history of the deformation. The constitutive models change depending on the type of material and are commonly used to model effects such as nonlinear elasticity, plasticity, viscoelasticity, creep. *Force* and *displacement boundary condition* nonlinearities arise from applied forces or displacement boundary conditions respectively which depend on the deformation of the structure. Typical applications are pressure loads of fluids (aerodynamics and hydrodynamics) and contact problems.

Without delving into the details of the latter two categories, which go beyond the scope of this introduction, we can further refine the categorisation of nonlinear sources by considering the possible states in which a structure may find itself in. Based on Bathe [Bathe 1996] the available options are (Fig. 4.1):

1. Materially-nonlinear-only: the displacements are infinitesimal; the strains are infinitesimal; the stress-strain relationship is nonlinear. (As long as the yield point has not been reached we have a linear analysis).
2. Large displacements, large rotations but small strains: the displacements and rotations are large; the strains are small; the stress-strain relations are either linear or nonlinear. (As long as the displacements are very small, we have an m.n.o).
3. Large displacements, large rotations, large strains: the displacements are large; the rotations are large; the strains are large; the stress-strain relation is probably nonlinear. (This is the most general formulation of a problem, considering no nonlinearities in the boundary conditions).

In the present work we shall mainly be concerned with one approximation: the *small strain* approximation. The small strain approximation allows one to consider that the elastic response of a given material is linear (this contrasts with the

case of finite, or large strain, where solids deform nonlinearly). On the other hand we will place no restrictions on the displacements, meaning that volume elements may undergo rigid-body rotations, which are irrelevant for computing elastic deformations. Large deformations and small strain is the mechanical framework of bending-active structures.

Therefore, it appears that there are two sources of nonlinearity in the theory of elasticity: one comes from the elastic constitutive law and the other from geometry. The first one is associated with the intrinsic response of the material, that is how a volume elements deforms under a loading condition and given stress state. The other source of nonlinearity is tightly connected with geometry. It both affects and is affected by the shape and geometry of the structure in its undeformed state as well as by the geometric configuration in its deformed state. These two kinds of nonlinear contributions are directly related to the assumptions made above about the strain levels and displacements of the material. When the strain remains small, the elastic constitutive laws can be linearised; when the displacements are small, geometrical nonlinearity is negligible. If only the strain is small, geometrical nonlinearity may still play a role.

In the following section we will focus on geometrical nonlinearity and on important associated physical effects. Geometrical nonlinearity is essential for predicting the elastic behaviour of thin bodies such as rods, plates and shells. Bending-active structures typically employ elements with thin cross-sections to take advantage of their large deformation capabilities. Therefore, we do not limit our analysis to small displacements but rather concentrate on finite deformations, where it will be shown that rotations in particular play a fundamental role. Nonetheless, the strain in the material is assumed small so that we can consider linear constitutive laws. This is the framework of Hookean elasticity. These simplifying hypothesis are in accordance with the assumptions made on the reduced cross-sectional thickness of the structural elements. Material nonlinear effects will not be taken into consideration in the development of this work. Although time-dependent effects such as creep and relaxation are important for materials like plywood and GFRPs, especially in the context of large deformations, we will only be concerned with the immediate response of the structure during form-finding and in its final shape. Finally, a further simplification that will be adopted in the upcoming sections is to consider the materials employed perfectly isotropic. Despite the anisotropic nature of most fibre-based materials, the influence of this effect was not deemed relevant in the treatment of the following topics.
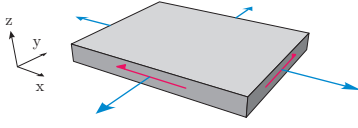
FIG. 4.2

Plate element in the membrane approximation
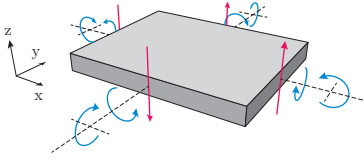
FIG. 4.3

Plate element under bending

4.2 Plates and shells

It is typical in engineering to distinguish between plate and shell structures, the main difference being that plates are initially flat and shells already present curvature in their stress-free configuration. Shells can be either single-curved or double-curved. The type of curvature has a major effect on the mechanical response of the structure. As opposed to rods and beams, both shells and plates can be identified as having thickness significantly smaller than length and width. In this way the geometry of a shell or plate is uniquely defined by their centre surface and local thickness [Bischoff et al. 2004]. From a geometric point of view plates and shells are assimilated to 2d surface elements.

The structural behaviour of shells and plates is characterised by two main states of deformation, *membrane* and *bending* action. Membrane deformations involve strain of the centre surface, whilst bending dominated deformations roughly preserve the length of the midsurface fibres. Under bending, only the material fibres away from the midsurface are fully exploited, therefore the structural elements are much more flexible.

A flat plate can be loaded by forces acting in the plane of the surface or perpendicular to it. A set of forces of the first kind will induce in-plane action in the plate and a membrane stress state. This kind of behaviour is also called plane stress. In Fig. 4.2 a planar plate element in the membrane approximation is depicted. With reference to the x-y coordinate axes and frame of reference, four stress components for the membrane stress are introduced: σ_x, the normal stress in the x-direction; σ_y, the normal stress in the y-direction; τ_{xy}, the shear stress component perpendicular to the x-direction and oriented as y; τ_{yx}, the shear stress component perpendicular to the y-direction and oriented as x. The reciprocity theorem proves that $\tau_{xy} = \tau_{yx}$, de facto reducing the components to three. Normally the stress components have the dimension of force per unit length, as they refer to the extension of the imaginary cross-sectional cut [Adriaenssens et al. 2014]. These set of stress components completely describe the membrane state of a plate element.

If forces perpendicular to the centre surface are applied to the plate, this will experience bending and torsion. The additional actions are depicted in Fig. 4.3. The axis of rotation of the bending moments M_x and M_y will respectively be oriented perpendicular to the x-z plane and the y-z plane. The twisting moment M_{xy} is directed along the x axis, and similarly the M_{yx} twisting moments along the y axis. As for the reciprocity of the shear stress in the membrane state, it can

44

be proven that $M_{xy} = M_{yx}$. As will be shown in the following section, for the equilibrium of the moments these are balanced by shear forces acting in the direction perpendicular to the centre surface. With reference to Fig. 4.3 the shear forces Q_x are the ones directed on the plane with normal x, and the Q_y shear forces are oriented along the plane with y axis normal. Together with the membrane theory, the bending theory of plates completes the description of the mechanical behaviour of plate structures.

A shell or plate which is subject to a bending stress state is said to undergo *pure bending*. Pure bending deformations are also called *inextensional deformations* as the neutral surface is completely free from longitudinal extension or compression and the structural element is bent without stretching. As seen in chapter 3, in mathematical terms a transformation that preserves lengths is also referred to as an *isometry*. *Pure bending*, *inextensional* and *isometric deformations* are all synonyms that are often used interchangeably in literature, preferring one term over another to highlight either mechanical or mathematical aspects [La Magna et al. 2016]. Strictly speaking, the only isometric transformations of the plane are into cones and cylinders, i.e. developable surfaces. As will be seen, these play a special role in the context of bending-active structures.

In structural applications, membrane deformation states are generally preferred as the cross-section is completely utilised and the load-bearing behaviour of the shell is significantly enhanced. This is the principal way of working of compression-only shells and similar structural typologies known as form-passive structures as defined by Heino Engel [Engel 1999]. This fundamental aspect is what makes compressive shells extremely efficient in terms of span-to-thickness ratio. On the other hand, characteristics of inextensional deformations may be exploited in certain situations, for example deployable or tensile structures which might benefit from bending dominated transition stages. In the context of bending-active structures, inextensional deformations represent the main modality of shape shifting, as the bending elements may undergo large deformations without reaching a critical stress state for the material. Owing to the high flexibility of thin plates with respect to bending, this state of deformation may be regarded as the dominating mechanical effect for bending-active structures as having the strongest effect on the nonlinear behaviour of plates.
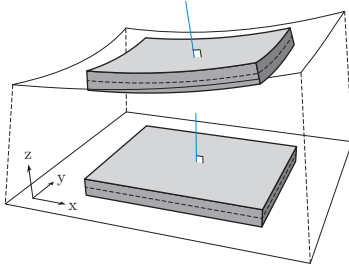
Kirchhoff's hypothesis for plates. Vectors normal to the surface in the undeformed state remain normal to the surface in its deformed state

4.3 Mechanics of plate structures

As this work is primarily concerned with the mechanical behaviour of planar elements, in this chapter we will focus exclusively on plate structures, as the treatment of shells is beyond the scope of this introduction. To better understand the global geometric effects of bending and stretching, we will first recall the theory of elastic plates in the linear approximation. The linear theory will then be extended to the nonlinear theory of plates to highlight fundamental aspects about the compatible deformation field of plates and their formability.

4.3.1 Classic linear theory of plates

The classical theory of thin plates is normally associated with the work of Kirchhoff who formalised the governing equations for plates in 1850 [Kirchhoff 1850]. Kirchhoff's theory contributed to the understanding of the bending of plates and promoted its widespread use in practice. Although Kirchhoff is primarily credited for the development of the theory, his work is based on decades of research on elasticity by eminent French mathematicians including Lagrange, Cauchy, Poisson and in particular Sophie Germain [Germain 1826] who was the first to develop a plate differential equation as early as 1811, for which she was notoriously awarded a prize by the Paris Academy of Science in 1816, the first woman to ever achieve such high decoration. The plate theory as commonly taught is also known as Kirchhoff-Love plate theory, as in its present form it was developed by Love in 1888 using the assumptions based on Kirchhoff [Love 1888].

The following paragraphs will be concerned exclusively with Kirchhoff's theory of thin plates, but for the sake of completeness and for aspects linked to numerical aspects addressed at the end of this chapter we briefly recall successive developments in the theory of plates. In 1945 Reissner [Reissner 1945], and in a different form Mindlin in 1951 [Mindlin 1951], developed the theory further by relaxing the assumptions of Kirchhoff. Their work gave rise to the now known Reissner-Mindlin theory of thick plates. Although analytically more complex than its counterpart for thin plates, Reissner-Mindlin's theory turns out to be simpler to implement in Finite Element code, which makes it *de facto* the standard in commercial software for structural analysis. This is due to the relaxation on the constraints on the curvature continuity for neighbouring finite elements, which need to comply with less restrictive features as the continuity requirements for the displacement assumption are lowered to C^0 continuity. This makes it easier to use arbitrary meshes for the analysis.

We now establish the classical equations for elastic plates in the small-deflection approximation. These are based on the following fundamental assumptions, also assumed by Kirchhoff in his treatment [Mansfield 1964]:

— "points which lie on a normal to the mid-plane of the undeflected plate lie on a normal to the mid-plane of the deflected plate" (Fig. 4.4);

— "the stress normal to the mid-plane of the plate, arising from the applied loading, are negligible in comparison with the stresses in the plane of the plate";

— "the slope of the deflected curve in any direction is small so that its square may be neglected in comparison to unity";

— "the mid-plane of the plate is a 'neutral plane', i.e. any mid-plane stresses arising from the deflection of the plate into a non-developable surface may be ignored".

The above assumptions translate to the condition that the out of plane shear strain is negligible compared to the in plane components of strain. These hypothesis allow for a simplified derivation of the equilibrium conditions.

With reference to Fig. 4.5, let u, v and w be the components of displacement in x, y and z directions of points lying on the centre surface of the plate. The component of the displacement vector w normal to the surface is commonly referred to as *deflection*. For the above assumptions it follows that the displacement field for a thin elastic plate is:

$$w = w(x, y) \quad u = -z\frac{\partial w}{\partial x} \quad v = -z\frac{\partial w}{\partial y} \tag{4.1}$$

From the above it follows that the displacements u and v of an arbitrary layer varies linearly over the plate's thickness, while the deflection remains constant throughout the section. Recalling the relationship between strain and displacement, which in Einstein's notation reads:

$$\epsilon_{ij} = \frac{1}{2}\left(\frac{\partial u_i}{\partial x_j} + \frac{\partial u_j}{\partial x_i}\right) \tag{4.2}$$

where the double index ij implies summation over the repeated indices, the strain components for thin plates assumes the following form [Ventsel and Krauthammer 2001]:

$$\epsilon_x = -z\frac{\partial^2 w}{\partial x^2} \quad \epsilon_y = -z\frac{\partial^2 w}{\partial y^2} \quad \gamma_{xy} = -2z\frac{\partial^2 w}{\partial x\partial y} \tag{4.3}$$
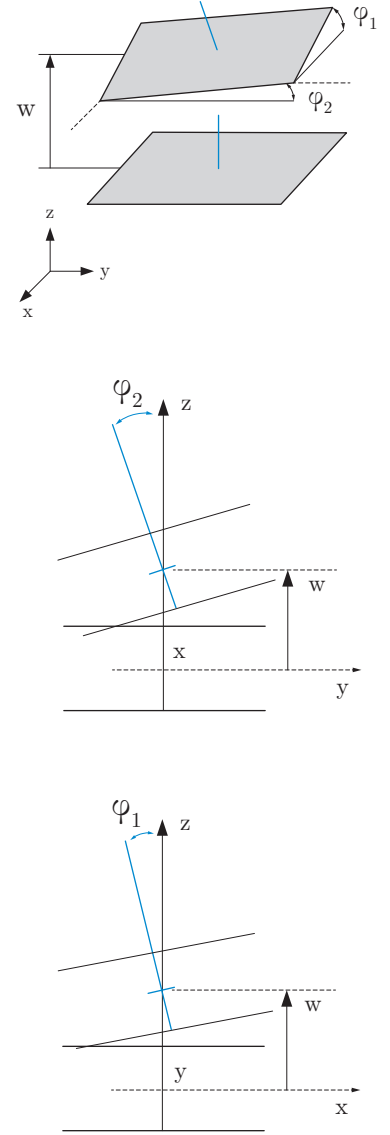
FIG. 4.5

Displacement field for plates in the classic linear theory

and for the z dependent components of the strain:

$$\epsilon_z = 0 \quad \gamma_{xz} = 0 \quad \gamma_{yz} = 0 \tag{4.4}$$

as previously discussed.

We recall here that the strain-displacement relationship (4.2) is derived for the small deflection approximation, and therefore the nonlinear terms have been dropped from the equations. For plates deforming under bending, the slopes in the x and y directions with respect to the neutral plane are respectively $\partial w / \partial x$ and $\partial w / \partial y$, as we assume negligible the difference between reference and deformed configuration. As a consequence, the curvatures of the mid-plane surface can be calculated as the second derivative of the deflection:

$$\kappa_x = \frac{\partial^2 w}{\partial x^2} \qquad \kappa_y = \frac{\partial^2 w}{\partial y^2} \qquad \kappa_{xy} = \frac{\partial^2 w}{\partial x \partial y} \tag{4.5}$$

where κ_x and κ_y represent the curvature of the centre surface in x and y directions and κ_{xy} the twisting curvature [Naicu 2016]. This result is similar to the curvature-deflection relationship for Euler-Bernoulli beams. Comparing the curvature with the strain relationships, we can rewrite the strain components in terms of curvature. This leads to:

$$\epsilon_x = z \kappa_x \qquad \epsilon_y = z \kappa_y \qquad \epsilon_{xy} = z \kappa_{xy} \tag{4.6}$$

which establishes a direct relationship between the curvature of the plate and the strain in the laminas placed at distance z from the mid-surface.

For the sake of completeness we recall the full derivation of Kirchhoff's plates' equations. Within the framework of linear elasticity, stress and strain are directly related through Hooke's law. Furthermore, Kirchhoff's assumptions allows us to drop three of the six equations which are identically zero as mentioned above. The remaining components of stress σ_x, σ_x and τ_{xy} assume the form:

$$\begin{aligned} \sigma_x &= \frac{E}{1 - \nu^2} (\epsilon_x + \nu \epsilon_y) \\ \sigma_y &= \frac{E}{1 - \nu^2} (\epsilon_y + \nu \epsilon_x) \\ \sigma_{xy} &= \sigma_{yx} = \frac{E}{1 + \nu} \epsilon_{xy}. \end{aligned} \tag{4.7}$$

Equation (4.7) completely define the variation of stress through the plate's thickness. By integration over the thickness of the plate we recover the moments and shear forces which are needed to establish the equilibrium equations. For

the moments these read:

$$M_x = \int_{-t/2}^{+t/2} z\sigma_x dz = -D\left(\frac{\partial^2 w}{\partial x^2} + \nu\frac{\partial^2 w}{\partial y^2}\right)$$

$$M_y = \int_{-t/2}^{+t/2} z\sigma_y dz = -D\left(\frac{\partial^2 w}{\partial y^2} + \nu\frac{\partial^2 w}{\partial x^2}\right) \tag{4.8}$$

$$M_{xy} = \int_{-t/2}^{+t/2} z\tau_{xy} dz = -D(1-\nu)\frac{\partial^2 w}{\partial x \partial y},$$

where we have introduced the quantity D known as the *flexural rigidity of the plate*:

$$D = \frac{Eh^3}{12(1-\nu^2)}. \tag{4.9}$$

For the shear forces, although the theory of thin plates omits the effect of the strain components in z direction, the vertical shear forces Q_x and Q_y are non-negligible. In fact, they are necessary for equilibrium of the plate element. We report the relationship for shear forces in the following, referring to [Ventsel and Krauthammer 2001] for a complete derivation of them. We first define the out of plane shear stresses as:

$$\tau_{xz} = -\int_{-t/2}^{+t/2}\left(\frac{\partial\sigma_x}{\partial x} + \frac{\partial\tau_{xy}}{\partial y}\right)dz =$$

$$= \frac{E}{2(1-\nu^2)}\frac{\partial\nabla^2 w}{\partial x}\left(z^2 - \frac{h^2}{4}\right),$$

$$\tag{4.10}$$

$$\tau_{yz} = -\int_{-t/2}^{+t/2}\left(\frac{\partial\sigma_y}{\partial y} + \frac{\partial\tau_{xy}}{\partial x}\right)dz =$$

$$= \frac{E}{2(1-\nu^2)}\frac{\partial\nabla^2 w}{\partial y}\left(z^2 - \frac{h^2}{4}\right),$$

where ∇^2 is the *Laplace operator* given by:

$$\nabla^2 w = \frac{\partial^2 w}{\partial x^2} + \frac{\partial^2 w}{\partial y^2}. \tag{4.11}$$

Having defined the out-of-plane shear stress components, by integration we retrieve the shearing forces acting on the plate:

$$Q_x = \int_{-t/2}^{+t/2} \tau_{xz} dz = -\frac{Eh^3}{12(1-\nu^2)}\frac{\partial\nabla^2 w}{\partial x} = -D\frac{\partial\nabla^2 w}{\partial x}$$

$$Q_y = \int_{-t/2}^{+t/2} \tau_{yz} dz = -\frac{Eh^3}{12(1-\nu^2)}\frac{\partial\nabla^2 w}{\partial y} = -D\frac{\partial\nabla^2 w}{\partial y}. \tag{4.12}$$

The three moments M_x, M_y, M_{xy} and the two shear forces Q_x, Q_y completely describe the state of the plate at a point.

FIG. 4.6

Complete set of membrane and
bending forces acting on the plate
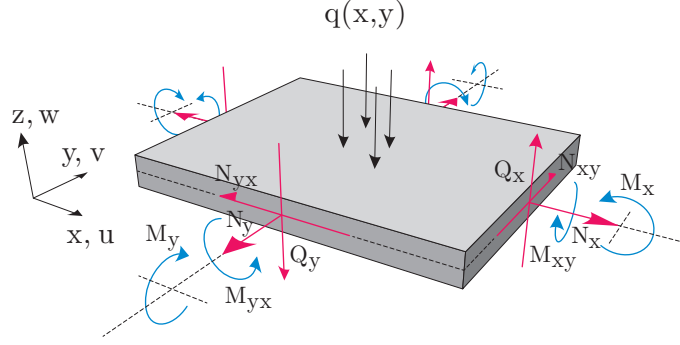
By imposing static conditions of equilibrium we derive the
variation of the stresses and stress resultants within the plate.
For the plate system in Fig. 4.6, the following conditions of
equilibrium apply:

summation of forces in z direction:

$$\frac{\partial Q_x}{\partial x} + \frac{\partial Q_y}{\partial y} + q = 0, \qquad (4.13)$$

summation of moments about the x axis:

$$\frac{\partial M_{xy}}{\partial x} + \frac{\partial M_y}{\partial y} - Q_y = 0, \qquad (4.14)$$

summation of moments about the y axis:

$$\frac{\partial M_{xy}}{\partial y} + \frac{\partial M_x}{\partial x} - Q_x = 0. \qquad (4.15)$$

From equations (4.14) and (4.15) it is possible to ex-
press the shear forces in terms of the moments, and there-
fore group all the above equations in the following:

$$\frac{\partial^2 M_x}{\partial x^2} + 2\frac{\partial^2 M_{xy}}{\partial x \partial y} + \frac{\partial^2 M_y}{\partial y^2} = -q, \qquad (4.16)$$

which expressed in terms of displacement w yields:

$$\frac{\partial^4 w}{\partial x^4} + 2\frac{\partial^4 w}{\partial x^2 \partial y^2} + \frac{\partial^4 w}{\partial y^4} = \frac{q}{D}. \qquad (4.17)$$

By introducing the *biharmonic operator* defined as the square of the Laplacian:

$$\nabla^4(\quad) \equiv \nabla^2(\nabla^2\quad) \equiv \frac{\partial^4}{\partial x^2} + \frac{\partial^4}{\partial x^2 y^2} + \frac{\partial^4}{\partial y^4}, \qquad (4.18)$$

we can rewrite (4.17) in compact form as:

$$\nabla^4 w = \frac{q}{D}, \qquad (4.19)$$

which is the differential equation for the deflection of a thin elastic plate of flexural stiffness D subject to a uniformly distributed vertical load of intensity q acting downwards.

This completes the introduction to the classic linear theory of plates. We highlight again how the theory shown here is valid only in the approximation of small displacements. This derives from the approximation on the components of strain that was performed at the beginning of the section by assuming a linear displacement field. For bending-active structures this is definitely not the case. The large deformation of the plate elements is actively employed to give shape to the structural system, and is an integral part of the conceptual idea of how this typology is constructed. Performing a linear approximation over the deformation field of the plate means disregarding the fundamental aspects that define bending-active structures.

The following section will address these aspects in detail. The theory will be improved by taking into account also higher order terms of the displacement field, therefore including those aspects that were left aside so far in the treatment of plates. In particular, this will be done to discuss and highlight the limits on the formability of plates, as this work especially focuses on the shape-giving potential of plates and plate-based systems. In terms of mechanical stress though, the linear approximation delivers accurate values for bending-active plate structures as the deformations are mostly non-extensional which leave the material fibres unstrained. In terms of displacements the results may not be reliable in the linear approximation, but we can still establish proportional relationships between quantities as curvature and angle of torsion to verify the material stress state. As it is almost impossible to define analytically a complete and satisfactory description for the large displacements of such systems, numerical analysis is necessary to gain a thorough understanding of the structural behaviour. Nonetheless, being able to quickly assess the quality of the geometry based on simple, straightforward relationships is invaluable especially in the early stages of design.

4.3.2 Nonlinear theory of plates

The relationships seen above are generally valid for plates which undergo small deflections where the strain of the middle surface can be neglected. When this assumption no longer holds, other relationships must be developed which correctly predict the large displacements. Specifically, this entails incorporating the higher order terms of the displacement that were neglected in the development of the classical linear plate theory.

The solution of the nonlinear plate equations is generally extremely complicated. These are nonlinear partial differential equations, and present a closed analytical solution only for few, very simple cases. Therefore, solutions are normally sought numerically with the aid of the Finite Element Method, as it is also the case in this work. Nonetheless, we derive in the following section the so called Föppl–von Kármán equations for large deformations of plates to highlight a key aspect which is otherwise lost in the linear treatment, i.e. the relationship between strain and Gaussian curvature.

The nonlinear equations for large deflection behaviour of plates were first derived by von Kármán in 1910 [von Kármán 1910] by extending work developed by Föppl in 1907 [Föppl 1907]. Föppl's treatment considered only the stretching energy, delivering a membrane approximation of the plate's behaviour. The main contribution of von Kármán was to incorporate also bending effects, therefore completing the description of plates under both stretching and bending. In the following paragraphs we will pursue the derivation by Audoly and Pomeau [Audoly and Pomeau 2010], focussing on the most relevant aspects for the development of this work. The interested reader is referred to the above publication for a detailed treatment of the subject.

We first introduce the treatment of the plate in the membrane approximation. In this case we neglect bending and consider only stretching effects. Similarly to the classical treatment of plates, we assume that any dependency of strain and stress with respect to z can be neglected as long as only stretching effects are considered:

$$\epsilon_z = 0 \quad \gamma_{xz} = 0 \quad \gamma_{yz} = 0 \tag{4.20}$$

$$\sigma_z = 0, \quad \sigma_{xz} = 0, \quad \sigma_{yz} = 0. \tag{4.21}$$

The assumptions made so far are identical to Kirchhoff's kinematic hypothesis employed in the linear treatment of elastic plates, namely that each material curve initially perpendicular to the centre surface remains perpendicular after deformation,

therefore limiting shearing effects only in the plane of the mean surface. The main differences derive with the incorporation of the nonlinear terms in the expression of the strain:

$$\epsilon_{ij} = \frac{1}{2}\left(\frac{\partial u_i}{\partial x_j} + \frac{\partial u_j}{\partial x_i}\right) + \frac{1}{2}\frac{\partial u_k}{\partial x_i}\frac{\partial u_k}{\partial x_j}, \qquad (4.22)$$

which is known as the Green-Lagrange strain tensor [Bischoff 2012]. A comparison with the linearized version (4.2) reveals that the Green-Lagrange strain is composed of two parts, the first linear part identical to the Cauchy strain and a second quadratic part which accounts for the nonlinearity of the displacement. It is also worth mentioning that the Green-Lagrange strain tensor vanishes for rigid-body rotations and translations, a characteristic that is not preserved in the linearized version. This feature is crucial in the analysis of large deformations, where rigid-body motions need to be handled correctly to avoid parasitic strains that would be otherwise falsely predicted.

By expanding the full form of the strain components for the x and xy directions for instance we retrieve the following:

$$\begin{aligned}
\epsilon_{xx} = &\frac{\partial u_x}{\partial x} + \frac{1}{2}\left(\left(\frac{\partial u_x}{\partial x}\right)^2 + \left(\frac{\partial u_y}{\partial x}\right)^2 + \left(\frac{\partial u_z}{\partial x}\right)^2\right) \\
\epsilon_{xy} = &\frac{1}{2}\left(\frac{\partial u_x}{\partial y} + \frac{\partial u_y}{\partial x}\right) + \\
&+ \frac{1}{2}\left(\frac{\partial u_x}{\partial x}\frac{\partial u_x}{\partial y} + \frac{\partial u_y}{\partial x}\frac{\partial u_y}{\partial y} + \frac{\partial u_z}{\partial x}\frac{\partial u_z}{\partial y}\right).
\end{aligned} \qquad (4.23)$$

In the above, the strain includes all nonlinear terms and is equally valid for small or finite displacements. By dropping all the nonlinear terms we would recover the Cauchy strain and subsequently the Kirchhoff equations for plates. We make here a less restrictive approximation by dropping the first two nonlinear terms but keeping the third one that depends on the deflections $w(x,y)$. We are performing a partial approximation of small displacements that is for the in-plane components of displacement only. By doing so we lose the invariance of the equations by rotations with a finite angle, but at the same time we can account rather accurately for isometric deformations. For the details on the reasons and implications of this approximation we again refer to [Audoly and Pomeau 2010]. Under this assumption, the components of strain assume the following form:

$$\epsilon_{xx} = \frac{\partial u_x}{\partial x} + \frac{1}{2}\left(\frac{\partial w}{\partial x}\right)^2,$$

$$\epsilon_{xy} = \frac{1}{2}\left(\frac{\partial u_x}{\partial x} + \frac{\partial u_y}{\partial y}\right) + \frac{1}{2}\frac{\partial w}{\partial x}\frac{\partial w}{\partial y}, \qquad (4.24)$$

$$\epsilon_{yy} = \frac{\partial u_y}{\partial y} + \frac{1}{2}\left(\frac{\partial w}{\partial y}\right)^2.$$

To complete the derivation of the plate's equation in the membrane approximation we need to introduce the constitutive equations and the equations of mechanical equilibrium. The constitutive equations have already been derived in (4.7) for the linear case. Rather than developing the equations of equilibrium in explicit form, which would lead to the derivation of the plate's forces and moments as in the linear case, we report here the equations of mechanical equilibrium in compact form [Audoly and Pomeau 2010]:

$$\frac{\partial \sigma_{ij}^{PK2}}{\partial x_j} + \rho g_i = 0, \qquad (4.25a)$$

$$\frac{\partial^2 w}{\partial x_i \partial x_j}\sigma_{ij}^{PK2} + \rho g_z = 0, \qquad (4.25b)$$

where $i,j = x,y$ are the in-plane indices of the plate running along the centre surface. Here ρg_i represents the volumic density of forces acting in-plane and ρg_z the volumic density of forces acting perpendicularly to the plate. The stress tensor σ_{ij}^{PK2} is the second Piola-Kirchhoff's stress tensor which, similarly to the nonlinear version of strain (4.22), is invariant under rotations. Equation (4.25a) denotes the mechanical equilibrium of translations in the linear approximation. Equilibrium of rotations is automatically satisfied by the condition of symmetry $\sigma_{ij} = \sigma_{ji}$ of the tangential stress. The nonlinear term (4.25b) is the net out-of-plane force obtained by coupling curvature and in-plane stress. Relationships (4.25a) and (4.25b) can be identically derived from direct considerations on the balance of forces or following the variational approach of minimisation of elastic energy.

The set of equations (4.24) – kinematic equations, (4.7) – constitutive equations, and (4.25) – equilibrium equations, fully describes the behaviour of elastic plates in the membrane approximation. We now proceed to cast these equations to a simplified form by introducing the Airy potential to highlight the fundamental correlation between strain and Gaussian curvature. By assuming that the external distributed force is purely normal, we can introduce the Airy potential χ, an auxiliary function defined as following:

$$\sigma_{xx} = \frac{\partial^2 \chi}{\partial y^2}, \qquad \sigma_{xy} = -\frac{\partial^2 \chi}{\partial x \partial y}, \qquad \sigma_{yy} = \frac{\partial^2 \chi}{\partial x^2}, \qquad (4.26)$$

where we have dropped the superscript of the second Piola-Kirchhoff stress tensor PK2 for the strain components as there is no ambiguity in the notation.

Through the Airy potential it is possible to rewrite the equations of equilibrium in simplified form, as they can be made dependent on the single scalar function $\chi(x,y)$. We concentrate on equation (4.25a), which can be rewritten as following [Audoly and Pomeau 2010]:

$$\nabla^4 \chi + E \left\{ \frac{\partial^2 w}{\partial x^2} \frac{\partial^2 w}{\partial y^2} - \left(\frac{\partial^2 w}{\partial x \partial y} \right)^2 \right\} = 0. \qquad (4.27)$$

The second term of the above equation is nothing else than the *Gaussian curvature*. It can be read as the product of the two curvatures in x and y directions, corrected by the mixed term in the case of orientation of the reference frame in non-principal directions (the mixed term would vanish, should the frame of reference be oriented with the principal directions of curvature). Equation (4.27) is the first Föppl's equation of an elastic plate in the membrane approximation for large displacements, expressed in terms of the Airy potential. It describes the membrane behaviour of thin, elastic plates under a nonlinear deformation regime.

It is absolutely remarkable to notice how an inherent geometric property like the Gaussian curvature enters the mechanical description of plates completely independently, without having made any assumption on the geometry of the structure. In this way, a direct connection with Gauss' Theoerema Egregium seen in chapter 3 is established. This is not a coincidence, as isometric mappings of the plane minimise the total energy of deformation. Therefore, bending actions will generally be favoured over deformations that involve substantial stretching of the centre surface.

As mentioned in the introduction of this paragraph, Föppl's membrane approximation was later expanded by von Karman to take into account bending effects, to form what are commonly known as the Föppl-von Karman equations. For the sake of completeness we introduce the second Föppl-von Karman equation. Expressed in terms of Airy potential this reads:

$$D\nabla^4 w - h \left(\frac{\partial^2 \chi}{\partial x^2} \frac{\partial^2 w}{\partial y^2} + \frac{\partial^2 \chi}{\partial y^2} \frac{\partial^2 w}{\partial x^2} - 2\frac{\partial^2 \chi}{\partial x \partial y} \frac{\partial^2 w}{\partial x \partial y} \right) - f_z \qquad (4.28)$$

with D being the bending modulus of the plate as previously seen in the classical treatment of plates, h the thickness of the plate and f_z the forces acting perpendicularly to the middle surface.

Without embarking into a detailed description of the structure of the above equation, and again referring to [Audoly and Pomeau 2010] for a complete derivation of it, we notice here that equation (4.28), which describes exclusively the bending behaviour of the plate, does not contain the curvature term that has been found in the membrane description of equation (4.27). This highlights a fundamental aspect, which is the independence of Gaussian curvature and bending effects. This means that to induce double curvature in a planar sheet of material, stretching of the centre surface is required. In synthesis, the tight relationship between the geometry of surfaces and the elasticity of plate structures has to do with the fact that inextensional deformations of the centre surface involve bending deformations only, and therefore cost much less energy than an arbitrary deformation in which stretching is involved.

This remark explains why the Gaussian curvature appears in the Föppl – von Kármán equations, in the first equation (4.27). The Gaussian curvature, which measures by how much the centre surface departs from a developable configuration, is the source term in the equation for the Airy potential χ that governs in-plane stress. As a result, no stretching will be present in the plate if the centre surface can deform isometrically. In other terms, for a plate a change of Gaussian curvature is possible exclusively by stretching, as bending will keep the curvature unaltered.

The plate equations were derived in the linear approximation – Kirchhoff's classical plate theory – and extended to the nonlinear case – Föppl-von Kármán nonlinear plate theory. For both treatments the actions on the plate can be distinguished between membrane and bending actions, where the membrane forces and stresses act over the full cross-section of the plate, and the bending stresses vary linearly over the cross-section. The linear approximation assumes small displacements, therefore it is safe to disregard higher order terms. Despite delivering the correct results, Kirchhoff's theory does not capture a fundamental feature which is the dependency between change in Gaussian curvature and membrane stretching. This aspect is evident in the nonlinear set of equations which describe the behaviour of plates under large deformations. In conclusion, the nonlinear equations of plates and Gauss's Theorema Egregium express the same concept from a mechanical point of view and from its complementary geometrical perspective.

4.4   Energy arguments

The relationship between large deformations and pure bending is well understood in the light of energetic arguments explained in the following paragraph. The quantities derived in the next sections are an estimate of the elastic energy involved in the deformation of a plate. These are based on heuristic arguments and order of magnitude estimates. In the membrane approximation, the elastic energy of a plate reads:

$$\mathcal{E}_{mb} \sim Eh \iint_P (\epsilon_{\alpha\beta})^2_{cs} dxdy, \qquad (4.29)$$

where the subscript cs means that we can evaluate the density of the elastic energy along the centre surface. The approximation (4.29) can be understood as following: it is the surface integral of the squared, two-dimensional strain along the centre surface $\epsilon_{\alpha\beta}$, multiplied by the factor Eh which is proportional to the thickness h and to Young's modulus E of the material.

Conversely, the bending energy of a two-dimensional plate assumes the following form:

$$\mathcal{E}_b \sim \frac{1}{2} \iint_P \frac{Eh^3}{12} \left(\frac{1}{R_{cs}(x,y)} \right)^2 dxdy, \qquad (4.30)$$

which can be read as the surface integral of the squared curvature (dependent on x and y) of the centre surface, multiplied by the factor Eh^3 which is commonly called *bending stiffness*.

Comparing the stretching energy (4.29) with the bending energy (4.30) shows that the small thickness h comes in the flexural energy (4.30) with a larger power than in the stretching energy, i.e. h^3 in place of h. For very thin plates, this makes the energy of isometric deformations much lower than those involving significant stretching of the centre surface. As a result, large deformations will occur mainly under bending, as the low energy involved in the process is generally compatible with the strain limits of the material.

Coupling the results above with the observations derived in chapter 4.3.2 on the nonlinear behaviour of plates and the derivation of Gauss's Theorema Egregium in chapter 3, it is easy to see how bending actions will be favoured against membrane deformations. This concludes the explanation of the nature of bending and the mechanisms involved in the large deformations of plate structures for bending-active plate systems.
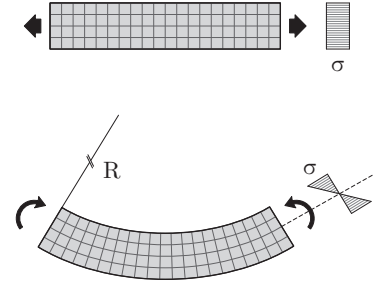
FIG. 4.7

a. Axial forces act on the full cross-section of the plate, b. Bending induces a typical butterfly stress distribution in the plate
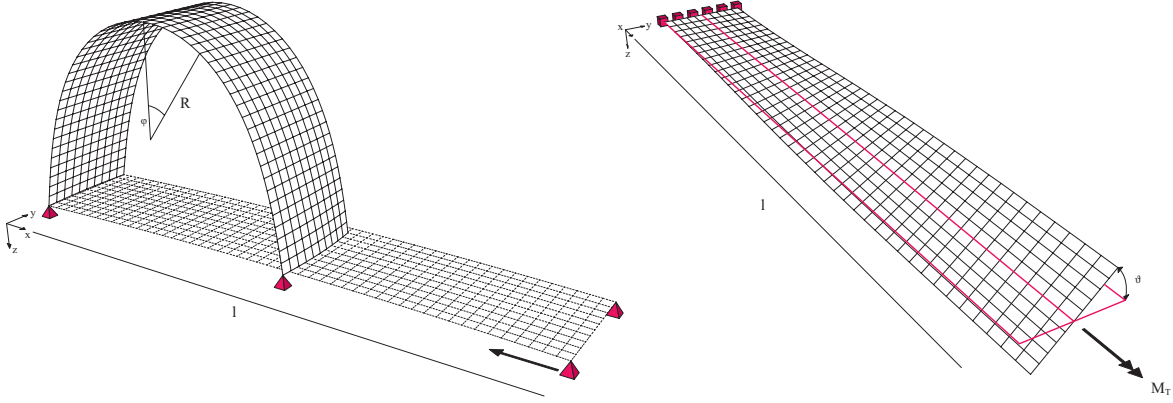
$$k = \frac{d\varphi}{dx} = \frac{M_B}{EI}$$

$$\sigma_{max} = \frac{M_B}{W}$$

$$k_{min} = \frac{1}{R_{max}} = \frac{\sigma_{max}W}{EI} = \frac{2\sigma_{max}}{Eh}$$

with:

k	curvature [1/m]
M_B	Bending moment [kNm]
E	Young's modulus [N/mm^2]
I	Moment of inertia [m^4]
W = bh^2/6	Resistance moment [m^3]
σ_{max}	Max allowable stress [N/mm^2]
h	Section height [mm]

$$\frac{d\theta}{dx} = \frac{M_T}{GJ}$$

$$\tau_{max} = \frac{M_T}{W_T}$$

$$\frac{d\theta}{dx} = \frac{\tau_{max}W_T}{GJ} = \frac{\tau_{max}}{Gh}$$

θ	Angle of twist [rad]
M_T	Torsional moment [kNm]
G	Shear modulus [N/mm^2]
J	Torsional constant [m^4]
W_T = bh^3/3	Torsional resistance [m^3]
τ_{max}	Max shear stress [N/mm^2]
h	Section height [mm]

FIG. 4.8

a. Approximation of plate's behaviour under pure bending, b. Approximation of plate under torsion

4.5 Direct relationships

Although commonly referred as to bending-active, the term has been specifically coined to describe a wide range of systems that employ the large deformation of structural components as a shape-forming strategy. Besides bending, torsional mechanisms can also be employed to induce form, as the energy involved is of similar order of magnitude compared to bending. An essential requirement for bending-active structures is that the stress state arising from the form-finding process does not exceed the yield strength of the material.

Based on the previous assumptions of perfect elastic material response and thin, slender sections, the maximum bending curvature and maximum torsional angle twist can be checked against the relationships in Fig. 4.8a and Fig. 4.8b. These equations refer to the classic Euler-Bernoulli model for bending and de Saint-Venant torsion model for beams. Both models ignore higher order effects, respectively deformations caused by transverse shear and torsional warping. Although generally non-neglectable for large deformations, owing to the previous assumptions of slender cross-sections and elastic

58

behaviour it is safe to assume these values for a preliminary check of the master geometry. The relationships in Fig. 4.8a-b establish a direct relationship between geometric quantities of the deformed structure and the stress level in the material. In this way, assuming that the elements of the structure are initially flat, the design can be easily checked in advance simply based on the geometry of the model.

Bending and torsion are not mutually exclusive and can both simultaneously act on the plate element. What influence bending and torsion have on the stress state in the plate element can be checked using von Mises stress definition. In the most general case of three-dimensional elasticity, von Mises yield criterion reads:

$$\sigma_{vonMises} = \sqrt{\frac{1}{2}[(\sigma_{xx} - \sigma_{yy})^2 + (\sigma_{yy} - \sigma_{zz})^2 + (\sigma_{zz} - \sigma_{xx})^2] + 6(\tau_{xy}^2 + \tau_{yz}^2 + \tau_{zx}^2)}. \tag{4.31}$$

We specialise equation (4.31) by considering a plane stress state:

$$\sigma_{vonMises} = \sqrt{\sigma_{xx}^2 - \sigma_{xx}\sigma_{yy} + \sigma_{yy}^2 + 3\tau_{xy}^2}. \tag{4.32}$$

To evaluate the stress state in the plate we use von Mises stress relationship in the plane stress approximation. This assumption is valid as the axial bending of a plate exclusively induces normal stress in the direction perpendicular to the axis of rotation, and the torsional effect only shearing in the material. For completeness it has to be mentioned that secondary effects due to transversal strain are disregarded, as we consider a material of zero Poisson's ratio. This simplification is acceptable within the limits of tolerance. By plotting the values of the maximum normal bending stress and the maximum shear stress against the limit stress value of the material a good estimate of the combination of bending and torsion can be achieved.

Relationship (4.32) can be further simplified by considering exclusively monoaxial bending. This is mostly the case for bending-active structures, as it has been demonstrated that in most cases only pure bending can be applied to the material. In conclusion, bending-active structures are mainly dominated by pure bending, torsion, or a combination of both. In the case of a combined bending and torsional action on the strip the stress state can be easily checked against von Mises' yield criterion, paying attention that only two components of stress, mainly the normal and shear stress, are present.

4.6   Finite Element Method

The complexity of the analytical solutions and form-finding procedures inevitably requires an accurate numerical analysis. In general, currently available form-finding tools can be subdivided into two categories. The first one, Dynamic Relaxation (DR), is a numerical iterative method to find the solution of a system of nonlinear equations. DR replaces the equations of the static equilibrium with the dynamic equilibrium equations according to d'Alambert [Bletzinger 2016]. Due to the dynamic nature of the system of equations, DR methods employ an explicit time integration scheme with lumped mass. It has been successfully employed in engineering applications for the form-finding of membrane and cable net structures [Barnes 1999, Adriaenssens and Barnes 2001] and in modified versions also for torsion related problems in surface-like shell elements [Nabaei et al. 2013].

The second method relies on the Finite Element Method (FEM). Similar to other numerical methods for the solution of partial differential equations, the Finite Element Method discretises a continuum with a certain number of elements. Hence the name Finite Elements, as the method approximates a continuous domain into a finite set of elements which combined form a discrete version of the original. The Finite Element Method has established itself as the most frequently used numerical discretisation method for problems in structural mechanics. Because of the widespread nature of this method, and especially for the precision of the conveyed results it was identified as the tool of choice for all the simulations contained in the next chapters.

4.6.1   Introduction to FEM

The Finite Element Method is based on a variational formulation of the principal of virtual work [Bischoff 2012]. The principal of virtual work notoriously states that the sum of work done by external forces applied on a system must be balanced by the sum of internal work in an arbitrary (but small) virtual displacement. As opposed to Dynamic Relaxation, the Finite Element Method is a matrix based approach, and for static and quasi-static problems it uses implicit integration schemes which solve the system of algebraic equations at once as opposed to the iterative, explicit integration scheme employed in DR.

The Finite Element Method is exemplified in the well known relationship:

$$\mathbf{K}\mathbf{d} = \mathbf{f}, \tag{4.33}$$

where $\mathbf{K}$ represents the stiffness matrix of the system, $\mathbf{d}$ the vector of unknown displacements and $\mathbf{f}$ the vector of external forces. The elements stiffness matrices can be derived in many ways. A derivation of the stiffness matrix following equilibrium arguments leads to the so-called Direct Stiffness Method. In FEM the stiffness matrix is derived by considerations of virtual work, as the implementation is simpler and more direct despite the higher intellectual complexity involved in the comprehension of the theoretical background.

In the continuous case, the virtual work principle for two-dimensional elasticity problems with a domain Ω and boundary Γ reads [Bischoff 2012]:

$$\int_\Omega \delta\boldsymbol{\varepsilon}^T \boldsymbol{\sigma} d\Omega = \int_\Omega \delta\mathbf{u}^T \mathbf{b} d\Omega + \int_\Gamma \delta\mathbf{u}^T \hat{\mathbf{t}} d\Gamma, \qquad (4.34)$$

where the left hand side of equation (4.34) represents the sum of internal virtual work and the right hand side the sum of external virtual work. Here, the quantity $\boldsymbol{\varepsilon}$ represents the strain matrix and it accounts for the kinematics of the system. It is defined as $\boldsymbol{\varepsilon} = \mathbf{L}\mathbf{u}$, where $\mathbf{L}$ is the differential operator and $\mathbf{u}$ the vector of displacements. The material equations are contained in $\boldsymbol{\sigma}$ known as the stress matrix and defined as $\boldsymbol{\sigma} = \mathbf{C}\boldsymbol{\varepsilon}$, with $\mathbf{C}$ being the material matrix. The first integral of the right hand side is the sum of distributed body forces over the domain Ω and the second integral is the sum of the prescribed surface loads and forces on the traction boundary Γ. Introducing the kinematic equations and material law and substituting, (4.34) becomes:

$$\int_\Omega \left(\delta\boldsymbol{u}^T \boldsymbol{L}^T \right) \mathbf{C}\mathbf{L}\mathbf{u} d\Omega = \int_\Omega \delta\mathbf{u}^T \mathbf{b} d\Omega + \int_\Gamma \delta\mathbf{u}^T \hat{\mathbf{t}} d\Gamma \qquad (4.35)$$

The displacement field $\mathbf{u}$ must satisfy equation (4.35) for all arbitrary virtual displacements $\delta\mathbf{u}$, therefore it can be removed from the above relationship leading to:

$$\int_\Omega \boldsymbol{L}^T \mathbf{C}\mathbf{L} d\Omega \mathbf{u} = \int_\Omega \mathbf{b} d\Omega + \int_\Gamma \delta\hat{\mathbf{t}} d\Gamma, \qquad (4.36)$$

where the displacement vector $\mathbf{u}$ has been taken out of the integral as it does not depend on spatial coordinates.

We now specialise the results above to the discretised version of the problem. The domain Ω is first subdivided into finite elements. The integrals in the virtual work principle can be expressed as sum of element contributions. Therefore we concentrate on one individual element, as the extension to the whole domain is trivial. The main step in the discretisation process is the approximation of the unknown displacements

as a sum of trial functions. These trial functions are expressed as the product of *shape functions* $\mathbf{N}$ and nodal parameters $\mathbf{d}$. Without delving into specific details, we refer the interested reader to dedicated literature [Bathe 1996, Felippa 2012]. Introducing the approximation of all the fundamental quantities seen above we get:

$$\mathbf{u} \approx \mathbf{u}_h = \mathbf{Nd}, \qquad \boldsymbol{\varepsilon} \approx \boldsymbol{\varepsilon}_h = \mathbf{Lu}_h = \mathbf{LNd} = \mathbf{Bd},$$
$$\delta\mathbf{u} \approx \delta\mathbf{u}_h = \mathbf{N}\delta\mathbf{d}, \qquad \delta\boldsymbol{\varepsilon} \approx \boldsymbol{\varepsilon}_h = \mathbf{B}\delta\mathbf{d}, \tag{4.37}$$

with h indicating the discretised counterparts of the continuous quantities. In (4.37) the strain displacement matrix $\mathbf{B}$ has been introduced. Inserting these relations in equation (4.35) we obtain for one element:

$$\int_{\Omega^e} \delta\mathbf{d}^T \mathbf{B}^T \mathbf{CBd} d\Omega = \int_{\Omega^e} \delta\mathbf{d}^T \mathbf{N}^T \mathbf{b} d\Omega + \int_{\Gamma^e} \delta\mathbf{d}^T \mathbf{N}^T \hat{\mathbf{t}} d\Gamma. \tag{4.38}$$

The same arguments discussed for the continuous case also apply in the discrete setting. Therefore equation (4.38) can be further simplified leading to a system of linear algebraic equations:

$$\int_{\Omega^e} \mathbf{B}^T \mathbf{CB} d\Omega \mathbf{d} = \int_{\Omega^e} \mathbf{N}^T \mathbf{b} d\Omega + \int_{\Gamma^e} \mathbf{N}^T \hat{\mathbf{t}} d\Gamma, \tag{4.39}$$

and by grouping terms in the following way:

$$\mathbf{K} = \int_{\Omega^e} \mathbf{B}^T \mathbf{CB} d\Omega, \qquad \mathbf{f} = \int_{\Omega^e} \mathbf{N}^T \mathbf{b} d\Omega + \int_{\Gamma^e} \mathbf{N}^T \hat{\mathbf{t}} d\Gamma \tag{4.40}$$

we retrieve the well known relationship:

$$\mathbf{Kd} = \mathbf{f}. \tag{4.41}$$

This serves as a brief introduction to the theory of Finite Element Analysis. The field is extremely vast, and an extensive number of publications and volumes exist on the topic. Nonetheless, the concepts seen so far are necessary to understand the further developments that lead to the geometrical nonlinear analysis tools employed. All the results presented here were achieved through geometrical nonlinear Finite Element simulations run in the commercial software SOFiSTiK. Benchmarks on the handling of large deflections can be found in [SOFiSTiK 2013a, SOFiSTiK 2013b]. The following sections are devoted to discuss specific implementation aspects and routines developed for the simulation and form-finding of bending-active structure in the software environment of choice.

4.6.2 Incremental load steps for nonlinear FEM

For a linear analysis, the nodal displacement is scaled proportionally to the acting load. Therefore the calculation of the stiffness matrix occurs once and remains constant throughout the analysis process. The magnitude of the displacement is negligible, and therefore the calculation can be performed with respect to the initial configuration. When the magnitude of the displacement is no longer negligible, it becomes necessary to perform a geometric nonlinear analysis. This entails updating all the quantities involved in the calculation to the deformed configuration, as the change in geometry now plays a decisive role in the load bearing mechanism of the structure. As the geometrical configuration of the structure now evolves over the loading process, also the stiffness matrix of the system changes accordingly. Therefore, it is common to refer to the *tangential stiffness matrix*, as the stiffness matrix is sought for each loading step as the tangent to the load-displacement curve. In general, there is no major difference with respect to the conventional computational problem of solving for unknown displacements and back substituting the results in the element stiffness equation to determine the element forces [McGuire et al. 2000]. But for a nonlinear analysis this operation is performed in a stepwise fashion in which the total response is determined through summation of increments. In conclusion, the fundamental difference between linear and geometrically nonlinear analysis is the necessity of discretising the load acting on the structure and the stepwise nature for the solution of each load step.

The major computational cost for geometrically nonlinear Finite Element analysis mainly derives from the stepwise nature of the calculation process. For each loading step it is required to assemble the stiffness matrix, which is generally the most expensive operation of the whole process, and solve the system of algebraic equations, after which an update of the system can be performed and the next loading step applied. This process is repeated up to the full application of the load on the structure.

As the correct solution of the system's equilibrium tends to depart from the linear solution provided by the stiffness matrix at the analysis step (which is the reason why it is referred to as tangential stiffness), an iterative search of the solution space must be performed in order to find the best fitting solution. This is normally conducted through a Newton-Raphson's method with iterative minimisation of the residual forces in the system (Fig. 4.9). Briefly summarising the nonlinear simulation process, this occurs in a nested stepwise fashion: the full load is broken down in successive steps, and

FIG. 4.9

Geometrically nonlinear analysis.
Search of the equilibrium path
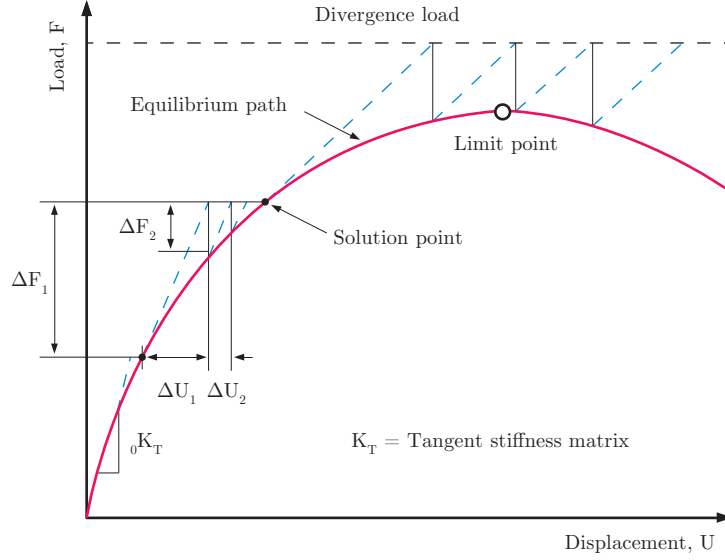
for each step an iterative search is performed to find the solution pertaining to the current load increment.

Typically, the number of iterations needed to reach convergence in one load step is proportional to its size. This means that a small load step will require less iterations to reach convergence as opposed to a larger step. Therefore, the number of required iterations for a load increment are an indicator of the nonlinearity of the system at the specific loading state, which can be employed to scale accordingly the successive load steps. Exercising control over the scaling of the loading process generally has a major effect on the total calculation time. In this way it is possible to dramatically reduce the required time and employ the power of this simulation technology in a more seamless way within the design flow and design exploration.

Different schemes can be applied for the automatic determination of the load increment. Simple schemes can typically be linear or quadratic with respect to the number of iterations. Although efficient for certain structural systems, these don't offer a granular control over the sizing of the increment. More advanced methods include procedures which adapt the load increment for each step, therefore achieving a very fine control on the loading process. So far, one of the most efficient adaptive schemes has been proposed by Ramm [Ramm 1981], who suggested to adapt the step size in relationship to the number of iterations of the previous loading step I to a desired number of iterations I_k. Following this scheme, the current load step s is calculated in the following manner:

$$s = s_0 \left(\frac{I}{I_k} \right)^\kappa,$$

(4.42)

where s_0 is the previous load step and k is a factor that controls the scaling of the load step. Ramm suggests using the square root of the quotient I/I_k, hence the factor k which typically assumes values in the range $0.1 < k < 0.5$, where 0.5 would coincide with the square root. Lower values of k lead to a less steep load increment, therefore increasing the overall calculation time but also decreasing the risk of non-convergence. Following experience by the author, higher values of k are normally non suitable for complex systems, where the best values are between 0.2 and 0.4.

The method proposed by Ramm has been implemented in SOFiSTiK by the author as part of this work. The idea was first introduced by J. Lienhard [Lienhard 2014] in the context of his research, and following extensive discussion subsequently implemented and improved by the author. The implementation makes use of internal routines that divide the loading in several steps and keep track of the number of iterations needed for each step. A complete breakdown in pseudocode is reported below:

```
SOFiLOAD
        DEFINE load
        DEFINE main loadcase = mlc
END

ASE
        DEFINE starting loadcase factor = s
        // generally s = [0.001, 0.01]
        DO
                DO
                        solve loadcase lc = s*mlc
                        IF lc converged
                                CONTINUE
                        ELSE
                                s = 0.5*s
                UNTIL lc converged
                IF s < 1.0
                        s0 = s
                        s = s₀ (I/Iₖ)ᵏ
        UNTIL s = 1.0
END
```

The above SOFiSTiK code snippet allows to considerably speed up the calculation time as the loading factor adapts dynamically to the number of iterations required to perform the calculation step. For nonlinear analysis of large deformations this approach has demonstrated to be invaluable to better handle the overall calculation time.

In conclusion, in the present chapter the relevant concepts on the mechanical behaviour of plates was introduced. An important focus was set on the analytical description of the limits of deformation of planar elements and the direct relationship to Gaussian curvature. Interestingly, the same results were derived in geometrical form in chapter 3 in the discussion on plane isometries and Gauss' Theorema Egregium. This closes the loop of the dual geometrical and mechanical treatment of plates and planar elements in general. The simplified relationships introduced in the continuation of the chapter and the numerical tools employed for the simulation of large deflections provide the main tools that were employed for the design and analysis of the case studies that will be presented in the following chapters.

5. Form conversion approach

In this chapter, we delve into the devised strategies to induce Gaussian curvature through the means of elastic bending of plate-based structural systems. Many strategies exist, and a brief overview of relevant methods will be presented in the introduction to the chapter. The main focus will be set only on existing approaches that make use of plates in their underformed state and elastically bent to achieve global curvature. In particular, these methods will be analysed from a geometric point of view to understand the compromises required to induce Gaussian curvature employing exclusively planar elements. The chapter will then proceed by introducing the form conversion approach that was developed as part of this research along with the presentation of the built prototypes that make use of this strategy for the construction of lightweight shell structures. The exposition of the form conversion method will be followed by a detailed discussion on the mechanical behaviour of these structures and a comparisons between the different discretisation methods and their continuous counterpart as well as discrepancies from the base surface.

5.1   Shape forming strategies of plate structures

Chapters 3 and 4 have been devoted to the explanation of the geometrical and mechanical limits of plate bending. It was seen that large deformations of plates can occur only under axial bending, as stretching will not produce a noticeable effect in the change of geometry. This means that the only configurations achievable are combinations of developable strips. Therefore, the question that naturally arises is how planar elements can be employed to induce curvature in a structure. Many strategies exist and have been developed for this scope, but some fundamental aspects can be recognised. From a geometric point of view, if planar or at most single curved elements are used, some other characteristics of the base surface must be sacrificed. The discrete shell will not possess a continuous curvature everywhere, but will rather be the assembly of locally smooth patches with zero Gaussian curvature. Observed locally each patch will be either flat or a portion of a cylinder or cone, but globally double curvature will still be perceived in the structural system.

ICD/ITKE Research Pavilion 2011

FIG. 5.2

ICD/ITKE Research Pavilion 2011. The Gaussian curvature is concentrated in the vertices
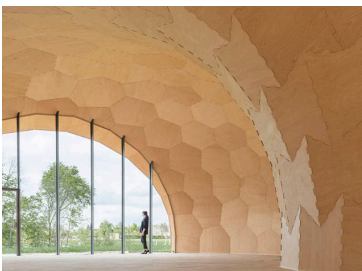
FIG. 5.3

Landesgartenschau Pavilion - ICD/ITKE

In general we can distinguish between three different approaches depending on specific geometrical qualities. These can be grouped as following:

1. Shells made of planar plates. This is the case of segmented shells. The curvature happens in the vertices.
2. Edge coupling of developable strips. The curvature is concentrated along the edges of the neighbouring strips.
3. Overlapping of developable strips. The curvature is completely taken by the voids.

We first consider assemblies of planar elements. In this case the whole double curvature is "concentrated" at the edges of adjacent elements and at their vertices. The double curvature of the geometry can be evaluated using the discrete curvature algorithms discussed back in chapter 3. This would be for instance the case of any discrete mesh approximation of a three-dimensional surface. The challenges concerning this kind of construction logic mainly concern the planarization of the elements. Many algorithms and computational strategies have been developed in recent years for this specific task, as the latest trends in architectural design are pushing ever more towards the rationalisation of freeform shapes. Examples of this approach can be found in many architectural and structural applications. Here we recall two recent prototypes that make use of this idea: the ICD/ITKE Research Pavilion 2011 (Fig. 5.1, Fig. 5.2) and the Landesgartenschau Pavilion also by ICD and ITKE (Fig. 5.3). Both pavilions employ similar structural principles and required each single panel to be planar. Despite the local planarity of the elements, the global perception is that of a double curved surface. It is clear that more elements better approximate the curvature.

The second approach distinguishes itself from the first one for the use of bending. In this case the initially planar elements are now curved in one direction, meaning that the Gaussian curvature of the initial base surface can be approximated better. For a set of continuously bent strips, the curvature will completely occur at the joining of the edges between neighbouring elements. The sharp kink that arises along the line of contact makes up for all the curvature lost in the single curved strips. The bent elements add an enhanced sense of continuity to the structure, as the hard transitions of a discontinuous shell of the first type is partially smoothened out by the single curvature of the strips. The main challenges for this kind of approach rely on the fabrication of suitable connections between the elements. As the contact between the strips happens in a very narrow zone, namely the thickness of the elements' edges, it is necessary to resort to advanced CNC and robotic manufacturing resources to create the connections. Despite the scarceness of examples, this approach has lately been gaining growing interest in the research community. Notable examples can be found in the work of Pottmann et al. [Pottmann et al. 2008] who have been focusing on the panelisation of double curved surfaces with developable strips, the so called D-strips (Fig. 5.4). Other interesting examples can be found in the work of Krieg (Fig. 5.5) and recently by Brütting (Fig. 5.6), the first with a strong focus on fabrication aspects [Krieg and Menges 2013] and the latter on mechanical features of cross-laminated plywood strips and how to steer the inherent anisotropy of the material [Brütting 2016].

The last approach listed at the beginning of this paragraph is the main topic of discussion of this chapter. The ability of multidirectional bending strips to span several directions is the fundamental aspect that led to the development of the *form conversion* approach. This method was termed "form conversion" as there is a 1:1 correspondence between the input surface and the discrete bending shell which is the outcome of the conversion process. In this way a high degree of precision is achieved and deviations from the original shape are minimised. The main difference between the form conversion and the other approaches seen so far lies in the concentration of double curvature in the voids that develop between the bending-active elements. The advantages listed here obviously do not come for free, as the holes introduced in the continuous shell take a toll on the load bearing capacity of the structure. In the following paragraphs this effect will be analysed and quantified. In conclusion, different strategies for the induction of Gaussian curvature using planar or bent elements have been listed. This introduction served as a qualitative overview, in particular to understand where the double curvature arises and gets concentrated for the different cases.

FIG. 5.4

Bulbous bow. From EvoluteTools D.Loft
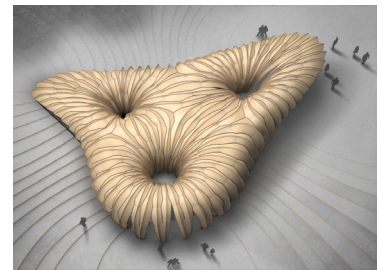
FIG. 5.5

Connecting Intelligence. Master thesis by Oliver David Krieg
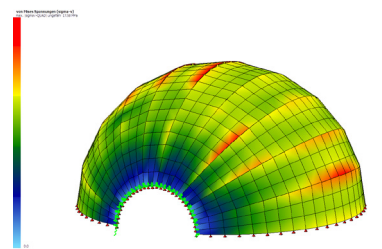
FIG. 5.6

Bending-Active Segmented Shells. Master thesis by Jan Brütting

von Mises stress
N/mm2

100.0

50.0

0.0
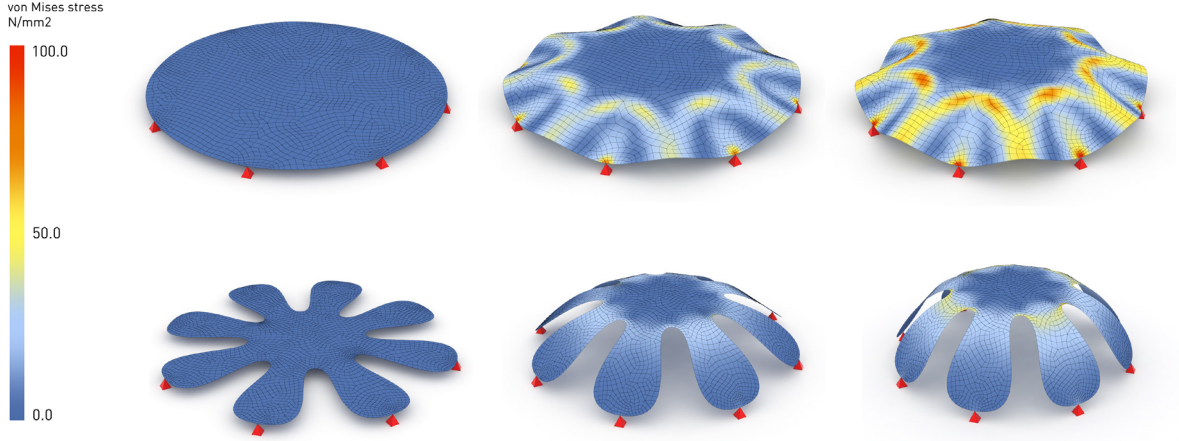
FIG. 5.7

The *form conversion* principle. By strategically removing material from the surrounding, the radial strips of the plate are free to bend

5.2 Form conversion

The principal limit to the formal potential of bending-active structures lies in the restrictions on the material formability. The only deformations that can be achieved within stress limits are the ones that minimise the stretching of the material fibres. For strips and plate-like elements, these reduce to the canonical developable surfaces: cylinders and cones. Attempting to bend a sheet of material in two directions will either result in irreversible, plastic deformations or ultimately failure. Such a strict requirement severely limits the range of structural and architectural potential for plate-based bending-active systems. To expand the range of achievable shapes, it is therefore necessary to develop workarounds for the induction of Gaussian curvature. To overcome such limitations, multidirectional bending can be induced by strategically removing material and freeing the strips from the stiffening constraint of the surrounding. A similar approach is presented by [Xing et al. 2011] and referred to as *band decomposition*. The key principle is illustrated in Fig. 5.7. Here a full disc is bent by applying a support displacement towards the centre. The von Mises stress plots show the stress concentrations that arise in the material as a consequence of the non-isometric deformation that the disc undergoes. If material is strategically removed from the disc as shown in Fig. 5.7b, the radial strips are now free from the constraint of the neighbouring material and can be easily bent into shape. Moreover, the stress levels are radically reduced as the elements are only subjected to non-extensional deformation. Only at the intersection between the petals a small area of stress concentration arises. This is due to the higher bending stiffness of the intersection area as the section width of the strip drastically increases in that area.

To better illustrate the concept, a continuous rectangular plate is reduced to two orthogonal strips (Fig. 5.8a).

70
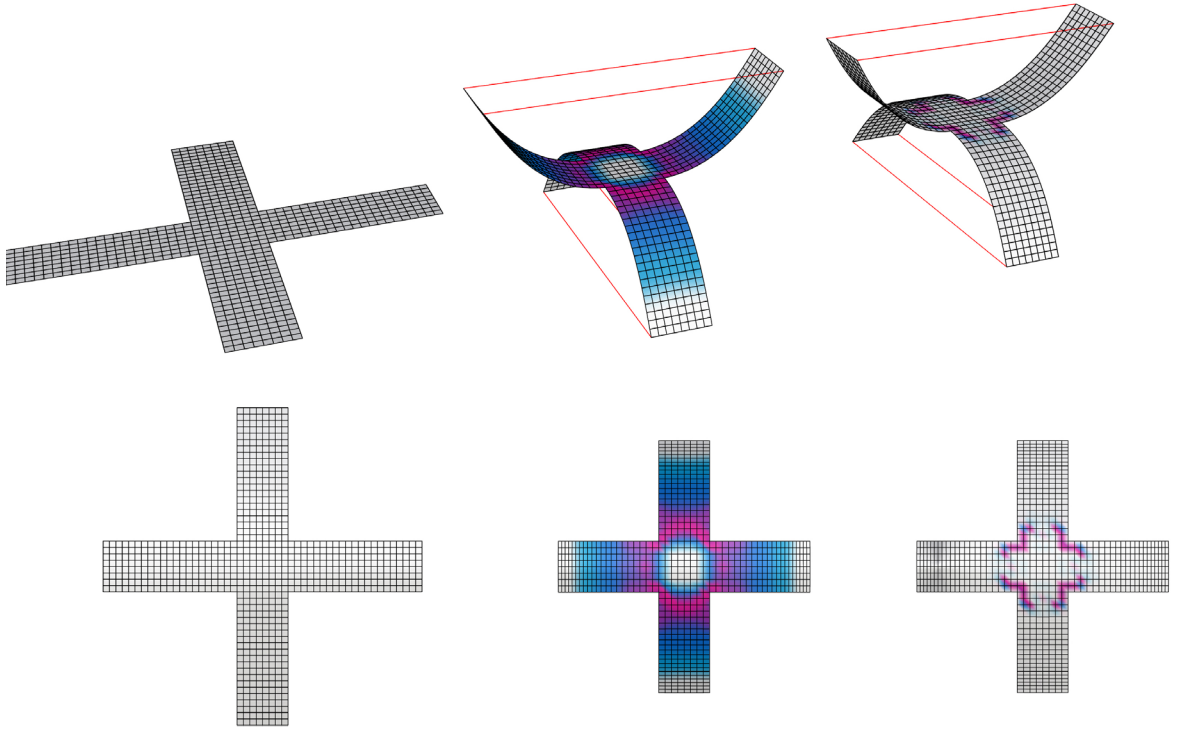
The strips are later bent into opposite directions in a finite element simulation using the ultra-elastic contracting cable approach based on [Lienhard, La Magna and Knippers 2014]. The bending stiffness of the plate, depending proportionally on its width b, results in a radical increase of stiffness in the connecting area between the strips. As a result, the connecting area almost remains planar, and therefore the perpendicular bending axis remains unaffected by the induced curvature. In this way it becomes possible to bend the strips around multiple axes, spanning different directions but still maintaining the material continuity of a single element. Fig. 5.8b depicts the resulting von Mises stresses calculated at the top fibres. The gradient plot clearly displays an area of unstressed material at the intersection between the two strips, as expected based on the previous arguments. A local stress concentration appears at the junction of the strips due to the sharp connecting angle and inevitable geometric stiffening happening locally in that area. This result can be compared with Fig. 5.8c, which displays the Gaussian curvature of the bent element. From the plot it is clear that the discrete Gaussian curvature (based on [Meyer et al. 2003] as seen in chapter 3) of the deformed mesh is everywhere zero, apart from a small localised area at the intersection of the two branches. This confirms that, within stress limits, flat sheets of inextensible material can only be deformed into developable surfaces at most.

FIG. 5.8

a. Orthogonal strips, b. Von Mises stress plot of the bent strips, c. Discrete Gaussian curvature plot of the bent strips
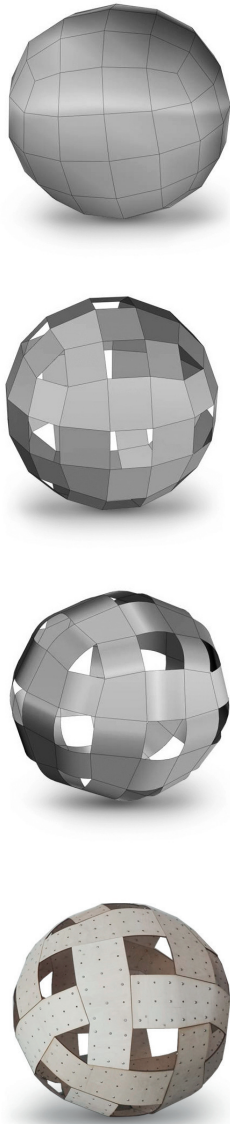
71

Based on the strip approach defined so far, the general procedure for an arbitrary freeform surface is summarised in the following steps:

1. Mesh the target surface (Fig. 5.9a).
2. Perform an interior offset for each face of the mesh.
3. Connect the disjointed faces by creating a bridging element; two faces initially sharing an edge will be connected (Fig. 5.9b).
4. The bridging element is modified to take into account the bending curvature. Assuming that the start and end tangent plane of the bridging element coincide with the surfaces to be connected, the element can be defined through a simple loft (Fig. 5.9c).
5. Unroll the elements.

Fig. 5.9d shows the 1 meter diameter plywood sphere realised to assess the validity of the decomposition principle. The prototype employed double layers of 3.5 mm plywood sheets, assembled in a criss-cross manner to increment stability and ensure a proper overlapping of the elements at the location of the seams.

With this method it is possible to span multiple directions with varying degrees of local curvature, therefore faithfully reproducing the global curvature of the source geometry. Taking as an ex-ample the 4-branched element above, different combinations of bending directions will reproduce discrete versions of different curvature points. For instance:

1. A positive rotation around the local y axis of each branch will produce an area of positive Gaussian curvature (Fig. 5.10a).
2. A positive (or negative) rotation around the local y axis of two branches will produce a cylindrical area of zero Gaussian curvature (Fig. 5.10b).
3. Positive rotation around the local y axis of two branches and a negative rotation of the remaining ones will produce an area of negative Gaussian curvature (Fig. 5.10c).
4. A negative rotation around the local y axis of three branches and a positive rotation of the fourth one will have the effect of building a local monkey saddle (Fig. 5.10d).

The previous remark demonstrates the universal character of the method. Virtually any shape, no matter the complexity of it, can be physically reproduced following the form conversion process (Fig. 5.13). The only constraints here

FIG. 5.9

Form conversion of a sphere test case. a. Mesh of target surface, b. Offset and edge bridging, c. Bending of bridging elements, d. Plywood prototype of sphere test case

are imposed by the limits of the material and the achievable bending radii. For architectural and structural applications this method is very well suited, as the radii of curvature are normally not extremely pronounced compared for instance to sheet metal forming for the automotive industry.

Despite the formal freedom deriving from the decomposition process, it is necessary to highlight how the method is intrinsically dependent on the mesh topology of the source geometry. This is intuitively obvious as the source mesh uniquely defines the geometry of each panel through the offset operation (Fig. 5.11). As the core areas of each element are built from an interior offset, every deviation from the plane will automatically be retained in this phase. This generally contradicts the assumption that the core area remains planar and unstrained during the bending process. Based on practical experience though, it has been noticed that it is almost always possible to find a geometrical configuration of the banded structure that eliminates curvature in the core areas and shifts all the geometrical deviation to the branches. In this way it is possible to guarantee that the central connecting piece will retain its planarity even after the unrolling process takes place.

Concentrating all the deviation from planarity to the branches has the undesirable effect of introducing double curvature and therefore strain in the branches. Despite being detrimental to the formability of the elements and incrementing the internal stress state of the form-finding process, the stress levels are typically within the limits of the material. This achieves a combined bending and torsional effect acting on the branches due to misalignment of the edges of the offset mesh. As seen in chapter 3 dedicated to the mechanics of strips, this combined action can be checked in the early stages of design to make sure that the deformation state is not prejudicial to the safety of the structure.

The optimality of the bridging between cores can be checked over the relative orientation of the connecting edges. In the optimal case the two edges are coplanar and this will lead to a single curved bridging element. Only bending will be involved in this way (Fig. 5.12a). Any deviation from this configuration will be compensated by local torsion of the strip, resulting in normal bending stress accompanied with tangential torsional stress (Fig. 5.12b). Using von Mises' yield criterion the general plane stress state is easily recovered.

The described form conversion method uniquely defines the dual decomposed mesh seen in Fig. 5.11. Based on the assumptions made so far, due to the larger cross sectional area and to the localised stiffening the central core remains planar also throughout the assembly process. Following this argument, the core elements in Fig. 5.11c are geometrically
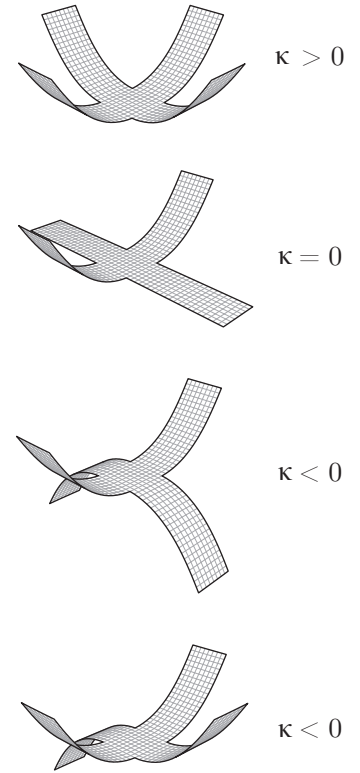
FIG. 5.10

Local curvature values a. Positive Gaussian curvature (synclastic surface), b. Zero Gaussian curvature (cylindrical surface), c. Negative curvature (anticlastic surface), d. Monkey saddle

$\kappa > 0$

$\kappa = 0$

$\kappa < 0$

$\kappa < 0$

Offset

Core   Branch
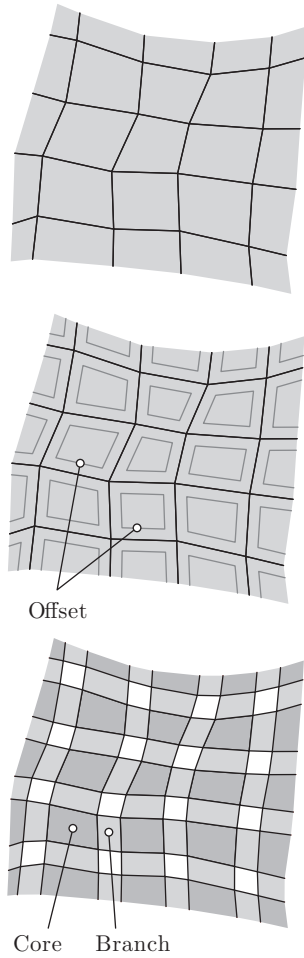
Breakdown of the form conversion process

Tangent direction
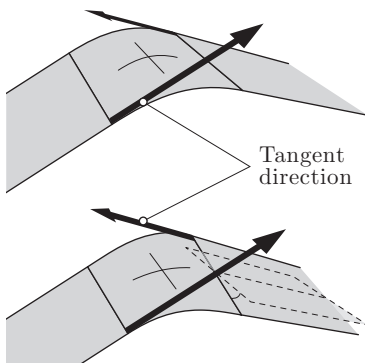
a. Coplanar neighbouring edges will only have bending in the branches, b. Non-coplanar neighbouring edges will have bending and torsion in the branches

identical to the fabricated counterpart and do not undergo further manipulation. Fig. 5.12a illustrates the following steps leading to the final geometry. Assuming planarity of the cores, the normal of the face is uniquely defined, and so the tangent plane in which the face lies. This also identifies the starting direction of the bridging element, as this vector will be perpendicular to the starting edge and will lie on the very same tangent plane. Intuitively, it is obvious that the bridging element, sharing the core's starting edge, will also be tangent to it. The start and end tangent directions are therefore entirely defined by the neighbouring elements, which can be used to generate the missing items. The available elements are sufficient to generate a loft surface between the start and end edge and the tangent directions correctly aligned with the neighbouring central core. In this way we generate the elements of the deformed geometry to be unrolled.

The band decomposition method presented in this chapter was developed in its original form by Akleman et al. following rigorous arguments from topology and graph rotation system theory arguments, and the results published in a series of scientific publications [Akleman et al. 2010]. Their theoretical work is often accompanied by small scale paper prototypes meant to elucidate and verify the topics presented. Interestingly, late developments by Akleman and his team are pointing towards self-folding structures and the integration of smart materials as shape memory alloys to create self-assembling objects. The advantages of bending and the associated large deformations are here mostly evident, as the large rotations of the connecting bridges allow to pronouncedly change the shape of the continuous, flat strip. In comparison to Akleman's work and literature, the present research distinguishes itself by focusing on the implementation of large scale structural systems with architectural potential and concentrating on engineering related aspects less evident at smaller scale.

A fundamental aspect independent of the scale of the system is the sequence of assembly and the shape forming process. The question raised here is to understand whether it is necessary to follow a specific assembly sequence to achieve the final shape and how this is influenced by it. This aspect is demonstrated rigorously in [Xing et al. 2011] and expressed by the Hefter-Edmunds theorem of graph rotation systems, which "asserts that there is a bijective correspondence between the set of pure rotation systems of a graph and the set of equivalence classes of embeddings of the graph in the orientable surface". Without entering technical details that go way beyond the scope of this research, it suffices to report that "as a direct consequence of the theorem, to assemble the structure, the builder must simply attach the corresponding

edge-ends of vertex components. Once all the components are attached together, the whole structure will correctly be assembled". This is an astonishing feature, as it simplifies the need of embedding sequential assembly operations. The whole structure can therefore be assembled without following a predetermined sequence pattern, a most desirable aspect especially when the complexity of the object might require different stages of construction. This aspect can be well understood by considering the assembly process of the case studies. No additional information was required for the assembly as only the topological arrangement of the elements was sufficient to correctly raise the structure.

The construction guarantees preservation of the local and global Gaussian curvature characteristics of the base mesh, resulting in a close approximation of the original surface. Gaussian curvature is an extremely useful measure to evaluate the shape and structure of surfaces. It relates to the topology and geometry of the surface through the Gauss-Bonnet Theorem, which implies that for a manifold *M*, the Gaussian curvature must be equal to 2π times $\chi(M)$, the Euler characteristic of the corresponding surface as seen in chapter 3. For instance, for a genus-0 manifold mesh, this sum must be equal to 4π. On the other hand, for genus-1 surfaces, the Euler characteristic is zero.

Since the form conversion structure is made only of flat or single curved components, the Gaussian curvature is zero everywhere on the solid parts. The Gaussian curvature happens only in the voids that are uniquely determined. Since the Gaussian curvature of the holes is correctly formed, the structure will always be raised and formed in three-dimensional space, closely approximating the overall shape of the initial surface.

Following the exposition by Akleman, the process converts polygonal meshes to structures that are composed of operative vertex components, i.e. the vertices of the mesh. For the starting polygonal meshes, we employ the discrete version of Gaussian curvature seen in chapter 3. The discrete Gaussian curvature for vertices of triangular (or planar) meshes is also known as the vertex defect, and for every vertex of a piecewise planar mesh it is defined as:

$$\Theta = 2\pi - \sum_{i}^{n-1} \theta_i,$$

(5.1)

where θ_i is the angle at corner i of the vertex and n is the valence of the vertex.

The resulting structures represent the dual of the original polygonal mesh. Therefore, the faces (i.e. the holes) of the structure correspond to the vertices of the original mesh.

On the other hand, the vertices of the structure (the vertex components) correspond to the faces of the original mesh. Note that the faces of the original mesh are either planar or approximately planar. It is therefore easy to create the vertex components, which can be fabricated with developable materials such as paper, plywood or even thin metal. When using developable materials, if there is only inextensional deformation and the elements undergo pure bending, regardless of the level of bending of each element the Gaussian curvature will remain zero. In other words, the Gaussian curvature happens only at the holes of the structure. Since the holes correspond to the vertices of the original polygonal mesh, the Gaussian curvature of any hole must correspond to the discrete Gaussian curvature of its corresponding vertex in the original polygonal mesh.

Note that the discrete Gaussian curvature for a face directly depends on the face defect and is defined as:

$$\Phi = \sum_{j=0}^{n} \phi_j - (n-2)\pi, \qquad (5.2)$$

where ϕ_j is the angle at corner j of a hole and n is the number of the sides of the hole. Therefore we have retrieved a way to compute the Gaussian curvature for the holes of the structure. To make the Gaussian curvature of every hole Φ equal to Θ of its corresponding vertex in the original mesh is straightforward. Let ϕ_i and θ_i be two corresponding corners of a hole in the structure and its corresponding vertex in the original mesh. If we choose $\phi_i = 2\pi$ - θ_i, then $\Phi = \Theta$ for such corresponding hole-vertex pair. In this way we have demonstrated that the double curvature of the initial polygonal mesh is completely absorbed, and correctly represented by the holes of the decomposed structure [Hernandez et al. 2013].

The presented form conversion method maintains general validity for any arbitrary source mesh. There are no restrictions in the base design model. In the case of an Ngon mesh, its banded dual will have strips with N arms departing from the central core element. The geometry of the voids is defined by the valence of the mesh. For the sphere example a 4-valent source mesh produces square voids throughout the banded structure. A tri-valent hexagonal mesh would produce triangular voids and so forth. This is shown in Fig. 5.13, where several objects discretised with meshes of different geometry and topology are shown decomposed following the method described above. The only limitations concern the planarity of the initial polygonal mesh faces, which can easily be fixed as mentioned previously. In the next sections a series of prototypes built following the rules for form conversion listed here will be presented.

76

5.3   Case studies

The form conversion approach for bending-active plate structures was tested on three full scale prototypes. Each case study presents different characteristic in geometry, topology, shape and materials employed. Nonetheless, the core generative strategy remains the same for all three cases.

To take advantage of the bending deformations, the prototypes had necessarily to be built out of thin sheets of material. As usual, the compromise on the formability of the strips takes a considerable toll on the load bearing capacity of the shell. To counteract this detrimental effect, for two of the three constructions, coupling between the two layers had to be developed. In this way a multiple layered shell with distributed shear connectors between top and bottom skin is constructed.

Besides adopting these construction measures, the main stiffness of the prototypes actually derives from the geometric stiffening effect of the double curvature of the shape. Apart from being the main objective of this research, the induction of Gaussian curvature in the system was essential to ensure enough stability in the prototypes. Therefore it can be said that it is geometry that does all the work rather than the amount of material or thickness of the cross-section. In this way the reduced cross sections are compensated by the increased geometric stiffness of the curved shell. Also for this reason the shape of the prototypes were chosen to accentuate this geometric feature, therefore guaranteeing increased stability besides displaying the construction and rapid assembly capabilities of the form conversion method.

Concerning the shape of the prototypes, intuitively it would make sense to resort to optimal shell geometries as known from the work of Isler, Candela, Otto and others. The core difference though is that in those cases the shells are compressive structures which carry load mainly via membrane action, where the self-weight is always the dominant load case. This ensures that the force transfer occurs via compression within the cross-section of the shell. For thin, lightweight shells this principle does not apply anymore. The reduced cross-section cannot ensure a proper transfer of compressive loads as it would buckle way too easily. For this reason, bending-active shells have to rely on bending both for its form-giving qualities and also for carrying external loads, as self-weight can often be disregarded.

Finally, a characteristic of discrete shells is that globally they behave similarly to their continuous equivalent, but on a local scale the behaviour of the individual elements becomes more dominant. All these aspects will be discussed further in detail in the sections dedicated to the structural behaviour of discrete bending-active shell structures.

Snap It Up. Diploma thesis by Nicola Haberbosch and Andreas Schönbrunner under supervision of the author

5.3.1 Snap It Up

The first case study was developed in collaboration with students Nicola Haberbosch and Andreas Schönbrunner as part of their diploma thesis at the University of Stuttgart. This prototype served as a kick starter for this part of the research and the realisation of the following case studies. Despite having developed the prototype in a more intuitive and empiric fashion compared to the next case studies, the approach adopted for the first shell is the same as the form conversion method that was described previously. All the results and information described in the next sections have been published in a joint publication by the authors in [Schönbrunner et al. 2015].

The system was built in a prototypical scale (2.6 m x 1.9 m x 2.0 m) using thin sheets of 0.5 mm and 0.75 mm PET-G. The structure consists of two basic elements: a series of strips which form the upper and the lower surface, and pairs of truncated cones that act as spacers between the two-layered structure (Fig. 5.14). The form of a truncated cone was chosen as spacer because it can resist area loads in the direction normal to the surface and at the same time maintain the ability to undergo snap-through buckling when loaded at certain points. These cone elements are populated over the entire surface and are used to provide both structural height and increased interconnectivity between the layers where structurally necessary. Besides providing the necessary shear connection between the two layers, the cones serve as an interruption over the continuous surfaces, therefore creating the necessary voids that allow multidirectional bending to take place in the layer strips. In the structure, a connection similar to mortise and tenon joints are used to connect the strips of the upper and lower layer with each other as well as cross-connecting them with the pairs of truncated cones.

To additionally increase the structural performance of
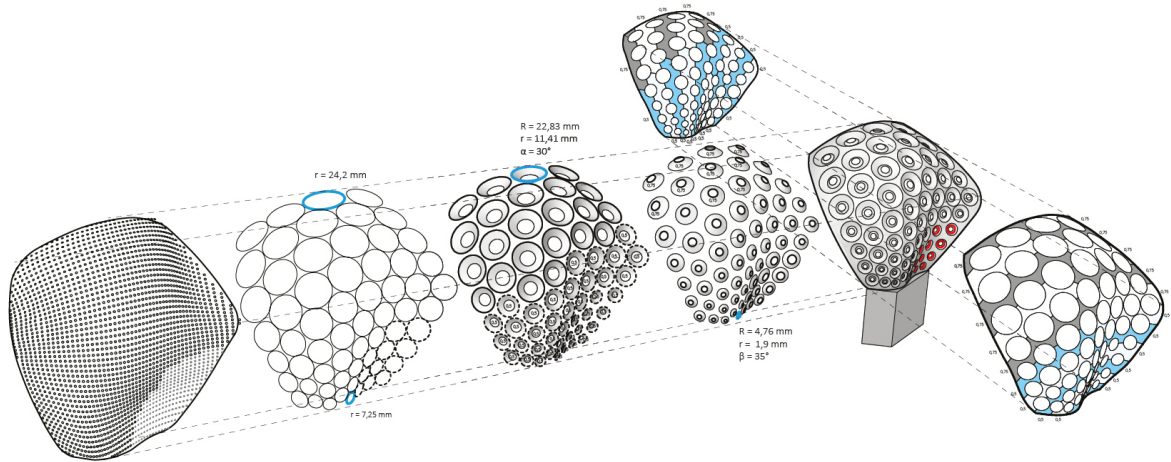
the system and reduce the material usage, the height of the sandwich structure varies based on the information of a previously conducted Finite Element Analysis. Areas of high bending moments are met with higher cones that provide more static height, whereas high shear forces are coped with a higher density of cones, which locally increases the interconnectivity of the sandwich layers. Since there is a distinct relationship between the radii of the cones and the sandwich height, circles are placed computationally onto the target surface with varying radii. These circles lead to different cone sizes and therefore sandwich heights.

   In order to connect multiple structural elements into the desired shape, a bio-inspired snap-through effect was used. The connection logic implements this effect in order to join individual parts together without the need for auxiliary tools or special fasteners. During the assembly process, the tenons of the cones are inserted into the mortises of the strips, which already connects them loosely together. By snapping the cones a first time into their inverted stable condition, the previously loose connection becomes fastened, which is due to a combination of surface friction and geometric restriction. This process is then repeated for all mortise and tenon joints at the top and the bottom layer. After connecting all the cones to the top and bottom layers, the structure is still somewhat flexible. Snapping the cones a second time, however, this time only partially and in opposite direction, finally locks the layers tightly to each other and makes the structure finally very stable.

   A computational tool developed for this case study uses an abstracted geometry to enhance the computing performance and to enable the unrolling process of the stripe elements. The abstraction neglects details such as the mortise and tenon joints and creates the surfaces only to obtain a de-

a. Simplifying the double curved surface to developable strips,
b. Strips abstraction, c. Detail of built prototype
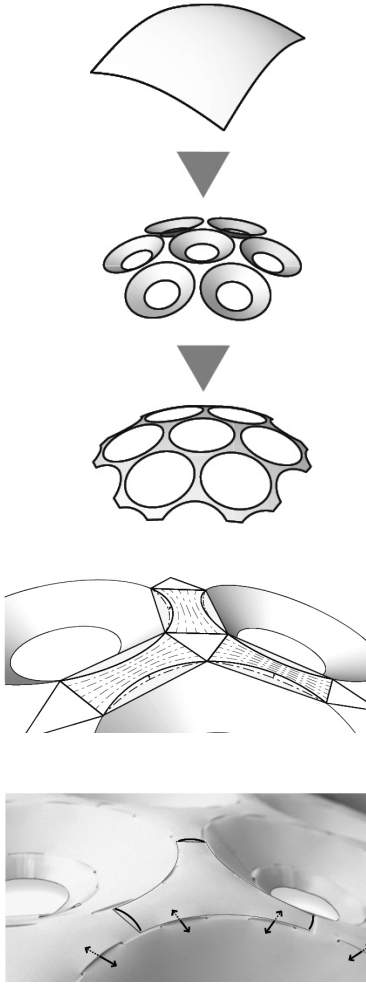
velopable topology which maintains the key geometrical information during the unrolling process (Fig. 5.15).

The curvature of the system is created in a way comparable to the free-forming of laminated sheets: the top and bottom layer are bent individually and then fixed in shape by the shear connectors, which in this case are the truncated cones. The double curvature can be achieved by perforating the outer layers so that the desired global curvature can be simplified to a grid of single curved stripes (Fig. 5.16a). The remaining triangular areas negotiate the transversal curvatures (Fig. 5.16b). Little deviations of the computational model from the built system are acceptable due to possible tolerances in the connection (Fig. 5.16c). Incorporating findings gathered during the previous project allowed for a controlled and precise abstraction process.

To ensure that the shear connecting cones could be snapped by hand, parameters restricting their proportions and dimensions were identified in physical tests and incorporated into the design tool. In order to allow for the second snap-through buckling, the top and the bottom cones of one connection pair needed to have different angles resulting in different radii touching top and bottom surface. For changes of the curvature direction (convex, concave) the orientation of the cone pair needed to change accordingly. For synclastic regions this orientation could be processed easily since both principal curvatures have the same direction. Only anticlastic regions needed further investigation as the principle curvatures have the larger absolute value and are therefore decisive for the orientation.

The generation of the 3-D model could be broken down into three major steps. After analysing structural properties and the Gaussian curvature of the target surface, the digital model is populated employing a circle packing algorithm based on the structural needs and results following the material tests. Eventually, the abstracted cone surfaces were created and the gaps in between the cone pairs were filled with the developable surface strips which constituted the top and bottom layers of the shell (Fig. 5.15). In order to minimise the self-weight of the structure, a differentiation of the material thickness was introduced. For the developed mock-up the surfaces were organized in groups of 0.5 mm and 0.75 mm Vivak® sheets based on material limitations. The top and bottom surfaces were joined in developable groups of strips. To prevent the structure from being weakened by continuous structural cuts, the strips were split in different directions on the top and bottom layer. After unrolling, the abstract surfaces were supplemented by constructive details. The ease of the assembly process allowed the erection to take place in only a few hours.

5.3.2 Berkeley Weave

The second case study investigates the design potential emerging from integrating both bending and torsion of slender strips into the design process. The results are described extensively in the author's publication [La Magna et al. 2016]. A modified Enneper surface acts as a base for the saddle-shaped design (Fig. 5.18a). This particular shape was chosen for its challenging anticlastic geometry with locally high Gaussian curvature. The subsequent conversion process into a bending-active plate structure followed several steps. The first was to approximate and discretise the surface with a quad mesh (Fig. 5.18b). A curvature analysis of the resulting mesh reveals that its individual quads are not planar but rather double curved (Fig. 5.18c).

The planarity of the quads is an important precondition for the later assembly process, as this enables bending of the elements to take place. In a second step, the mesh was transformed into a four-layered woven pattern with strips and holes. Here, each quad was transformed into a crossing pattern of two strips in one direction intersecting with two other strips in a 90-degree angle. The resulting interwoven mesh was then optimised for planarisation. However, only the regions where the strips overlapped were forced to be planar (blue areas), while the quads between the intersections remained double curved (Fig. 5.18d). A second curvature analysis illustrates the procedure and shows zero curvature only at the intersections of the strips while the connecting arms are both bent and twisted (Fig. 5.18e). In the last step, this optimised geometrical model was used to generate a fabrication model that features all the connection details and strip subdivisions (Fig. 5.18f).

A closer look at the most extremely curved regions of the structure shows the complexity related to the last generation
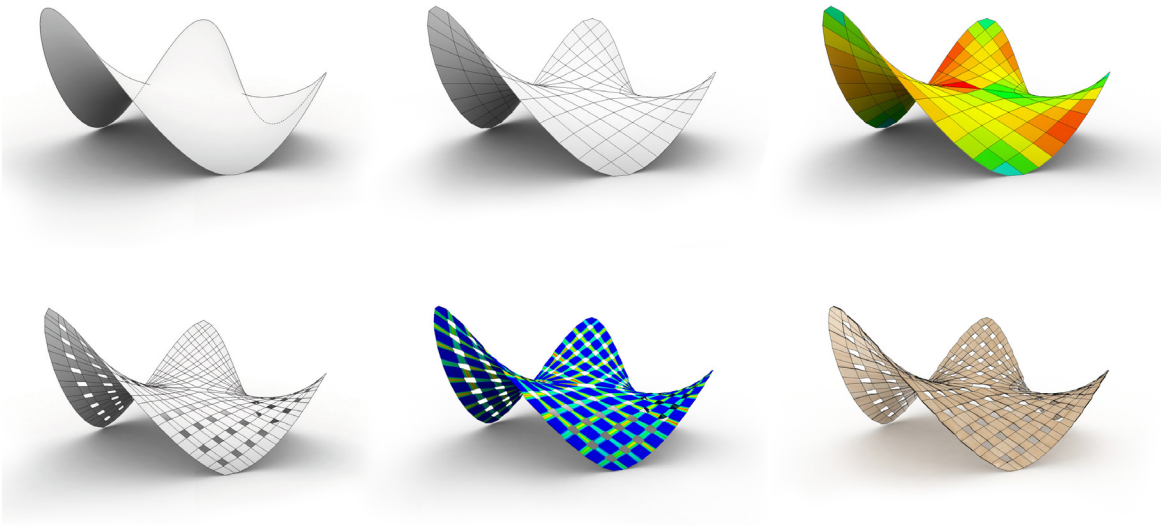
Generation process and analysis.
a. Base geometry, b. Mesh approximation, c. Curvature analysis,
d. Conversion to bent plates,
e. Curvature analysis, f. Fabrication model

step (Fig. 5.19a). To allow for a proper connection, bolts were placed only in the planar regions between intersecting strips, therefore leaving the double curved elements free to span between the central pieces. Since the strips are made exclusively of smaller segments, it was necessary to control their position in the four-layered woven structure and also the sequence of layering process. A pattern was created which guaranteed that strip segments only ended in layers two and three which were clamped by continuous strips in layers one and four. A positive side effect of this weaving strategy is that the gaps between segments are never visible and the strips appear to be made out of one, continuous piece. The drawback, however, is that each segment has a unique length and requires specific positions of the screw holes (Fig. 5.19b).

To demonstrate proof of concept for this design approach, this case study was built in the dimensions of 4 m x 3.5 m x 1.8 m (Fig. 5.17). The structure was assembled out of 480 geometrically different plywood strips fastened together with 400 similar bolts. The material used was 3.0 mm thick birch plywood. The 3.0 mm plywood employed for the Berkeley Weave project was composed by three cross-laminated birch veneers. The uneven number of laminas and the reduced cross-section makes the plywood extremely sensible to orthotropic behaviour. The nominal Young's modulus in the direction of the top and bottom grain is $E_{\parallel} = 16471$ N/mm^2, whilst in the orthogonal direction $E_{\perp} = 1029$ N/mm^2. Despite the high anisotropy of the plywood used for the installation, the strips where all oriented to in the most favourable grain direction to minimise the strain in the material. This was possible as the individual elements did not span multiple directions as in the case of the previous and the next prototype. Dimensions and material specifications were employed for a Finite

Element Analysis using the commercial software SOFiSTiK. Under consideration of self-weight and stored elastic energy, the minimal bending radii were no smaller than 0.25 m and the calculated stress peaks were still below 60% of the permissible yield strength of the material.

The weaving strategy of the installation guaranteed that the seams between the elements would constantly overlap and always be covered by a continuous strip. In this way no seam is visible in the built prototype. Besides the aesthetical appeal of the weaving, this strategy has the advantage of placing the uninterrupted strips at the top and bottom layer levels. Therefore, the seams between the strips are always in the middle where the neutral surface of the bending elements lies. This has the advantage of placing the discontinuities of the structural system in the area of least mechanical demand.

In the opening section on the details of the form conversion approach, it was mentioned that only the topological arrangement of the strips is required to correctly assemble the structure. The assembly of the Berkeley Weave installation did not in fact require any additional information apart from the connectivity of the elements. This information was easily retrieved from the computational model that served as a base for the definition of the system. The identification system was composed by a numbering and orientation identifier to correctly place the elements. The information was simply etched on the plywood strips during the laser cutting process.

The second of the three prototypes is characterised by the use of combined bending and torsion. This was necessary as the base mesh used to generate the form conversion pattern was only partially planarised. This combined mechanical action on the plywood imposed a higher stress level on the elements compared to situations where simple axial bending is used. On the other hand, it allowed to have less restrictive limitations on the bending and twisting of the elements, and therefore on the global geometry of the piece. It is important to notice that the areas bolted together were planarised to avoid excessive warping in the combined section. As four 3.0 mm plywood sheets come together in that point, a combined cross-section of 12 mm would have been excessively thick to contemporarily bend and twist. This strategy can be applied to any geometry that is generated through form conversion. By concentrating all the deformation in the connecting branches it ensures that areas of higher stiffness remain relatively unstrained. The multiple layers ensured a higher cross-sectional inertia due to the thickness of the combined elements and higher load bearing capacity which could have been even further enhanced by adding more layers to the system.
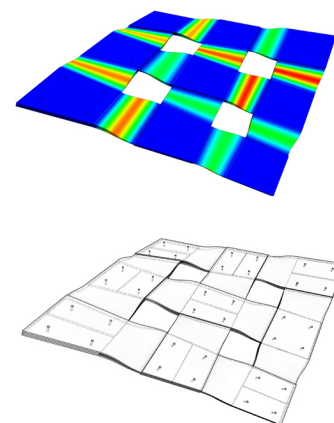
FIG. 5.19

a. Analysis of Gaussian curvature, b. Schematic of the weaving and technical details

FIG. 5.20

Detail of built prototype

FIG. 5.21

View of the Bend9 pavilion

5.3.3 Bend9

The third case study is a multi-layered arch that spans over 5.2 m and has a height of 3.5 m (Fig. 5.21). This project was built to prove the technical feasibility of using bending-active plates for larger load-bearing structures. In comparison to the previous case study, this project showcases a different tiling pattern and explores the possibility to significantly increase a shape's rigidity by cross-connecting distant layers with each other. As for the previous prototype, results are reported in the publication [La Magna et al. 2016].

To fully exploit the large deformations that plywood allows for, the thickness of the sheets had to be reduced to the minimum, leading once again to the radical choice of employing 3.0 mm birch plywood. As for the second case study, the nominal Young's modulus in the direction of the top and bottom grain of the birch plywood is $E_{\parallel} = 16471$ N/mm², whilst in the orthogonal direction $E_{\perp} = 1029$ N/mm². As the individual elements span multiple directions, the bending stiffness heavily depends on the orientation of the branches with respect to the plywood's grain. In theory, this aspect could be integrated in the computational pipeline to orient the elements that bend the most in the weakest direction of the plate, therefore making the pieces easier to bend. In practice, the minimal bending radii were chosen no smaller than 0.25 m so that the bending stress under form-finding was still below 60% of the permissible yield strength of the material.

Since the resulting sheets are very flexible, additional stiffness needed to be gained by giving the global shell a peculiar geometry which seamlessly transitions from an area of positive curvature (sphere-like) to one of negative curvature (saddle-like) (Fig. 5.22a). This pronounced double-curvature provided additional stiffness and avoided undesirable deformation modes
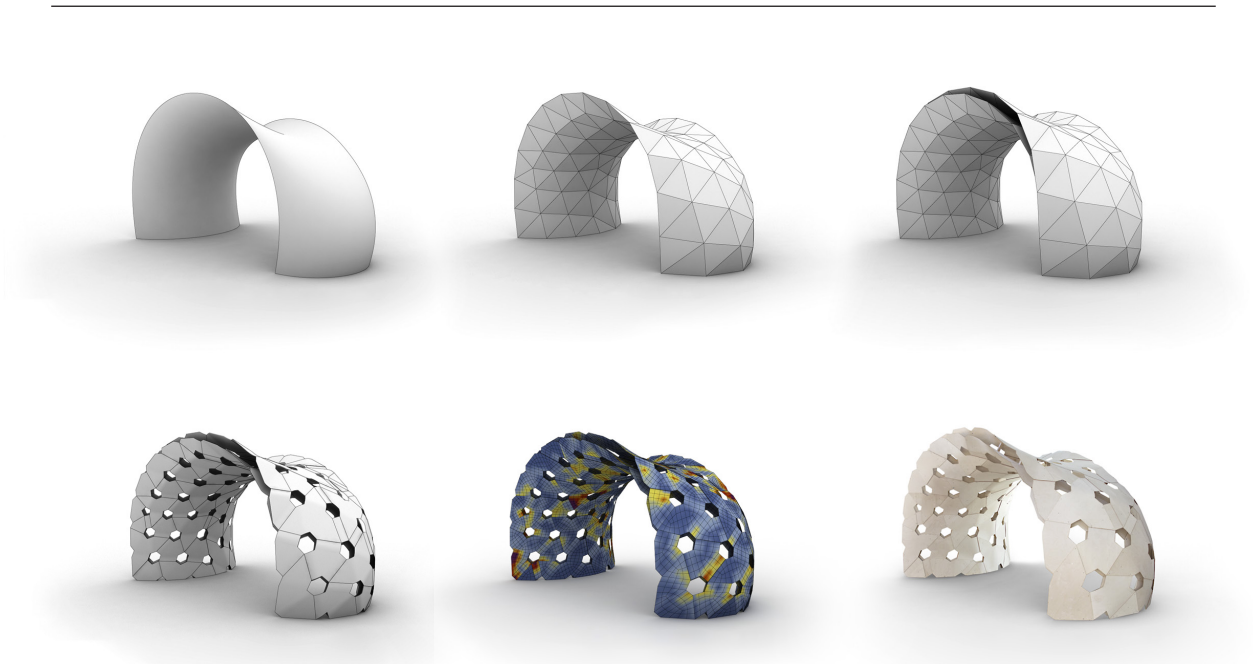
of the structure. Despite the considerable stiffness achieved through shape, the choice of using extremely thin sheets of plywood required additional reinforcement to provide further load resistance. These needs were met by designing a double-layered structure with two cross-connected shells.

As in the previous example, the first step of the process was to convert the base geometry into a mesh pattern (Fig. 5.22b). The third case study employs a triangular base mesh as opposed to the quad mesh of the second prototype. In this way the planarity of the elements is automatically ensured by the geometry of the mesh. In the next step a preliminary analysis of the structure was conducted, and a second layer was created by offsetting the mesh. As the distance between the two layers varies to reflect the bending moment calculated from the preliminary analysis, the offset of the surfaces changes along the span of the arch (Fig. 5.22c). The offset reflects the stress state in the individual layers, and the distance between them grows in the critical areas to increase the bending stiffness of the system. (Fig. 5.23) The tiling logic that was used for both layers guarantees that each component can be bent into the specific shape required to construct the whole surface. This is achieved by strategically placing the voids into target positions of the master geometry, as described in the previous section, ensuring that the bending process can take place without prejudice for the individual components (Fig. 5.22d). Although initially flat, each element undergoes multi-directional bending and gets locked into position once the neighbours are added to the system and joined together. The supple 3.0 mm plywood elements achieve consistent stiffness once assembled together, as the pavilion, although a discrete version of the initial shape, still retains substantial

FIG. 5.23

Front view of the Bend9 pavilion

FIG. 5.24

a. Detail of the elements, b. Detail of the connecting elements

shell stiffness. This was validated in a second Finite-Element Analysis that considered both self-weight as well as undesirable loading scenarios (Fig. 5.22e). Finally, a fabrication model was generated and the structure fabricated (Fig. 5.22f, Fig. 5.21).

This form conversion prototype made use exclusively of cylindrical bending for each plate. Only single axial bending occurs in the elements, therefore avoiding the combined effects of bending and torsion. Compared to the previous case studies, the curvature radii that could be achieved in this case were considerably smaller, i.e. tighter curvatures, as only bending stress occurred in the plywood. The adoption of a multiple layering strategy was inevitable in order to achieve the large span of the pavilion. In general, the coupling of multiple layers is the only method that can be adopted to increase the span and the structural qualities of bending-active constructions. Increasing the cross-section of the panels is not a feasible alternative as the bending stress increases by the third power of the thickness.

The built structure employs 196 elements unique in shape and geometry (Fig. 5.24a). 76 square wood profiles of 4 cm x 4 cm were used to connect the two plywood skins (Fig. 5.24b). Due to the varying distance between the layers, the connectors had a total of 152 exclusive compound mitres. The whole structure weighed only 160 kg, a characteristic which also highlights the efficiency of the system and its potential for lightweight construction. The geometry of the base surface was chosen for its challenging shape as the arch transitions from an area of synclastic curvature at one support to the anticlastic curvature of the other support point. The smooth curvature transition and the overall complexity of the shape clearly emphasise the potential of the construction logic to be applied to any kind of double-curved freeform surface.

5.4   Considerations on the limits and applicability

The presented case studies demonstrate the application of the form conversion approach to three different freeform surfaces. The surfaces were chosen to highlight the flexibility of the method to be used for arbitrary geometries. Considerations on the limits and comparisons with other approaches are discussed in the following paragraph.

Limits on the applicability of the form conversion approach mainly derive from the amount of curvature, torsion, or a combination of both in the bridging elements. This value can be directly predicted based on the geometry resulting from the conversion process discussed in paragraph 5.2 (Fig. 5.11, Fig. 5.12). As long as the stress levels are kept within the limits of the material, any surface can be converted using the presented approach. This means that the limits of applicability are dictated exclusively by material and thickness but are independent of geometry. The stress limits for the cases of pure bending, pure torsion and the combination of both have been discussed in paragraph 4.5.

The surface's discretisation plays a crucial role in the conversion process. Triangular meshes, being inherently planar, will always eliminate torsion in the elements. Further attention must be paid in the case of quadrangular and hex dominant meshes, as these may introduce substantial torsion in the plates. This can be controlled by adjusting the mesh to achieve a satisfactory compromise, for instance by densifying the amount of elements in the areas of greater curvature.

In the overview on existing approaches at the beginning of this chapter, alternative methods developed by other authors have been presented. In particular the work of Brütting has been mentioned, as it shares common features to the form conversion approach presented here. As discussed by Brütting in his work, "The strips between two opposing edges need to have a curvature in only one direction and cannot change the curvature direction within one strip [...]" [Brütting 2016]. In comparison, the form conversion approach is not limited in any way by the geometry of the base surface. This means that changes in the sign of curvature are allowed throughout the whole development of the surface. In this way the construction of geometries with arbitrary transitions between synclastic and anticlastic areas is made possible. Moreover, the strip method developed by Krieg and Brütting inevitably requires complex edge connections between the strips. The overlapping between surface areas in the form conversion approach reduces the complexity of the joinery, as a simple bolted connection is sufficient to connect the plates together.

5.5   Structural behaviour

In this chapter the mechanical behaviour of bending-active structures generated through the form conversion approach is evaluated. It has been seen that using the form conversion implies adding a series of voids in the base surface, effectively reducing the continuity of the surface and therefore also the total amount of material involved in the transfer of forces. We are now interested in understanding what effect does this have on the global structural behaviour of the shell and in particular what is the toll taken by the form conversion method.

The analysis of the structural behaviour starts with a thorough comparison between a prototypical hemispherical shell and two sets of form conversion shells, the first set generated from a triangular base mesh and the second set from a quad based mesh. In this way, also the influence of the mesh pattern could be evaluated in the following study cases. To be able to compare the results between the half sphere and the form conversion cases, a full simulation of the wrapping procedure of the unrolled patterns was performed. By doing so, all the information concerning the local bending of the elements post form-finding is retained. This provides all the necessary force and stress values in the elements of the simulation which are needed to assess the influence of prestress on the global structural behaviour.

The chapter on the structural behaviour of form conversion bending-active structures proceeds with the analysis of the influence of pattern density. Variations in the number of elements employed for the discretisation of the base surface are analysed along with changes in the size of the voids aperture. It will be seen that, contrary to the limited effect of prestress, the main structural benefits derive directly from changes in the shell patterning. The limits of the refinement process will be shown in the development of the section, highlighting the best compromises between structural behaviour and system complexity.

To wrap up this section, the results of the Finite Element analysis for the second and third case studies will be presented. As explained in the opening of the chapter, the first case study was the result of an empirical approach to plate structures from which the systematic method adopted for the construction of the other prototypes was developed. For this reason, a complete Finite Element analysis was performed only on the latter two case studies. Nonetheless, the simulation results of these two test cases contain all the fundamental aspects needed to evaluate the structural performance of arbitrary geometries constructed with the form conversion approach, object of this research.

5.5.1 Effects of prestressing

In this section the effect of prestress on the load-bearing behaviour of bending-active structures derived through the form conversion process is studied. To do so we concentrate on a hemispherical shell structure which represents the base test case for the analysis. The half sphere is compared to the form conversion counterpart derived from a triangular base mesh as well as a quad based mesh dual. As we are interested in assessing the influence of prestress over the mechanical behaviour of the shells, the structural systems must be chosen as similar as possible to be able to extrapolate comparable results. The spheres are chosen as single layered shells made of an ideal isotropic material with a Young's modulus of 15000 N/mm². A value for the shear modulus was omitted to focus exclusively on the bending action and avoid parasitic stress arising from transversal secondary strain effects.

To compare the continuous hemisphere with the form conversion geometries, a full form-finding of the shells had to be performed. By doing so, the bent hemispheres are the outcome of the form-finding process and possess all the forces and stress information that might have an influence over the structural behaviour of the shells. In the first place the discrete shell geometry is completely unrolled on the plane. As the initial generated surface from the form conversion process is everywhere either flat or at most single curved, we know that the unrolling of the surface can occur without stretching or shrinking. In other terms, the planar, unrolled surface is completely isometric to the wrapped shape.

The bending process of the hemispheres is shown in Fig. 5.25. The unrolled pattern is completely bent into shape by using successive form-finding steps based on the ultra-elastic cable approach [Lienhard et al. 2014]. A series of elastic cables are attached to the nodes of the mesh that need to be connected together and gradually shrinked until the length of each cable element vanishes. The form-finding process of the spheres needed to be broken down into several steps, as attempting to perform the simulation at once by first attaching and then shrinking all the cables through prestress inevitably led to high instabilities in the system. Successive series of ultra-elastic cables pull the flat elements together until the whole structural system is restored as seen in Fig. 5.25. The fact that the full bending process of the hemisphere could be fully simulated, is also a strong guarantee that the shape deriving from the form conversion process is geometrically compliant with the limits of the material.

For each set of ultra-elastic cables, after the shrinking process is completed nodes that were distant from one another

FIG. 5.25

Wrapping process of the form conversion hemisphere
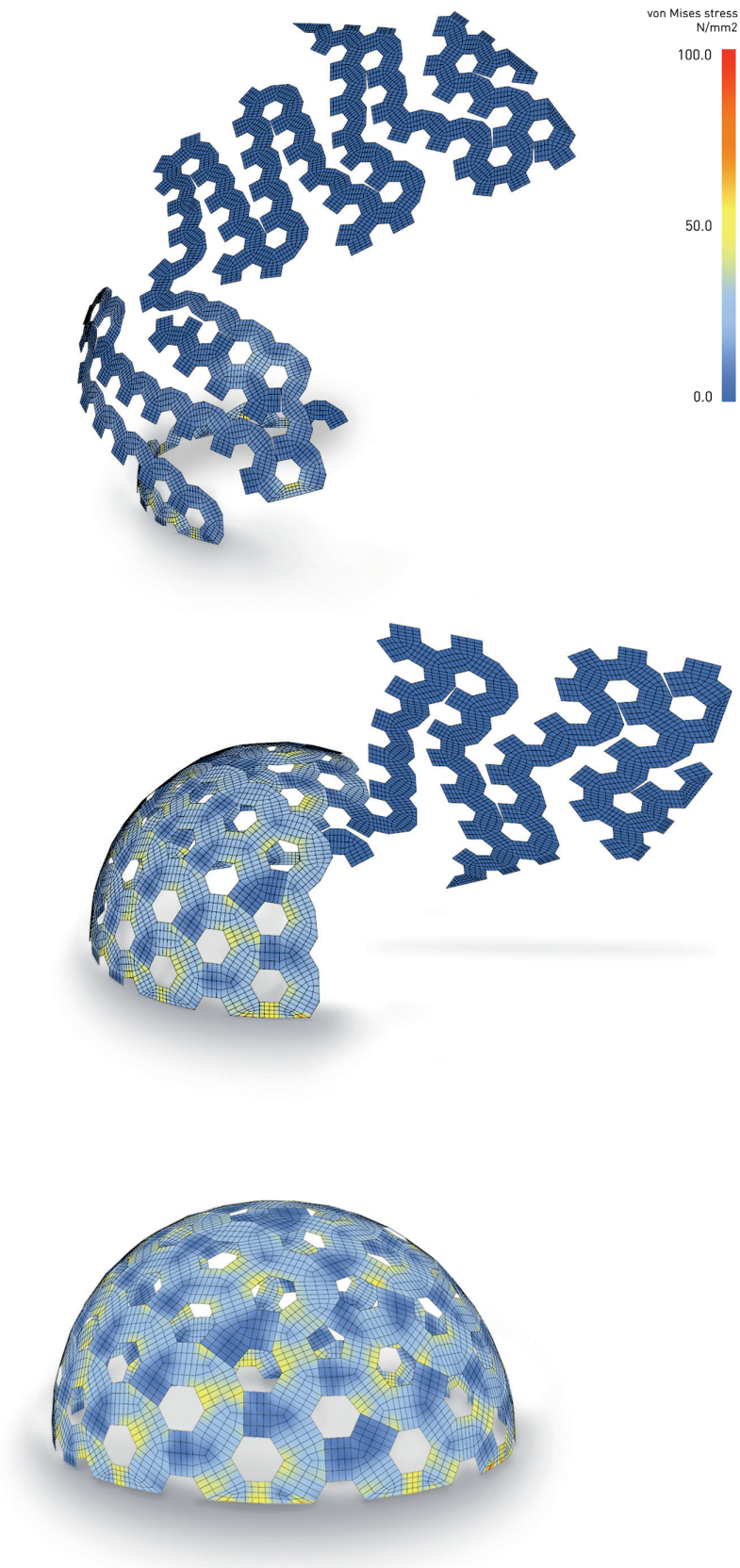
in the starting mesh are now coincident. To restore continuity between the nodes of the mesh, these are joined together using the stiff coupling definition of SOFiSTiK which couples translations and rotations in the three coordinate directions. The SOFiSTiK code line reads: *NODE no 1 fix kf nr1 2*. The previous snippet is interpreted as coupling the translations and rotations *(fix kf)* of node number 1 to the translations and rotations of node number 2. The ultra-elastic shrinking cables method restores the C^0 continuity of the mesh, meaning that continuity is guaranteed only in terms of position. The tangent between now coincident elements is not smooth, so that in most cases a kink develops along the contact line. This could be easily solved by adding a rotation of the nodes to restore the continuity of the tangent, but the computational effort was not deemed necessary for the evaluation of the global result. From Fig. 5.25 it can be seen how the stress level in the quad elements are very low. Here the colour gradient shows the von Mises stress averaged over each element. Almost everywhere the mesh is unstrained (central areas) or axially bent (bridging elements), meaning that the stress derives exclusively from bending. Only in few, localised zones a rise in stress can be seen. As expected, these coincide with the intersection areas between multiple elements and at the sharp corner transitions between branches spanning different directions. Despite of these localised stress concentrations, the bending stresses are generally way below the maximum acceptable levels of the material.

The bent hemispheres are analysed in two different flavours: once in their bent configuration, meaning that the prestress in the plate elements arising from the form-finding process is taken into consideration. The second analysis is performed on the dead geometry. This means that the geometry on which the simulation is performed is the same as the one deriving from the form-finding, but the stress state is completely disregarded. The base geometry is stress free in this case. In this way the effect of the prestress on the stiffness and the mechanical behaviour of the shell can be better recognised.

Each case is analysed by progressively applying a point load in the negative z direction at the top of the hemisphere (Fig. 5.26). The point load has an intensity of 0.1 kN, and at each successive iteration the load is increased by a factor λ. By comparing the load factor λ with the deflection in z direction measured in mm, we obtain the load-deflection graphs as shown in Fig. 5.27. For the form conversion hemispheres, the continuous lines of the graph represent the bent geometries, whilst the dashed lines are for the dead geometries. The continuous red line is representative of the full hemisphere.
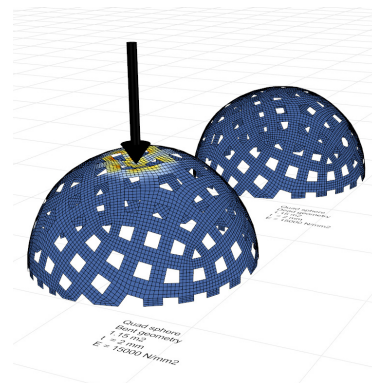
Point load applied to the form conversion hemispheres

Load factor λ [-]

Displacement Uz [mm]
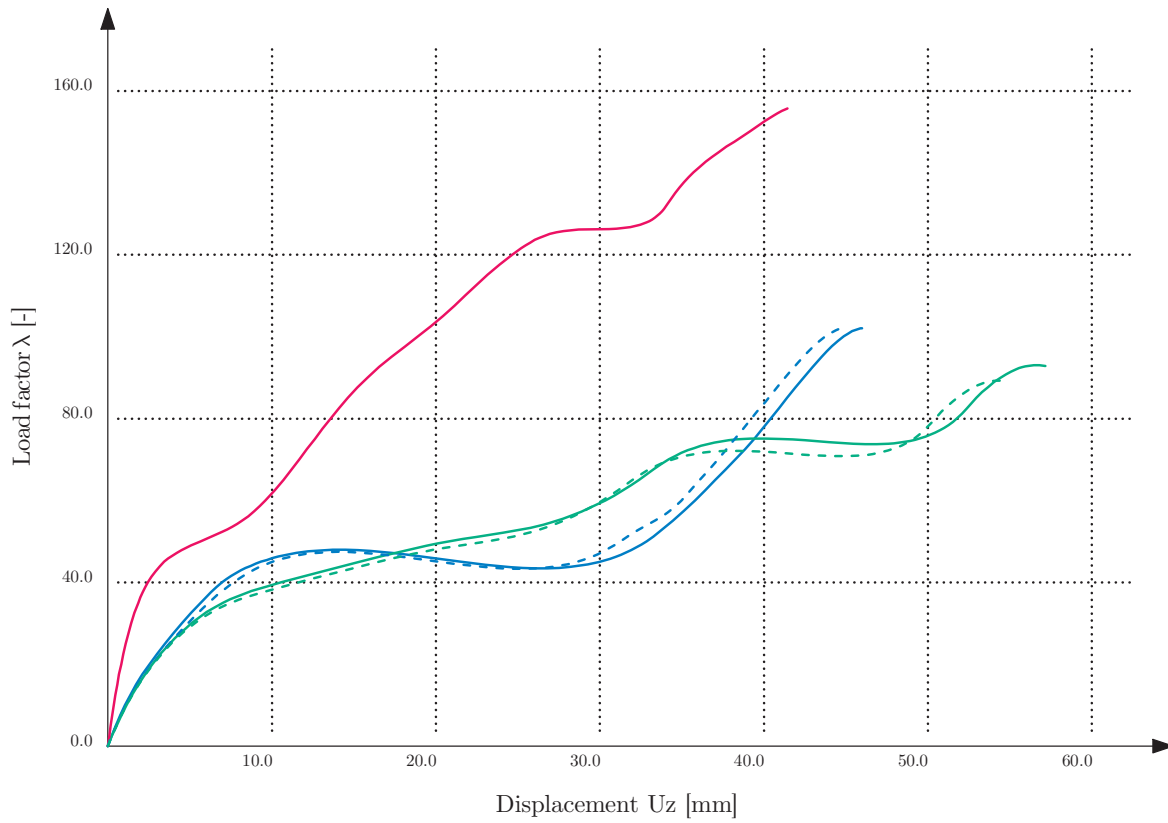
Full sphere
1.51 m2
t = 2 mm
E = 15000 N/mm2

Quad sphere
Bent geometry
1.15 m2
t = 2 mm
E = 15000 N/mm2

Quad sphere
Dead geometry
1.15 m2
t = 2 mm
E = 15000 N/mm2
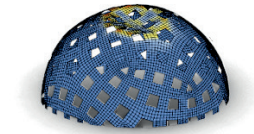
Tri sphere
Bent geometry
1.15 m2
t = 2 mm
E = 15000 N/mm2
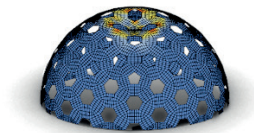
Tri sphere
Dead geometry
1.16 m2
t = 2 mm
E = 15000 N/mm2

FIG. 5.27

Load-deflection curves for the concentrated point load applied on the prototypical hemispheres

92
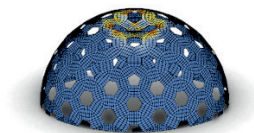
	full	quad bent	quad dead	tri bent	tri dead
diameter	1.0 m	1.0 m	1.0 m	1.0 m	1.0 m
area	1.51 m²	1.15 m²	1.15 m²	1.15 m²	1.15 m²
material	15000 N/mm²	15000 N/mm²	15000 N/mm²	15000 N/mm²	15000 N/mm²
thickness	2.0 mm	2.0 mm	2.0 mm	2.0 mm	2.0 mm
λ/U_z linear	43/2.9 mm	32/6.0 mm	31/7.2 mm	42/7.8 mm	40/7.7 mm
λ/U_z max	156/41.5 mm	93/57.2 mm	89/55.0 mm	102/46.0 mm	102/45.0 mm

Focusing on the results, it can be seen that all test cases initially behave pretty much linearly. The starting branches of each graph are consistent with the hypothesis made so far: a reduction of material implies a proportional reduction of stiffness. As expected, the full hemisphere is stiffer than the form conversion counterparts, as more material is involved in the transfer of forces. It is interesting to notice that the triangular version and the quad version also behave very similar to each other, as their respective load-deflection curves almost perfectly overlap. This suggests a minor influence of the type of pattern on the mechanical behaviour of the shells. What is rather more worthy noticing, is that the difference between the bent geometries and the dead geometries is minimal. The curves in the graph only show a slight deviation between the two variations, which means that the prestressing effect emerging from the form-finding does not seem to have a major influence on the load-bearing behaviour of the discontinuous shells (Fig. 5.28). Furthermore, a beneficial effect deriving from the prestressing would always be dependent on the direction of loading. A material strip bent in one direction will behave radically different whether loaded from the top or the bottom, as the stress distribution deriving from bending will be working against the deformation in the first case, but will be adding stress in the latter. It is therefore not possible to conclude in advance whether the prestressing effect of bending does have a beneficial or detrimental effect on a global scale. Moreover, as already seen in the previous chapters, materials that are suitable for bending-active structures also tend to be extremely susceptible to creeping effects, which overtime tend to nullify the effect of prestressing as it is lost during the relaxation process. In the light of these arguments, it is therefore safe to disregard effects deriving from the prestressing of the plates.

FIG. 5.28

Summary of system values and results
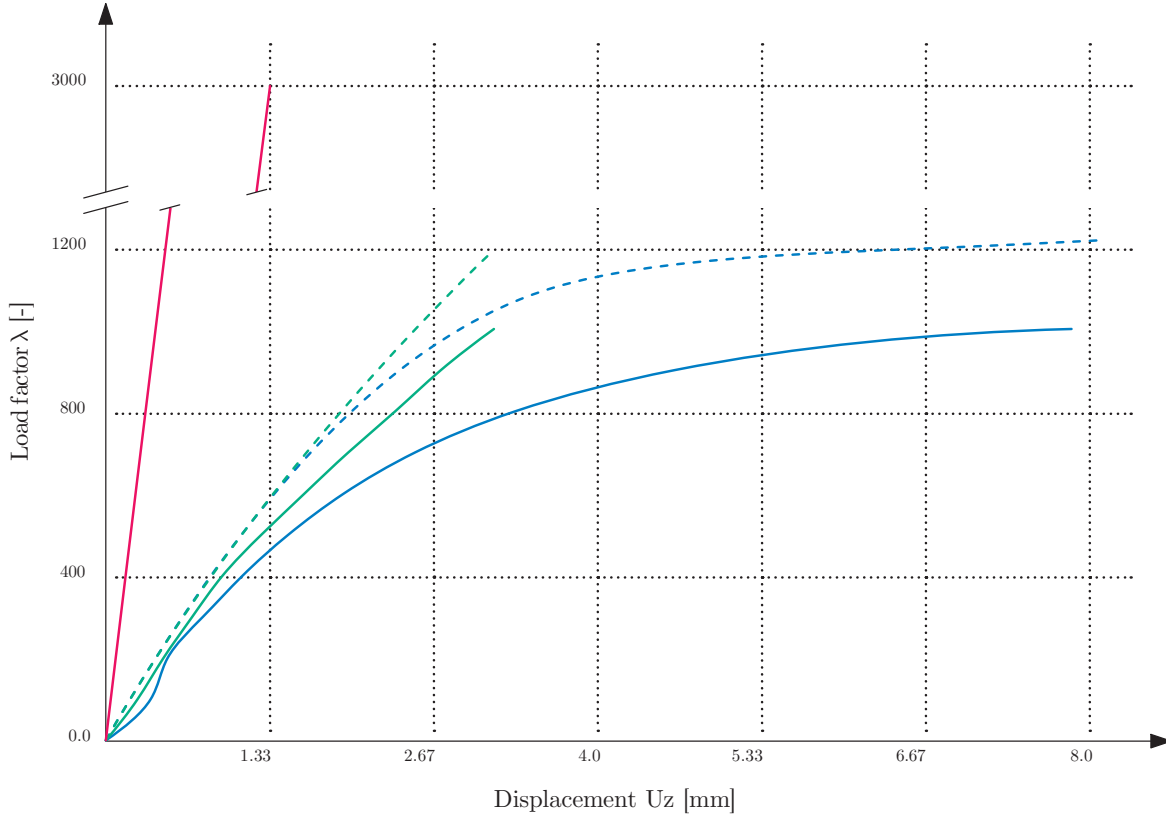
Load-deflection curves for the self-weight load applied on the proto-typical hemispheres

This is also confirmed in the following graph (Fig. 5.29), where the five test cases are also analysed under self-weight. The additional self-weight study is meant to highlight aspects otherwise lost in the previous point load study, as under concentrated loads shells tend to be more susceptible to local imperfections. The x-axis of the diagram shows the maximum vertical displacement of the shell. In this case the bent spheres behave worse than their dead counterparts showing a less stiff response. Besides, failure generally occurs at a lower load factor. Comparing Fig. 5.27 with Fig. 5.29 it is therefore not possible to decide in absolute terms whether the prestressing effect will be beneficial or not to the global behaviour of the shell.

From Fig. 5.29 it can be noted that the full sphere is considerably stiffer than the form conversion spheres. On the other hand, failure will occur rather suddenly due to local buckling in the continuous shell, as opposed to a larger plastic deformation zone which characterises the discontinuous cases. It is also interesting to notice the difference between the triangular pattern and the quadrangular pattern. The quad sphere shows a noticeably stiffer response curve. A possible explanation may lie in the geometry of the voids. By better approximating a triangular field, the quad pattern introduces increased in-plane stiffness, just like a triangulated gridshell is considerably stiffer than one with square fields.

94

Having established the minimal influence that pre-stress has on the structure, we now focus on the analysis of the continuation of the load-deflection curves beyond the initial linear portion for the point load test cases. Beyond the linear part, the form conversion shells show a radical departure from the behaviour of the full sphere. Besides minor differences, both triangular and quad shells display an extended non-linear structural response. It can be noticed how the shells locally bulge inwards entering a post-critical phase dominated by the snap-buckling of the spheres' cap. The graph shows that the cap of the triangular shell locally buckles at a lower load factor, whilst the quad shell withstands a larger load intensity, despite becoming softer, until the cap finally snap-buckles (the horizontal portion of the diagram). Scaled at the right proportions, the curves still resemble the behaviour of the full sphere, although the critical states are reached at a lower load. This effect can be explained by looking at a small portion of the form conversion hemispheres. Locally, the shells are made of developable surfaces connected together. Despite the topological and geometric arrangement of the elements lock undesirable deformations that would occur if these were free from the constraining neighbourhood, a certain degree of flexibility still allows for inextensional deformations of the individual elements to happen. This would explain why the shells generated through the form conversion method display a softer behaviour and are more prone to localised buckling. On the other hand, it must be highlighted that these effects appear at a very late stage and at a high loading factor for the structure. For real life structures at an architectural scale, the post-buckling effects would definitely not be acceptable as the structure would long have failed its purpose.

From the point load test cases we have seen that the effects deriving from prestress have a minimal influence on the load-bearing behaviour and the mechanical response of form conversion bending-active plate structures. This observation provides a useful argument for the simulation workflow, as it relieves the analyst from the bulk of integrating the whole form-finding at an early stage of design. Nonetheless, to capture every detail that might be relevant to understand the structural behaviour, it may still be necessary to perform a fully-fledged form-finding and analysis. This is also confirmed in the analysis of the self-weight test cases, where the effects of prestressing are undoubtedly more evident. Although the analysed prototypes have shown a weak post-critical behaviour, within certain load limits the structures perform well as expected. For these reasons, the advantages in terms of fabrication and assembly might overwhelm the relative reduction of structural performance of bending-active plates.

5.5.2 Influence of geometry and topology

The bending patterns for the form conversion can assume infinite variations in terms of number and shape of the elements. In this section the influence of the principal geometrical and topological parameters that define each individual pattern is studied. Taking as test case the prototypical hemisphere seen in the previous section, we focus on two main parameters and their combination:

1. The surface subdivision, i.e. the total number of elements that make up the pattern.
2. The void to material ratio, i.e. the average ratio between the total area of the voids and the total area of material.

For this study, the surface subdivision makes use of two well-known subdivision schemes, namely the Catmull-Clark for the quad pattern and the Loop scheme for the triangular pattern. Each subdivision step doubles the amount of elements for each pattern leaving the global and local shape unaltered. Three levels of subdivision are taken into account. For each subdivision step the area of the patterned hemisphere remains almost constant, therefore introducing only a change in topology. The rows of the hemispheres' table in Fig. 5.30 and Fig. 5.31 show surfaces with the same value of subdivision.

The void to material ratio provides a relevant metric to estimate the total amount of material against the area of the voids in the structural system. This ratio can vary consistently depending on the amount of offset adopted during the conversion process from the mesh base surface. In Fig. 5.30 and Fig. 5.31, the columns of the table refers to hemispheres with constant void to material ratio. The ratios considered are 0.6 (void area < material area), 1.0 (void area = material area) and 1.4 (void area > material area).

Combining all the parameter variations we achieve a total of nine combinations that provide a precise overview on the influence of geometry and topology on the load-bearing behaviour of form conversion bending-active plate structures. The case studies are analysed by placing a point load at the tip of the surface and observing the vertical deflection of the structure. The dimensions of the hemispheres are the same as for the stiffness studies of the previous section, i.e. 1 meter diameter, 2 mm cross-sectional thickness, isotropic material with Young's modulus 15000 N/mm² and vanishing Poisson's ratio. The point load on the surfaces is 0.1 kN in negative z direction, therefore pointing downwards. The load is chosen

96

Quad sphere
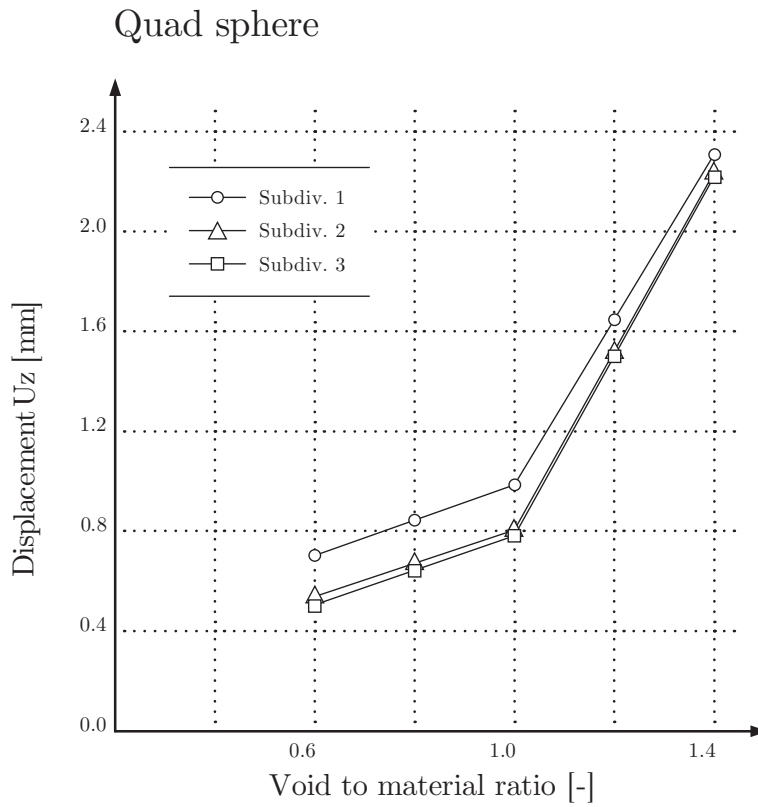
FIG. 5.30

Influence of geometry and topology on the load bearing behaviour of the quad pattern sphere

Subdivision 1
Void/Material = 0.6

Subdivision 1
Void/Material = 1.0

Subdivision 1
Void/Material = 1.4
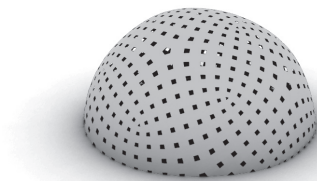
Subdivision 2
Void/Material = 0.6
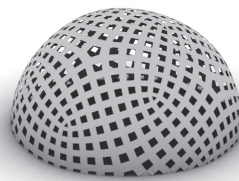
Subdivision 2
Void/Material = 1.0
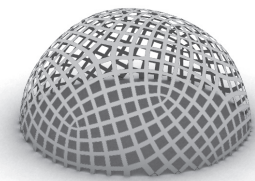
Subdivision 2
Void/Material = 1.4
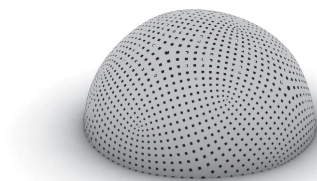
Subdivision 3
Void/Material = 0.6

Subdivision 3
Void/Material = 1.0
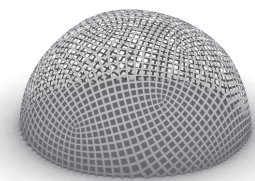
Subdivision 3
Void/Material = 1.4

small enough to avoid entering the nonlinear area of structural response. The analysis is run for both the quad pattern and the triangular pattern.

The diagrams show the influence that geometrical and topological changes of the pattern have on the stiffness of the shell. Each curve represents different levels of subdivision of the form conversion pattern. It can be seen that increasing the amount of elements, i.e. adding a subdivision iteration, but keeping the surface area constant has a minor effect on the amount of total deflection. Between subdivision 1 and subdivision 2 the differences between the two curves are hardly perceptible. In fact, for the triangular pattern (Fig. 5.31) the two curves are almost coincident, whilst for the quad pattern they lie very near to each other. A slightly larger deviation happens with subdivision 3, as the top curve in both diagrams deviates more considerably with respect to the first two curves. This means that the topological arrangement of the elements does not play a fundamental role in the structural performance of the form conversion shell. Moreover, between the quad pattern and the triangular pattern, major differences in stiffness are not apparent. This observation further supports the claim that the topology of the pattern plays a minor role in the influence of the structural behaviour.

As perhaps intuitively expected, the void to material ratio has a far larger influence than the topological variations of the pattern. The graphs in Fig. 5.30 and Fig. 5.31 show the dramatic increase in vertical deflection that the shells experience when raising the ratio. The loss in stiffness becomes absolutely evident for the 1.4 void to material ratio (we remind that a ratio of 1.4 means more voids surface than material area). Between 0.6 and 1.0 the deflection curve grows moderately, with an increase of deflection of roughly 40% for a decrease in material of 60%. The situation is radically different between 1.0 and 1.4, where a further 40% reduction of material in the shell leads to an overwhelming 130% increase of vertical deflection. Besides minor differences between the quad and triangular surface, this trend is almost the same for both patterns as can be seen in the graphs. Looking at the table of models, it is clear how the void to material ratio must strongly affect the structural action in the shell. By gradually dissolving the continuous areas of the surface, this slowly loses its shell-like qualities and starts looking more similar to a grid shell. Obviously, this translates directly into a grid shell transfer of forces in the members as opposed to a continuous shell action. To be able to work as a grid shell, the pattern would require a much thicker cross-section, as the reduced 2 mm are too thin to guarantee enough structural capacity. Moreover, for the 1.6 ratio variation of the shell pattern, the single elements would be way

Tri sphere
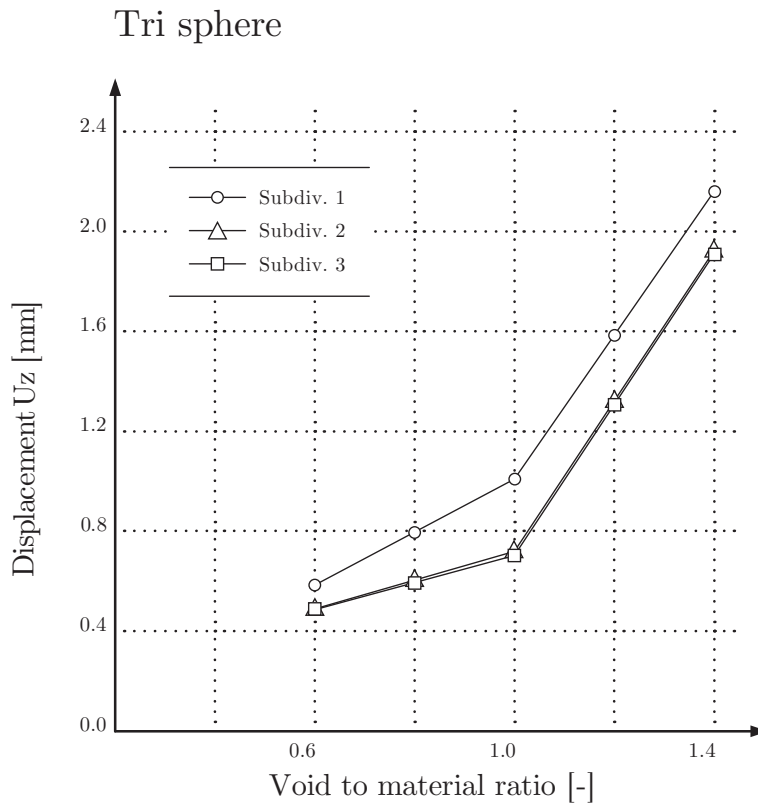
FIG. 5.31

Influence of geometry and topology on the load bearing behaviour of the triangular pattern sphere

Subdivision 1
Void/Material = 0.6
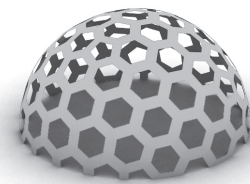
Subdivision 1
Void/Material = 1.0

Subdivision 1
Void/Material = 1.4

Subdivision 2
Void/Material = 0.6

Subdivision 2
Void/Material = 1.0

Subdivision 2
Void/Material = 1.4

Subdivision 3
Void/Material = 0.6

Subdivision 3
Void/Material = 1.0

Subdivision 3
Void/Material = 1.4

99
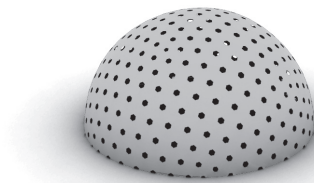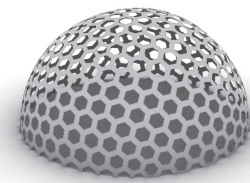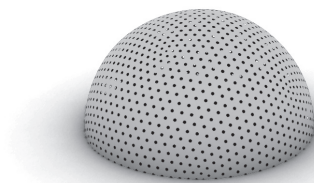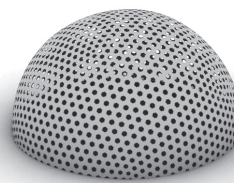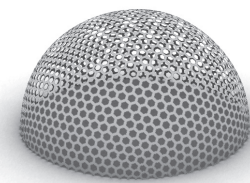
too slender to be able to withstand any buckling instabilities that would occur under the slightest load. For the more continuous versions with 0.6 and 1.0 ratio, the voids are too small to consistently affect the load-bearing behaviour of the shell, as the neighbouring elements are activated way before individual localised buckling can occur. From both graphs it seems as an acceptable balance between void and material ratio lies approximately around 1.0 and below. Beyond this limit the surface loses its structural qualities as continuous shell and starts behaving like a gridshell, for which the cross-section would not be sufficient to guarantee enough structural safety.

As an alternative measure of stiffness, the first eigenfrequency of the individual hemispeheres is analysed. The eigenfrequency can be considered as an indicative parameter of the stiffness of a structure. In [Lienhard 2014] this concept is presented and used to study the prestressing effects on the geometrical stiffness of bending-active structures. We employ the same idea to evaluate the change in structural performance depending on variations of the form conversion pattern. Only the first eigenfrequency of the first eigenmode is presented, as it is the most representative to evaluate the properties that we are focussing on. The results are reported in Fig. 5.32 for the quad pattern and Fig. 5.33 for the triangular pattern. In these diagrams the eigenfrequency is shown ascending, therefore the curves will have a negative slope as opposed to the graphs on the displacement. A higher frequency is associated to a higher stiffness, just like a guitar string with higher pretension will produce a higher pitch, i.e. a higher frequency tone. The eigenfrequency graphs show a similar evolution trend as the deformation graphs. The frequency difference between subdivision 2 and subdivision 3 are relatively minor, whilst a higher discrepancy in the results can be seen for subdivision 3. The more evident differences between the two sets of diagrams are noticeable in the shapes of the curves though. The curves in Fig. 5.32 and Fig. 5.33 show an almost linear progression, whilst the slope of the deformation curves in Fig. 5.30 and Fig. 5.31 considerably increase in the last branch. This suggests a directly proportional correlation between the void to material ratio and the stiffness of the structure, partially contradicting the results seen in the previous graphs. As the type of information employed for the diagrams have different physical interpretations, it cannot be concluded in absolute terms which analysis is more representative for the assessment of the structural behaviour of the form conversion approach. In general, it can still be argued that the major influence derives from the total void area in the surface, meaning how much the form conversion pattern deviates from its continuous base surface.
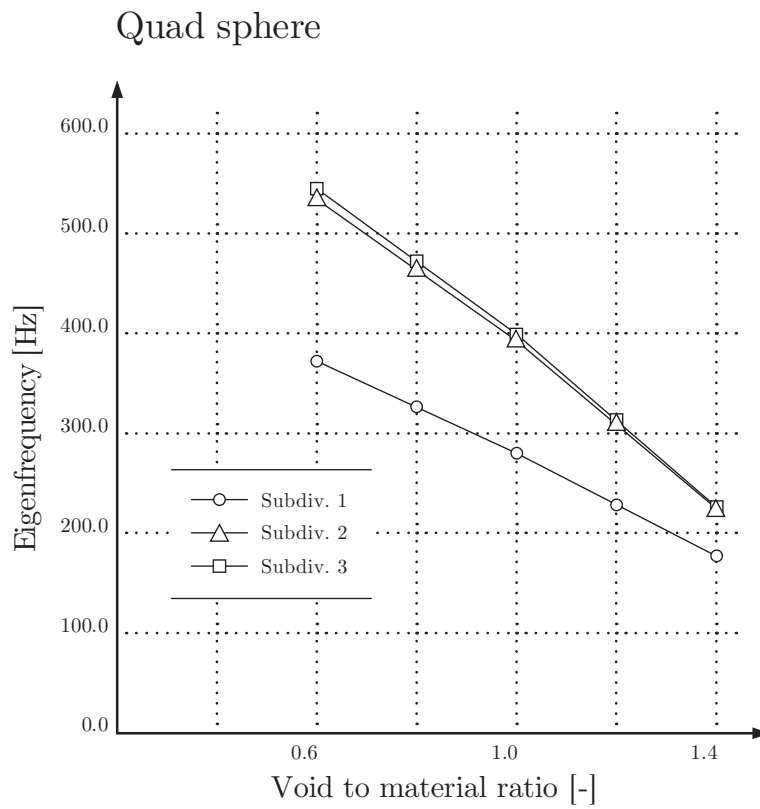
Quad sphere

Tri sphere
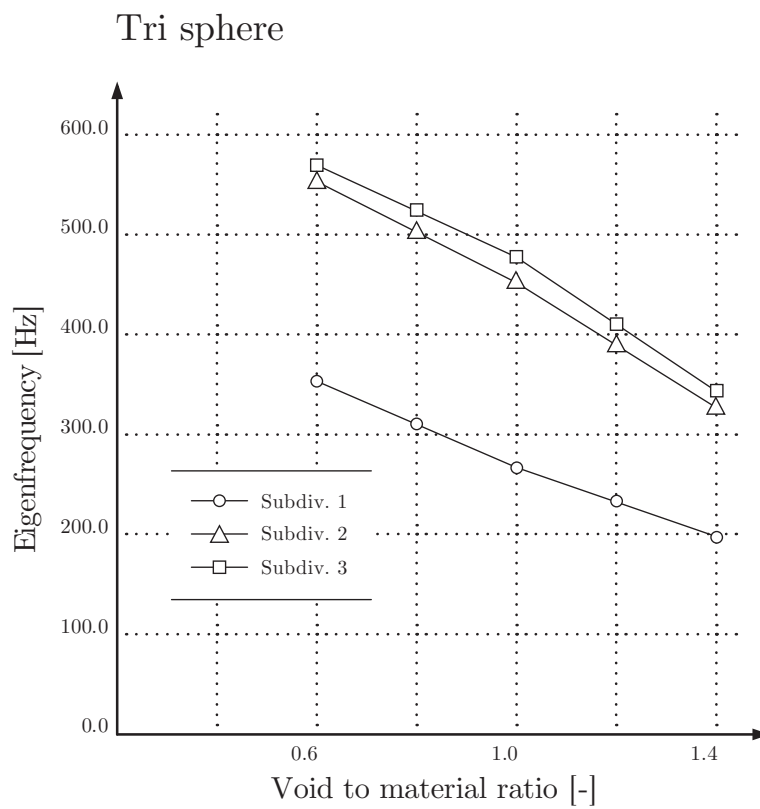
FIG. 5.34

Hex-dominant mesh version of the base sphere and the associated form conversion geometry

So far only two patterns were analysed, each deriving either from a triangular base mesh or a quad base mesh. From the case studies in Fig. 5.30 and Fig. 5.31 it is intuitively obvious that the void topology is nothing else but the geometric dual of the base mesh. Therefore the triangular mesh generates a series of hexagonal voids whilst the quad mesh generates square voids, as the dual of a square tiling is still composed by squares. The gridshell analogy discussed previously prompts the question about the efficiency of the patterns, as topologies departing from the canonical triangulated grid notoriously perform worse due to lower in-plane stiffness. Fig. 5.34 shows the application of the form-conversion approach to a hex-dominant hemispehere. From the conversion geometry it is clear that in this case the voids will be everywhere triangular, being the triangle the dual shape of the hexagon. By increasing the void to material ratio as seen in Fig. 5.34c it is now obvious how the plate structure tends to resemble a fully triangulated gridshell. Assuming that the connection between plates is not everywhere optimal, therefore allowing some degree of rotation between the elements, a hex-dominant topology might generally be preferable due to the locking of potential kinematic modes of the structure. Although not analysed in greater detail, hex-dominant topologies could greatly simplify the connecting detail, allowing for increased in-plane stiffness at the minimal cost of preliminary geometry processing of the base surface.

5.5.3 Structural behaviour of case studies

In the final section of this chapter the structural analysis of the built case studies are discussed. As previously mentioned, the results presented refer to the two latter prototypes, the Berkeley Weave and Bend9 pavilions, as these are the most representative of the developed form conversion approach. The diagrams show the maximum vertical nodal deflection under dead load scaled by a multiplication factor λ and the vertical deflection of a node of the structure with a concentrated point load also scaled by λ. The case studies are analysed in the dead and actively bent configuration to highlight the differences between the two states.

The Berkeley Weave installation is analysed by increasing the dead load up to a factor λ of 6.0 (Fig. 5.35). Beyond this load threshold instability effects occur. The curves in the diagram approximately show a linear response for the dead load cases. The maximum deflection reaches almost 60 mm. As seen for the stiffness studies on the prototypical hemispheres, the difference between dead and bent cases are minimal. Similarly, for the concentrated point load the displacement discrepancies between the bent and dead geometries are

Berkeley Weave – Self-weight
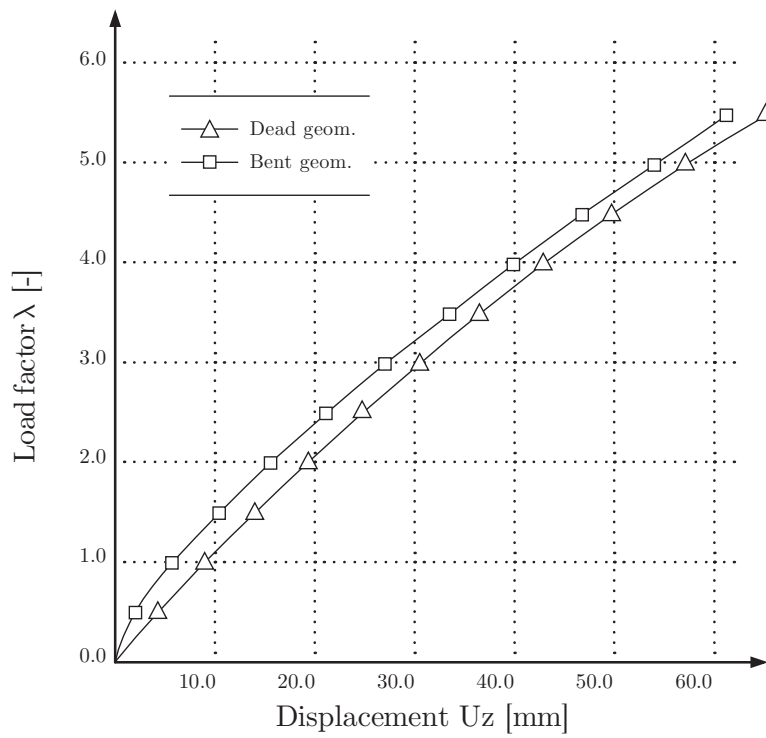
Berkeley Weave – Point load
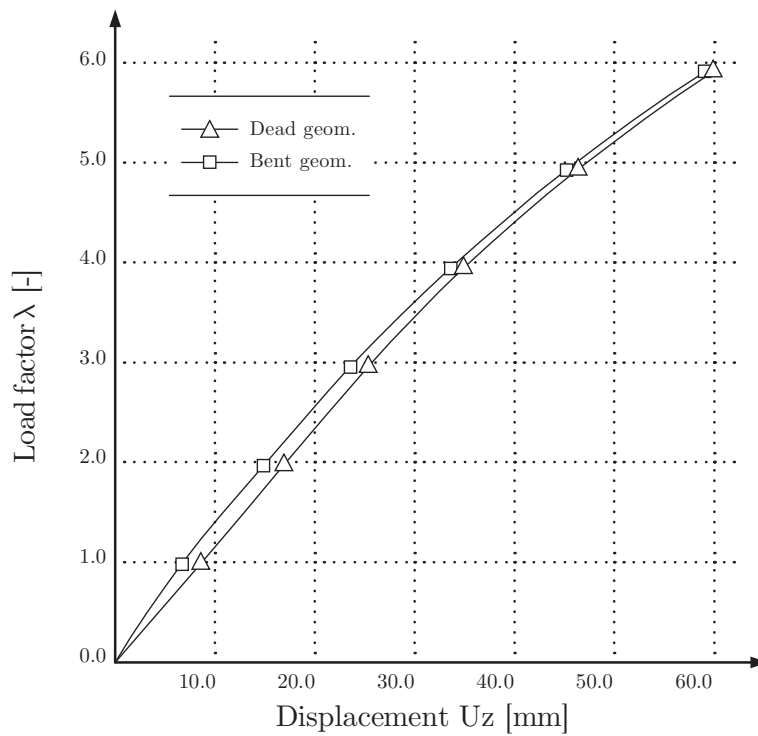
103

negligible. Here the point load is chosen equal to 0.1 kN and increased tenfold up to a maximum of 1.0 kN (Fig. 5.36). The load is applied at the centre of the surface. It is worth noticing that, despite showing a linear behaviour, the maximum vertical displacement reaches almost 300 mm. This is mainly due to the fact that the Berkeley Weave pavilion is made out of a single layer surface. The bending stiffness of the shell depends only on the thickness of the layer of plywood strips that compose the structure.

Fig. 5.37 shows the behaviour of the Bend9 pavilion under dead load. The development of the graph is still almost linear for the dead case, and slightly stiffer in the case of the bent configuration. The deflection under the maximum factor λ of 5.0 is 37 mm. Due to the larger span and considerable weight difference compared to the Berkeley Weave installation, it is comprehensible that the maximum deflection under self-weight is similar between the two prototypes. For the analysis under point load the situation is radically different. The point load is also chosen equal to 0.1 kN and increased tenfold up to a maximum of 1.0 kN in the negative z direction (Fig. 5.38). The vertical displacement of the node on which the point load is applied reaches a maximum value of 50 mm, six times less than the previous case study. The distinct increase in stiffness is mainly due to the double layer structure of the pavilion. Depending of the third power of the lever arm of the top and bottom layers, the bending stiffness is way higher in this case. For this reason, the coupling of multiple layers seems to be the best strategy to compensate the low stiffness due to the reduction of cross-section that is necessary to perform the bending of the individual elements.

From all the analysed case studies it emerges that the influence of prestressing effects in the bending active elements is minimal. These results are consistent with the studies run on the bending hemisphere seen in the previous sections of this chapter. For the single layered Berkeley Weave installation, the influence is slightly more evident, as the Bend9 pavilion takes predominantly advantage of the double layer configuration rather than the embedded inner stress state. Moreover, beneficial effects of prestress are predominantly directional, as reverting the load direction on the structure may cancel any positive result. Prestressing makes sense for structures where a primary load case dominates over the others, therefore guaranteeing a consistent loading state throughout the life of the construction. Concrete structures are the most prominent example, as in most cases self-weight overrules all other possible loading scenarios. For lightweight constructions such as bending-active structures this argument cannot be safely applied as these structures are way more sensible to the

Bend9 – Self-weight
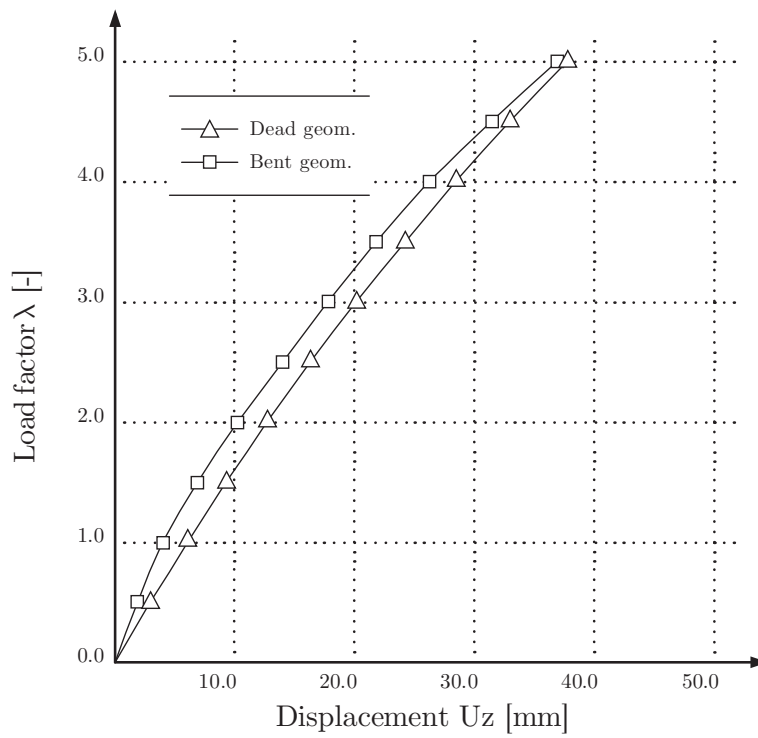
Load-deflection analysis of the
Bend9 pavilion under self-weight

Bend9 – Point load
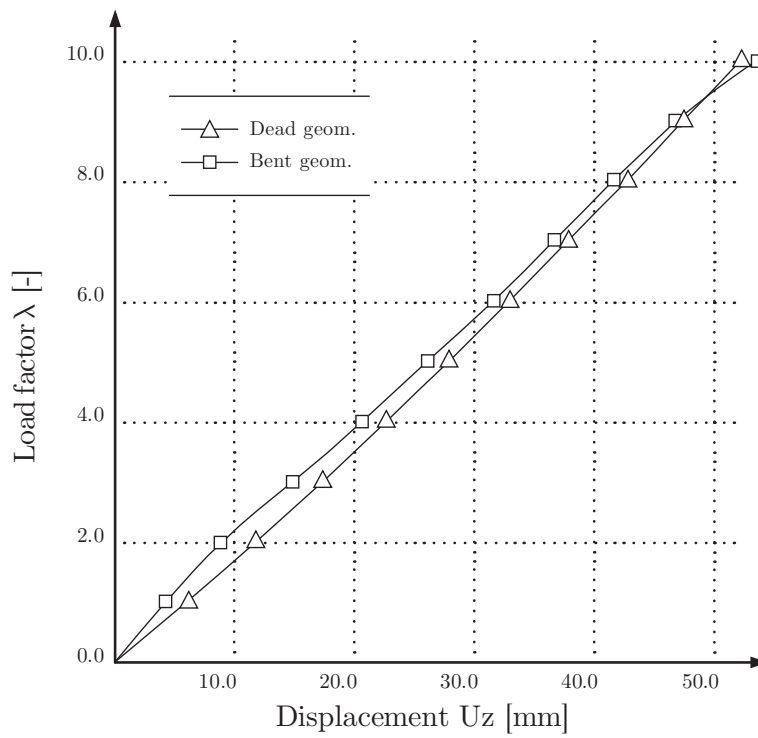
Load-deflection analysis of the
Bend9 pavilion under point load

direction of loading. The graphs of the case studies only show slight deviations between the dead geometry curve and the bent curve. Another potential reason for this behaviour may lie in the fact that the form conversion prototypes studied in this work do not have a dominant bending direction, but due do the tight curvature changes in the master geometry tend to bend and twist in different ways. For instance, this means that for a vertical loading the bending stresses of certain elements will work favourably, and neighbouring elements which bend in the opposite direction might as well increase the global deformation rather than reducing it. In the case of freeform surfaces it might become almost impossible to assess beneficial effects of bending due to all the concurrent parameters than have been listed so far.

In this chapter the form conversion approach for bending active plate structures has been presented and studied. The limits of the method lie exclusively in the bending and twisting radii of the individual elements, an aspect than can be addressed in the early stages of design to improve the deformation of the single pieces. It has been shown that bending and torsion mutually coexist, but in this case the total deformation of the elements is drastically reduced due to geometrical stiffening effects by introducing double curvature which prevents the deformation to occur any further. In general though, bending is preferred to torsion. The prototypes presented served as a proof of concept of the applicability of the form conversion approach. Arbitrary double curved surfaces were chosen to show the flexibility of the method and how it performs in the case of tight curvature radii which evolve throughout the development of the base surface. The test cases were analysed along with a series of studies performed on exemplary hemispherical shells. These studies were meant to assess the bendability of the unrolled shells, confirming in the first place that the patterns generated through form conversion indeed produce strips of developable surfaces. The simulations showed that only relying on the geometry of the elements and their topological arrangement, the continuity of the surface is restored. No additional information is therefore required for the construction of form conversion structures. In the closing sections of the chapter, studies on the prestressing effects deriving from the bending process of the plate elements were presented. The prestressing showed to exert a minor influence on the load bearing capacity of the global structures. For this reason, it is safe to analyse such structures in their dead geometrical configuration especially in the stage of preliminary design studies.

6. Embedded approach

The research on bending-active plate structures presented so far highlighted the strong limitations pertaining the deformation field of planar elements. As seen, these aspects have a strong effect on the formal potential of bending-active systems, and alternatives need to be devised in order to overcome such limitations. The geometrical and mechanical models which describe the deformation and the associated stress state clearly manifest the unfeasibility of inducing an appreciable double curvature in the material.

Strategies to induce double curvature can vary in scope and nature. The easiest choice is to employ materials which can locally withstand a great amount of stretching deformation, therefore allowing the material to assume a double curved configuration. This is for instance the case of membrane materials which can undergo large deformations without tearing. On the other hand, membranes do not possess any bending stiffness and need mechanical prestress to be able to withstand external loading. Metals such as steel and aluminium have an extended plastic zone, therefore they can undergo large plastic deformations without breaking. This principal is typically employed in many industries to create custom shaped elements, for instance chassis for the car industry or stamped elements. In this case the deformations are irreversible as the plastically deformed material will maintain the end shape and not spring back into its original undeformed configuration as in the case of elastic deformations. Membrane materials and plastic deformations both fall outside the realm of investigation of this work, the first due to their lack of bending stiffness and in the latter case as we focus on elastic deformation as opposed to plastic.

Ruling out alternative material choices, the other aspect worth investigating is geometry. Paraphrasing Julian Vincent's famous quote, "in nature material is expensive" [Vincent 2002], but geometry is cheap. Following this maxim, the main intuition that guided the investigations of the current chapter is that geometric variations in the arrangement of planar elements might lead to the sought result. This fundamental idea steered the research towards the field of metamaterials, where similar concepts have been developed particularly in the area of composite materials. The next paragraph introduces the topic focusing on the main ideas and concepts, which will be later expanded to the specific applications devised for the scope of the current work.

Metamaterials

- Electromagnetic
- Optical
- Acoustic
- Nanotechnology
- Mechanical
  - Auxetics
  - Cellular structures
  - Functionally graded materials
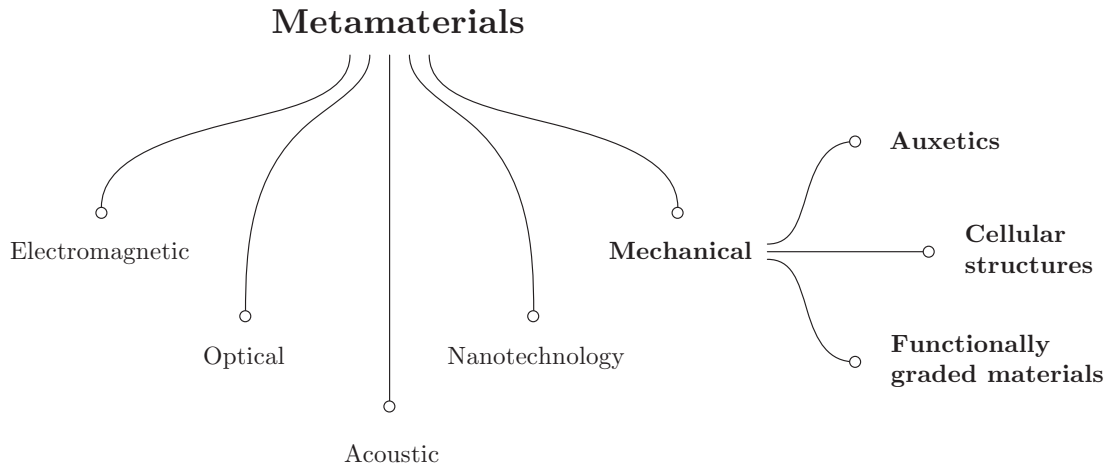
Classification of metamaterial types

6.1 Auxetics and metamaterials: an overview

A metamaterial is a material engineered to have a property that is not found in nature [Kshetrimayum 2004]. Typically, these are materials which have characteristics that can be significantly modified in a controlled fashion by external stimuli. This behaviour is derived by the assembly of multiple elements arranged in a repeating pattern, the scale of which is smaller than the amplitude of the phenomena they influence. Metamaterials don't derive their behaviour directly from the properties of the base materials, but rather from their designed structure. Metamaterials find applications in many different fields, ranging from electric engineering, optics, electromagnetics, nanoscience, aerospace engineering, material science and others (Fig. 6.1). Of the wide subclasses of existing metamaterials, mechanical metamaterials are the ones this research focuses on.

Mechanical metamaterials have a relatively recent history, although their existence had already been postulated over a century ago. Their systematic description is unanimously credited to Professor Rod Lakes from the University of Wisconsin in his seminal 1987 paper titled *Foam structures with a negative Poisson's ratio* [Lakes 1987]. In his paper Lakes describes a new class of materials in the form of a manufactured thermoplastic open cell foam that presented properties which are not encountered in ordinary materials. He specifically focused on the value of Poisson's ratio, demonstrating that a certain cellular pattern arrangement would lead to a material with a negative value. This was revolutionary in its own way, as until then materials with a negative Poisson's ratio had only been postulated but never (or very seldom) actually found in nature nor fabricated.

The class of mechanical metamaterials exhibiting a negative Poisson's ratio have been later dubbed *auxetics*. This term was coined by Professor Ken Evans of the University of Exeter and first appeared in the scientific paper *Molecular Network Design* [Evans et al., 1991]. The term auxetics derives from the Greek αὐξητικός (auxetikos) which literally means "that which tends to increase" and has its root in the word αὔξησις, or *auxesis*, meaning "increase". This definition derives from the peculiar behaviour of auxetic materials, which expand if stretched as opposed to common materials which exhibit a shrinkage of cross-section if under tension. The opposite is true if the material undergoes compression, i.e. typical materials would bulge, whether an auxetic material will become narrower in the direction perpendicular to the compressive axis. This behaviour is perfectly captured by the quantity known as Poisson's ratio ν, which is an elastic constant defined as the ratio of the lateral contraction strain with respect to the longitudinal tensile strain for a material under tension in the longitudinal direction [Evans et al., 2000]. In the case of typical materials, this is a positive quantity. For auxetic materials it is negative.

Auxetics are artificially engineered to display a negative ratio of lateral contraction otherwise unattainable in natural materials. This is achieved through a specific spatial arrangement rather than material composition (Fig. 6.2b). The mechanical behaviour of the structure is therefore directly dependent on the shape, size, topology, geometry and orientation of the single units and their specific arrangement. This shifts the importance played by material to geometry. Auxetic structures derive their macro mechanical properties from the specific arrangement of material and voids, therefore geometry is the main responsible for the way the structure responds mechanically. By varying the geometry of the pattern, the mechanical response changes accordingly, allowing to achieve a wide range of properties which can be specifically tailored and adapted to the needs of the designer. As it will be described in the following chapter, by inverting the geometry of an auxetic cell we retrieve the classic hexagonal honeycomb pattern. For this reason auxetics are also known as inverted honeycombs. Although not commonly described as a metamaterials, regular honeycomb structures also present traits of typical metamaterials, as their Poisson's ratio is above the typical incompressible limit of 0.5 (Fig. 6.2a). These aspects will be discussed in further detail in the following paragraph. Given the similar conceptual nature of honeycombs and auxetics, we will from now on refer to both types of structures as honeycombs, and will specify terminology where necessary to avoid confusion.
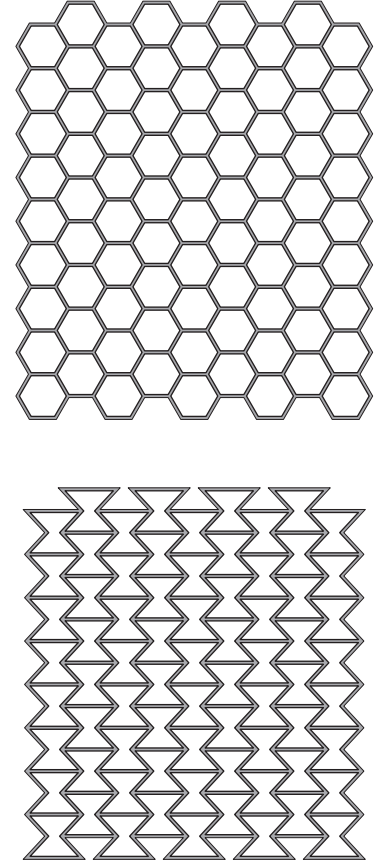
FIG. 6.2

a. Regular honeycomb structure,
b. Auxetic honeycomb structure
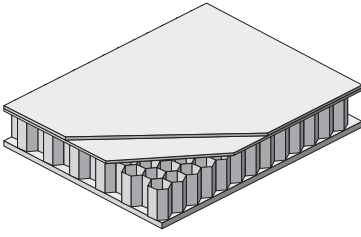
FIG. 6.3

Typical use of honeycombs for composite sandwich panels
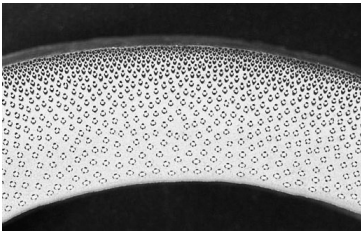
FIG. 6.4

Moso bamboo – cross-sectional surface of culm wall. Densification of the vascular channels is well recognisable

A complete literature review on the topic is utterly impossible due to the humungous amount of existing material. In the present chapter a few key publications will be mentioned, focusing on those mostly relevant for this research. The interested reader is referred to the bibliography of the cited books and articles to have a deeper overview of the work conducted so far in the field.

Lakes' work has given rise to a prolific stream of work, with researchers investigating negative Poisson's ratio structures due to their stiffening geometric effects and enhanced indentation resistance [Gibson et al. 1999, Grima 2012], shear modulus and impact absorption [Ju 2011] and much more. Lightweight cellular honeycombs have been widely used for automotive, marine and aerospace applications (Fig. 6.3) due to their increased properties of resistance, thermal insulation, and energy absorption capabilities [Gibson et al. 1999].

The great flexibility in terms of topology, geometry and material composition of cellular structures provides the designer with a vast range of possible multifunctional characteristics, as well as unusual and counterintuitive deformation properties. Exerting granular control over single, very small portions of the structure leads to the design of *Functionally Graded Materials.* In material science, Functionally Graded Materials are characterised by gradual variations in composition, structure and topology over the volume, therefore resulting in corresponding changes in the properties of the material. In the case of Functionally Graded cellular structures, a gradual variation of the shape, size and wall thickness of the cells over a certain portion of volume characterise the geometry and the mechanical response of the structure. The gradient topology leads to a continuous distribution of curvatures, stiffness and energy absorption capabilities [Hou et al. 2013].

In nature, gradient topologies are commonly found in plant stems to increase bending resistance under high loading. Some examples include the honeycomb-like vascular bundles of the coconut tree (*Cocus nucifera*), the internal microstructure of bamboo (Fig. 6.4) and the radial cellular densification of the *Iriartea gigantea*, which provides higher bending stiffness to a uniform density section [Gibson et al. 2010]. Research on Functionally Graded cellular structures have included, amongst others, investigations on deformation mechanisms under crushing [Ajdari et al. 2011], energy absorption capabilities of functionally graded foams [Cui et al. 2009], reduction of stress intensification for sandwich structures under dynamic loading [Kirugulige et al. 2005]. Recently, research on gradient cellular structures has been focusing on their shape-shifting capabilities. Gradient cellular solids are also known as *polymorphic.* This definition derives from the fact that they can change and vary their shape

and Poisson's ratio values along the principal direction of manufacturing. The gradual Poisson's ratio change, and therefore the continuous variation of curvature as will be seen in the following sections, is indeed one of the main characteristics of gradient cellular structures, and the principal aspect driving this part of research. Work focusing on the deformation properties of polymorphic cellular cores includes Lim [Lim 2002], who proposed a gradient cellular structure with a rotational symmetric array of regular cells by varying the internal cell angle. This core design was applied to a functionally graded beam with Poisson curving qualities. Lira and Scarpa [Lira and Scarpa 2010] devised a method to optimise the transverse shear stiffness of the honeycomb by varying the thickness of the horizontal rib through the panel. Recently, a noteworthy article by Hou et al. [Hou et al. 2013] focused on the bending properties of sandwich structures with auxetic cellular cores. As expressed by the authors in the paper, "to the best of the Author's knowledge, this is the first time a comprehensive analysis on the bending and failure of manmade gradient cellular structures has been performed". Other notable research recently appeared include the work of Pagitz et al. [Pagitz et al 2012, Pagitz and Bold 2013]. In this series of excellent articles the authors focus on compliant pressure-actuated cellular structures and their shape-changing properties inspired by the nastic movement of plants (Fig. 6.5). Although the actuation method is essentially different to the one employed here (pneumatic vs mechanical), it is remarkable to notice how the geometries and topologies of both types of structures are very similar. Morphing structures are rapidly growing in popularity especially in the field of aerospace engineering for the design of shape-changing wings. A recent paper by [Loukaides and Seffen 2015] describes the mechanical properties of regular honeycombs with square cells, drawing a parallel between the behaviour of grid shells and honeycombs. Finally, recent work by Farahi [Farahi 2016] adopted a similar approach as the one presented in this work for the production of morphing garments.

This introduction serves as a brief overview of the vast research field on auxetics, metamaterials, cellular structures, Functionally Graded Materials and shape-shifting structures. It is not intended to be exhaustive, but rather to highlight the main topics and the key ideas most relevant within the context of this work. Despite such a diverse terminology, objectives and methods, many concepts overlap and flow into each other, often presenting more similarities than differences. The topics developed in the upcoming paragraphs draws from all of these concepts and combine together specific aspects into a new and yet unexplored approach. Paraphrasing the previous quotation, to the best of the author's knowledge, this is the first time this topic has been developed in this way.
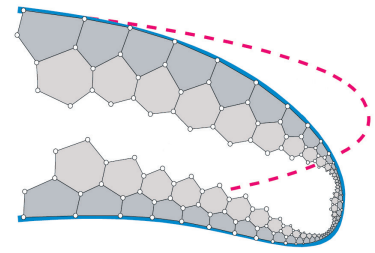
FIG. 6.5

Morphing wing through pressure-actuated cellular structures (from [Pagitz 2012])

Material	Poisson's ratio
Aluminium	0.33
Titanium	0.32
Stainless steel	0.31
Steel	0.288
Wrought iron	0.278
Cast iron	0.27
Glass	0.27
Concrete	0.2
Cork	0.0

FIG. 6.6

Poisson's ratio values of typical construction materials
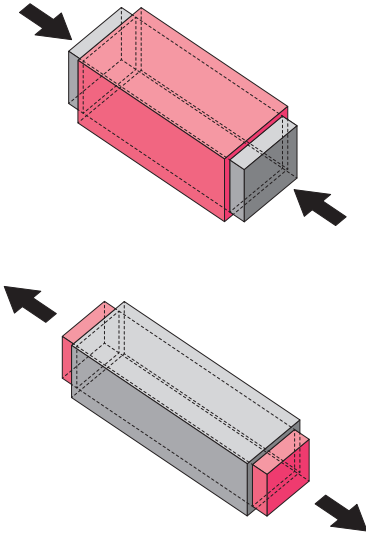
FIG. 6.7

Poisson's effect for conventional materials. a. Under compression the material expands transversally, b. Under tension the material contracts transversally

6.2 Poisson's ratio and its influence on curvature

We first introduce the definition of Poisson's ratio for linear, isotropic materials to focus on the main aspects that derive from it. Poisson's ratio ν is an elastic constant defined as the ratio between the lateral contraction and the elongation in the infinitesimal uniaxial extension of a homogenous isotropic body:

$$\nu = -\frac{\varepsilon_{transversal}}{\varepsilon_{longitudinal}}. \tag{6.1}$$

Tensile deformations are considered positive and compressive deformations are considered negative. The definition of Poisson's ratio contains a minus sign so that normal materials have a positive ratio. It is a pure, dimensionless number as it is the ratio of two quantities which are dimensionless themselves.

The theoretical limit of Poisson's ratio for isotropic materials is $-1 < \nu < 0.5$. This derives from the fundamental assumption that the function of energy density per unit volume for a linear elastic solid ψ must be strictly increasing for all conceivable deformations, i.e. $\psi \geq 0$ [Mott and Roland 2013]. This quantity is a function of the elastic constants and deformation. For an isotropic material the elastic constants (Young's modulus E, Poisson's ratio ν, the shear modulus G and the bulk modulus K) are linearly dependent on each other, only two of the four being linearly independent. By formulating Poisson's ratio in terms of the shear modulus and the bulk modulus we retrieve the following relationships:

$$K(G,\nu) = \frac{2G(1+\nu)}{3(1-2\nu)} > 0,$$
$$G(K,\nu) = \frac{3K(1-2\nu)}{2(1+\nu)} > 0. \tag{6.2}$$

To satisfy both of these constraints, and to ensure that the shear modulus G and the bulk modulus K are bounded, the restriction $-1 < \nu < 0.5$ must be placed on the values of Poisson's ratio.

Virtually all common materials, especially those typically employed in the construction industry, have a positive Poisson's ratio, i.e. they become narrower in cross section when they are stretched (Fig. 6.6). The reason of this behaviour is that most materials resist a change in volume, determined by the bulk modulus K, more than they resist a change in shape, as determined by the shear modulus G. For reasons of simplicity we will first concentrate on positive Poisson's ratio materials, and will later expand the discussion to the other class of materials.
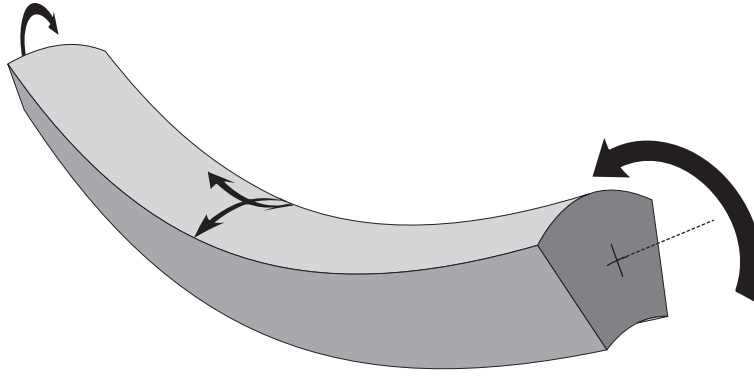
FIG. 6.8

Due to Poisson's effect, when a material is compressed in one direction it will expand in the other two directions perpendicular to the one of compression. How much it will expand in the transversal direction is captured by the value of Poisson's ratio (Fig. 6.7a). On the other hand, if the material is stretched rather than compressed, it will contract in the directions transverse to the direction of stretching (Fig. 6.7b). This can be typically noticed when a rubber band is stretched as it becomes noticeably thinner in the transversal direction. Just like for compression, under tension Poisson's ratio will be the ratio of relative transversal contraction to relative stretching expansion and will have the same value as above. It is indeed interesting to notice that this effect exists for both tension and compression.

As a consequence, bending will directly be influenced by the dual existence of Poisson's effect for stretching and compressive actions. Considering a homogenous beam made of isotropic material undergoing bending, the cross section will present a typical butterfly distribution of the normal stresses. For the beam in Fig. 6.8, the top half of the cross section will be under compression and the bottom half under tension, with the neutral surface running exactly along the centre of mass of the beam. As the top half is subject to compressive forces, it will expand laterally to compensate the change of volume following the described Poisson's effect. The same is true for the bottom half which will shrink laterally because under tension. This differential change of length over the beam's cross section is responsible for inducing curvature in the transversal direction of bending deformation. The effect can be understood better by considering what happens to a thin strip of material under a differential thermal load. In this case, if the bottom expands due to a positive thermal load and the top half shrinks under a negative thermal load, the differential expansion induced on the two halves of the cross section will induce curvature in the strip. This effect is well known in nature, especially in the case of plants which

113

A beam made of isotropic auxetic material will behave in the opposite way of a conventional beam. Under bending the beam will present a slight synclastic curvature as the layers under tension will expand and the ones under compression will shrink
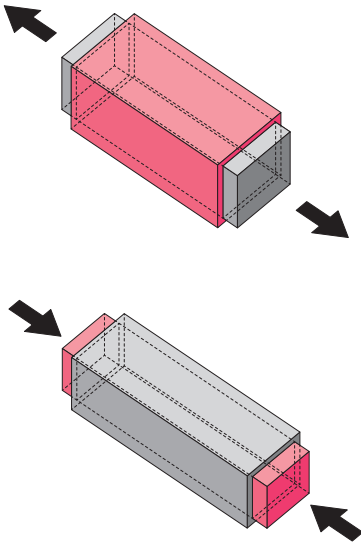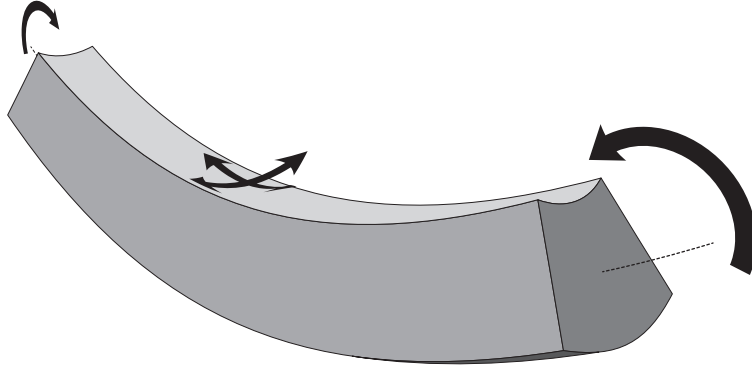
Auxetic materials with negative Poisson's ratio display the opposite effect of conventional materials. a. Under tension the material expands transversally, b. Under compression the material shrinks transversally

employ differential cell expansion and differential growth mechanisms as their primary source of movement [Schleicher et al. 2014]. In summary, Poisson's ratio governs the curvature in a direction perpendicular to the direction of bending. This effect can be easily visualised in the anticlastic curvature that emerges by the bending of a rubber eraser.

6.2.1 Auxetic structures

Common materials have a positive Poisson's ratio. Although materials with negative Poisson's ratio are theoretically prescribed by the relationships seen above, in reality they are extremely rare. In nature only certain rocks and minerals have been found to display auxetic behaviour. As it will be described later, auxetic materials derive their properties from internal mechanisms which are activated upon deformation. Assuming for now that materials with a negative Poisson's ratio exist, their behaviour will be exactly the opposite of conventional materials. Whilst a positive Poisson's ratio material will contract laterally when stretched, an auxetic material will expand its transversal cross section (Fig. 6.10). The opposite is true for a compressive axial force acting on the material, which will have the effect of shrinking the specimen in the perpendicular direction. This behaviour of auxetic materials is exactly complementary to the one displayed by their conventional counterpart.

By inverting the sense of lateral expansion (or shrinking), also has a direct effect on the response to bending. Looking back at the example analysed previously, we now consider a beam made of homogeneous and isotropic material, but this time we assume that the material possesses auxetic behaviour (Fig. 6.9). By applying a bending load, we will still have the top half of the beam under compression and the bottom half under tension. The nature of the material obviously does not play any role in the equilibrium of forces in this case. But we will now have the top half shrinking under compression and the bottom half expanding under tension.

The sense of deformation is exactly mirrored with respect to the neutral surface of the beam. As a consequence of this inversion between expanding and shrinking areas, the hypothetical auxetic beam will present a synclastic curvature, as opposed to the anticlastic curvature of the conventional beam.

This dual behaviour of conventional and auxetic materials provides an interesting hint to overcome the obstacles to shape formation which have been encountered so far. The necessary changes in length required to induce Gaussian curvature in a planar sheet of material could be potentially solved by taking directly advantage of the intrinsic deformation of materials. Hypothetically, being able to vary Poisson's ratio over a certain region of material would allow to achieve a continuous change of curvature in the structure. This is the fundamental principle which guides the idea of functionally graded materials.

Two key aspects still need to be taken into account to have a complete framework for functionally graded bending materials: where to find auxetic materials and how to free Poisson's ratio of conventional materials from the upper limit of 0.5. Amazingly, both issues are solved in a conceptually similar fashion.

Materials with a negative Poisson's ratio are extremely rare in nature. The few existing examples have been object of thorough investigation and research. In the case of the few rocks and minerals which display auxetic behaviour, it has been proven that this effect is due to the peculiar crystalline microstructure, which acts as a mechanism which deploys when stretched. Auxetic materials possess a specific internal structure tightly folded into itself under rest. Following loading, the individual elements unfold and expand as a result of their geometrical nature. This mechanism is at the base of the properties of auxetic materials.

The microstructure of auxetic materials is perfectly replicable on a larger scale. The most common and well known of these structures is the so called *inverted honeycomb* seen in Fig. 6.2b. This name derives from the geometry of the cell, which is a hexagon with two of the six vertices shifted towards the interior giving rise to a non-convex polygon with the typical butterfly shape.

The bee's honeycomb perfectly exemplifies a cellular solid in two dimensions with its regular array of hexagonal cells. By extending this concept, the word 'honeycomb' can be used in a broader sense to describe any array of polygonal cells which are nested together to fill the plane [Gibson and Ashby 1999]. The cells are usually hexagonal as in the case of the bee's honeycomb, but they can also have other shapes, square, triangular and re-entrant hexagons. Similarly to regular hexagons, also repeating arrays of re-entrant hexagonal cells with an external an-

gle $2\theta = 120°$ (Fig. 6.13) completely tile the plane, an important property which will guide the upcoming developments.
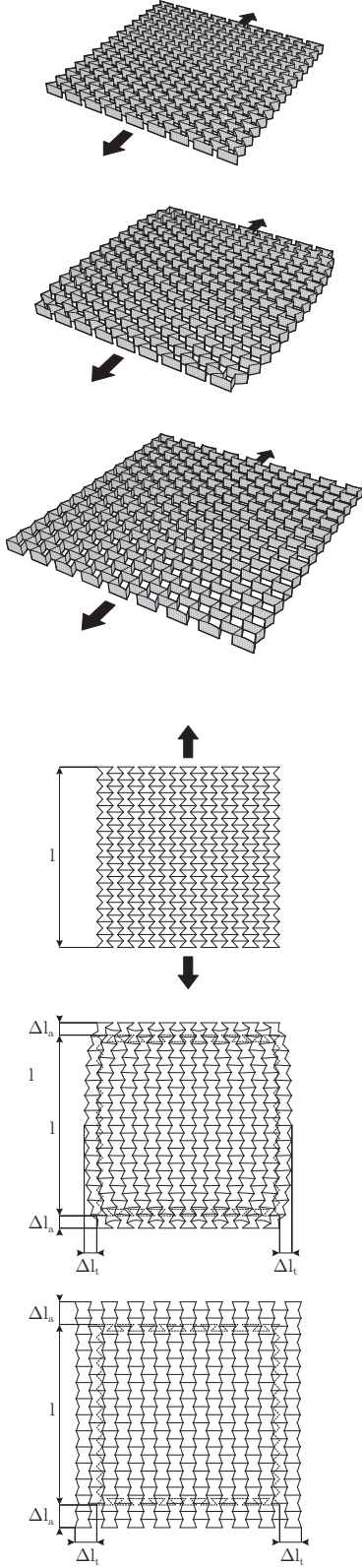
To study the deformation properties of auxetic honeycombs, we focus on Fig. 6.11a which depicts an array of inverted honeycomb cells packed together to form a cellular solid structure. Being interested in assessing the Poisson's ratio of this structural object, we apply a controlled support displacement to one of the edges and measure the degree of lateral deformation of the structure. Indeed, the sides expand, confirming the auxetic nature of the inverted honeycomb. The simulation of the auxetic honeycomb is run once by keeping fixed the lateral expansion of the top and bottom edges (Fig. 6.11b) and once leaving the whole pattern free to expand, i.e. leaving the edges free to move along the x axis (Fig. 6.11c). The constrained pattern bulges out in the middle, as the edges are constrained to remain the same length. The unconstrained pattern almost scales isometrically with respect to the initial pattern. Focusing on a detailed view of a cell, it can be noticed how the expanding mechanism works and where it is deriving from. Therefore, at a macro level the inverted honeycomb exactly behaves auxetically.

Having assessed the sign of Poisson's ratio for inverted honeycombs, we need to determine the value of the ratio itself. Comparing the axial dilation Δl_a of the structure with the transversal expansion Δl_t it can be seen that the two values are almost identical. This is true for any specimen's geometry, as it is a property of the pattern independent of the external boundaries of the test piece. As seen from equation 6.1, Poisson's ratio is the ratio between these two quantities, which in this case are identical. This means that the value of Poisson's ratio is practically -1. This implies that inverted honeycombs are placed exactly at the lower boundary of the theoretical limits prescribed for Poisson's ratio.

6.2.2 The regular honeycomb

Having demonstrated the existence of auxetic behaviour in the inverted honeycomb, the other aspect left to be dealt with is the upper limit of positive Poisson's ratio structures. As mentioned previously, this will be solved in a conceptually similar fashion.

The upper limit of Poisson's ratio exists for isotropic materials. This derives from the interdependency of the elasticity constants for isotropic materials seen in equation 6.2. Theoretically, anisotropic materials can assume any value [Ting and Chen 2005], as the limit of incompressibility is no longer as restrictive as for their isotropic counterpart. The regular hexagonal honeycomb belongs to that class of anisotropic structures which present a positive Poisson's ratio almost equal to one. This is shown in Fig. 6.12, where a regular

FIG. 6.11

Deformation of an auxetic pattern. The amount of axial stretching is equal to the lateral expansion. a. Structural system, b. Constrained edge, c. Unconstrained

honeycomb cellular structure (internal angle $2\theta = 120°$, Fig. 6.13) is subject to an axial support displacement. Opposite to what has been seen for the inverted honeycomb, in this case the lateral contraction is indeed positive, as it stretches towards the interior of the honeycomb. Fig. 6.12b shows the analysed honeycomb specimen constrained along the top and bottom line edges, therefore unable to contract freely. In this way under traction the comb bulges inwards creating the arched line visible in the top view. The comb in Fig. 6.12c instead is free to move laterally, therefore it scales proportionally to the prescribed amount of support displacement.

The lateral striction effect is way more pronounced compared to what can be observed in a strip of metal for instance. In fact, measuring the amount of axial displacement Δla and the amount of lateral stretching Δlt we notice that, as in the case of the auxetic honeycomb, both values are almost identical. This confirms that regular honeycombs do indeed approach a value of Poisson's ratio equal to +1, which is way beyond the incompressible limit of 0.5 for conventional, isotropic materials. A closer look to the stretched patterns clearly shows the mechanism that allows this effect to occur. The single cells can be considered as a regular arrangement of plate elements combined together and rigidly joined at their intersecting nodes. Being thin and slender, the individual plates of the cells can undergo a large degree of bending, therefore deforming substantially compared to their original configuration. Each cell contributes a certain amount of stretching and rotation in the whole system, which summed together with all the neighbouring cells gives rise to the global behaviour of the global pattern. This can be thought as adding up small contributions of translation and rotation to achieve a larger movement of the whole structural system.

So far we've seen that the regular honeycomb and the inverted honeycomb assume the extreme values of -1 and +1 as Poisson's ratio. Although in theory the lower boundary of -1 and the upper boundary of +1 could be exceeded, reaching even higher values, we will concentrate the further developments of this work on these two classes of cellular structures, limiting the extremal values to |1|. This limitation will obviously have consequences also on the bending of the structures which will be discussed later on. Other values of Poisson's ratio can be achieved by changing the geometry and topology of the pattern. Uncountable variations have been studied and developed by researchers worldwide [Evans and Alderson 2000, Greaves et al. 2011], and a complete review is utterly impossible. For reasons of simplicity, this works considers exclusively the regular and auxetic honeycombs, focusing on their geometrical generation and bending behaviour.
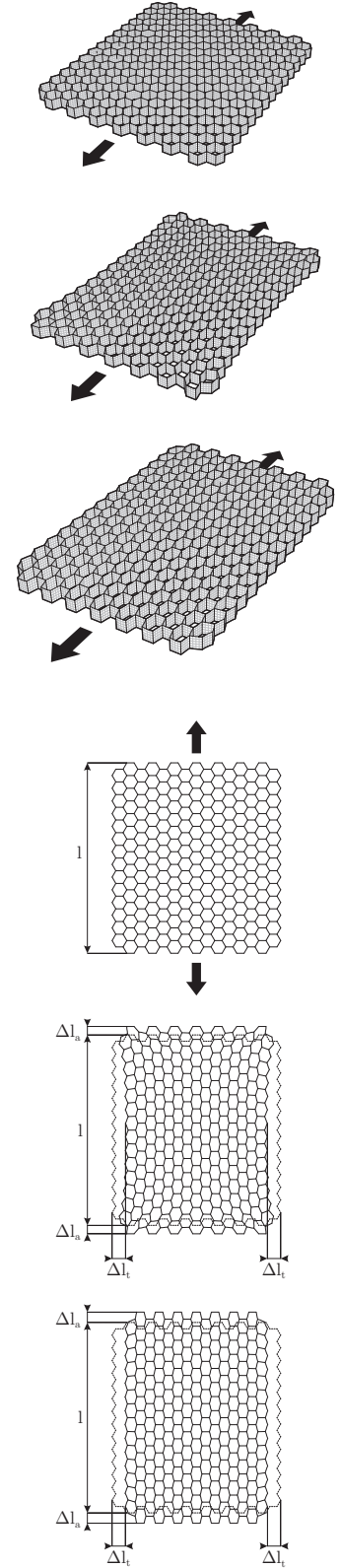
117

Pattern transition between the auxetic, zero Poisson's ratio and regular honeycomb
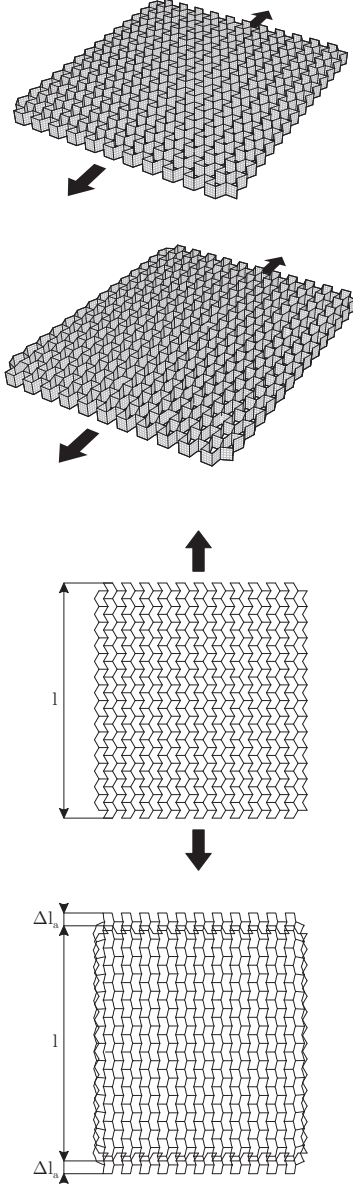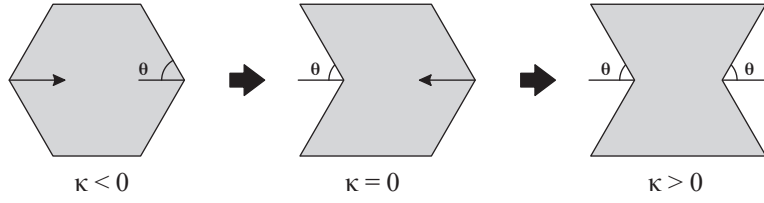
$$\kappa < 0 \qquad\qquad \kappa = 0 \qquad\qquad \kappa > 0$$

6.2.3 The zero Poisson pattern

One aspect which still needs to be clarified is how to achieve all the intermediate values of Poisson's ratio between -1 and +1, and how these transitional geometries influence the Gaussian curvature under bending. Intuitively, a smooth transition between the two honeycomb shapes should achieve the expected result. It will be shown that this is exactly the case, guaranteeing that all the curvature values can be reached using the same strategy.

In Fig. 6.13 the geometries of the regular and inverted honeycombs are shown with the transitioning pattern in between. By adopting an internal angle of 120° for the inverted honeycomb cell it is possible to completely tile the plane with the same number of regular hexagons. This is an extremely important property, as in this way one set is the dual of the other, and it is therefore possible to transition smoothly between the two patterns without interruptions. As the top and bottom edges of the auxetic cells are coincident with those of the regular hexagon, the only edges that need to be adjusted are the internal convex ones. This can be achieved by shifting the internal vertices one at the time towards the exterior, until the internal angle of the regular honeycomb cell is reached. In this way all the transitions between these two states are totally valid and do not break the regular tessellation of the plane. Here, only one of the two vertices is shifted until the 'fish scale' pattern is reached (Fig. 6.13b), after which the second vertex is allowed to transition from its concave configuration to the convex one.

Lying at the transition between the positive and the negative pattern, the 'fish scale' pattern (Fig. 6.13b) is supposed to possess a 0 Poisson's ratio. For this reason it will often be referred to as the *zero Poisson ratio* pattern or the *neutral pattern* to distinguish it from the regular and auxetic honeycombs. From Fig. 6.14, which again shows the amount of lateral contraction/expansion with respect to the axial stretching, it is clear that no transversal effect occurs in the deformation process, confirming that indeed the pattern possesses a vanishing Poisson's ratio.

Zero Poisson's ratio pattern under axial displacement. The lateral expansion in the specimen vanishes in this case

6.2.4 Bending and its effects on Gaussian curvature

To conclude this section we focus on the deformation effects that bending has on the different pattern typologies. We do this first from a qualitative point of view, demonstrating the effects empirically with the aid of prototypical test specimens. The specimens were created using a polyjet 3d-printing method. Further technical details on the employed fabrication approach will be provided in the upcoming sections.

The three main patterns were printed in the size of 10 cm x 10 cm x 1cm with a cell wall thickness of 1 mm. The minimum resolution detail that can be printed on Connex polyjet machines is 0.7 mm, but for reasons of material safety it is recommendable to print with a higher thickness. Therefore it was chosen to print the specimens with a 1 mm thickness, although the reduced scale would have required a thinner cross-section. The higher stiffness is nonetheless compensated by the mechanical properties of the material. These are reported and discussed in the following sections.

Fig. 6.15 shows the three specimens in their bent state. Comparing the different patterns, it can be seen that for the negative Poisson's ratio a spherical curvature is achieved, in the case of the regular honeycomb the Gaussian curvature is negative and finally for the 0 Poisson pattern the bending simply returns a cylindrical surface with vanishing Gaussian curvature. This indeed confirms the assumptions that have been made so far regarding the bending behaviour of the patterns in relationship to the values of Poisson's ratio. The secondary curvature effects described back in Fig. 6.7 and Fig. 6.9 regarding a conventional beam and a hypothetical
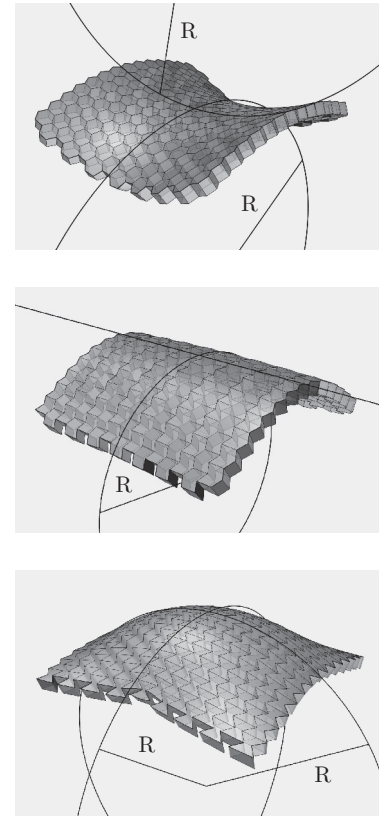
FIG. 6.15

Specimens showing the effects of bending on the Gaussian curvature. a. Anticlastic curvature, b. Cylindrical surface, c. Synclastic curvature
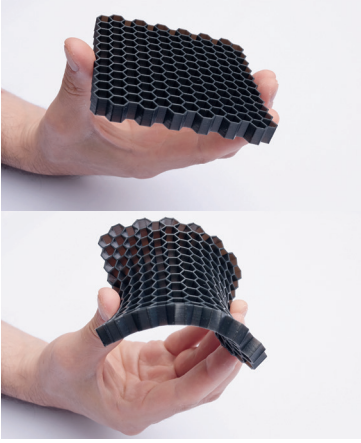
Bending of the regular honeycomb produces a surface of negative Gaussian curvature
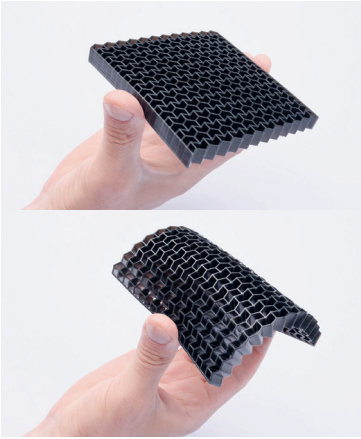
Bending of the zero Poisson's ratio pattern produces a cylindrical curvature
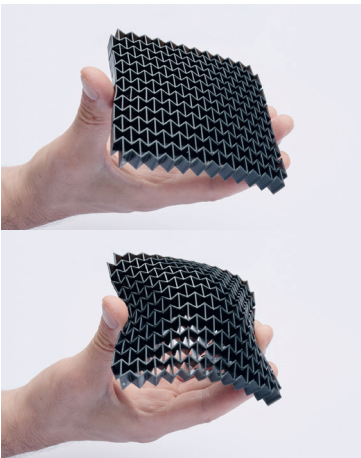
Bending of the auxetic comb produces a surface with positive Gaussian curvature

auxetic beam, assume a strong relevance in the context of graded cellular structures. As the transversal strain is almost the same magnitude as the induced axial strain, also the amount of bending will be comparable in both directions. Furthermore, the intrinsic deployment mechanisms of the individual patterns allow to stretch these cellular structures way beyond the stretching percentages of typical materials. Depending on the geometry of the cells and the internal angle between the plates, the maximum stretching can be controlled and tweaked to reach very high values. For the type of pattern used in this work, the internal cell angles allow for a maximum stretch of 20%. Looking at the stretched patterns in Fig. 6.11b, 6.12b and 6.14b and more in detail in Fig. 6.20, it is clear that the maximum stretching ratio is reached when the webs of the individual cells are almost vertical. Beyond this stage, the bending dominated deformation gives way to a membrane stress state and the structure inevitably departs from its elastic behaviour.

A full simulation of the bending process and the deformation of the specimens was setup and run in SOFiSTiK. The results are reported in Fig. 6.22 of the following section. In Fig. 6.15b a surface is created for each test case by interpolating the nodes of the deformed geometry derived from the Finite Element simulation. The surfaces are used to analyse the Gaussian curvature and the geometrical properties of the bent patterns. As expected, the curvature values show a negative, zero and positive curvature for each pattern respectively. Extracting the principal curvatures of the surfaces it can be seen that the radii of the osculating circles are equal in the two directions for the auxetic and regular honeycomb patterns. In the case of the neutral pattern, the maximum principle curvature corresponds to the main bending axis, i.e. the straight rulings of the cylinder. For the auxetic and regular patterns, the fact that the curvature radii are similar means that exactly the same value of curvature in the direction of actuation will be mirrored in the transversal direction as a secondary side effect. This leads to a 1:1 correspondence between the two curvatures. In this sense the value of Poisson's ratio can be understood as affecting bending: the bending radius induced in one direction will produce a radius of curvature of equal magnitude in the transversal direction, with sign dependant on the type of pattern.

By interpolating the patterns through changes of the cells' internal angle, a variation in the global mechanical properties are achieved. Transitioning between the auxetic honeycomb to the regular honeycomb passing through the neutral pattern will return a smooth spectrum of Poisson's ratio values from -1 to +1. As expected, this also has a direct

consequence on the bending behaviour of the transitioning elements. The Gaussian curvature for these intermediate stages will be a linear interpolation of the values reflected by the pattern geometry. Therefore a pattern with a value of -0.7 will return a secondary curvature of 70% the principle bending curvature, but oriented in the opposite direction.

In conclusion, we have qualitatively shown how the geometrical arrangement of the individual cells heavily influences the mechanical response of the structure. The regular honeycomb, the auxetic pattern and the neutral pattern indeed deliver curvatures consistent with their value of Poisson's ratio. In the following sections a general strategy for the exploitation of this effect will be derived.

121
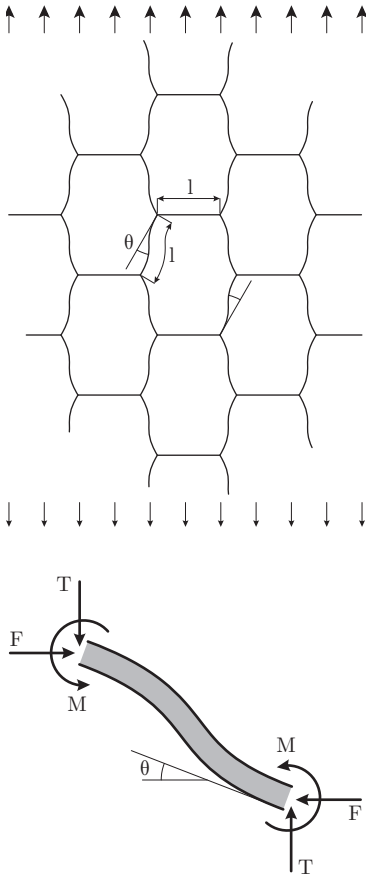
FIG. 6.20

Cell deformation by pure bending of the walls under in-plane axial strain
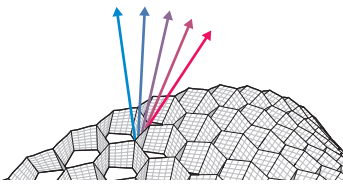
FIG. 6.21

Under global bending the cell's walls undergo a combined torsional and bending mechanism that raises the structure out of the plane

6.3 Mechanics of graded cellular structures

Considering the bending behaviour of honeycombs in the linear elastic approximation, this can be explained as a combined bending and torsional effect of the individual plate elements which form the walls of each cell. As seen in the previous chapters, bending and torsion have strain energies of similar magnitude, and are mainly responsible for the large deformations of plate elements as they are at least one order of magnitude smaller compared to membrane strain energy.

Pure bending deformations would not be sufficient to induce out-of-plane secondary effects. This can be seen in Fig. 6.20, where pure bending is induced in the cells of a honeycomb via in-plane axial strain. In a first approximation, the walls of the cells behave as short beams with a stiff connection at the nodes. The typical S deformation can be seen in the depicted cell's detail. In this state the honeycomb only experiences bending of the walls, and the deformation effects are confined within the plane of the structure. With the introduction of torsion the response of the cells changes. To balance the out-of-plane effect of bending, the walls of the cells have to bend and also twist, activating the secondary effect derived from Poisson's ratio. The torsional mechanism and the axial rotation of the single plates is responsible for the anticlastic or synclastic configuration the honeycomb assumes (Fig. 6.21). In the case of regular honeycombs the twisting has the effect of rotating the cell walls in the reversed direction of bending, therefore inducing a negative Gaussian curvature. The opposite is true for auxetic honeycombs where the cell walls will rotate in the same direction of bending, delivering a positive Gaussian curvature in the structure.

It is necessary to stress out that also these types of cellular structures suffer from the inherent contradiction of bending-active structures. This means that post deformation, the stiffness of the elements must be somehow restored. This could for instance be achieved by laminating the deformed core, therefore freezing the cellular structure in the sought configuration.

6.3.1 Influence of pattern density

Despite the single cells being limited in terms of deformation, the global behaviour of the honeycomb can be interpreted as an addition of micro effects occurring locally, which added up return an amplified global effect. The global behaviour of the honeycomb is in general independent of the size of the cell. The same amount of support displacement delivers same values of transversal contraction. This means that the Poisson's ratio of the honeycomb is scale independent with respect to the cell size.
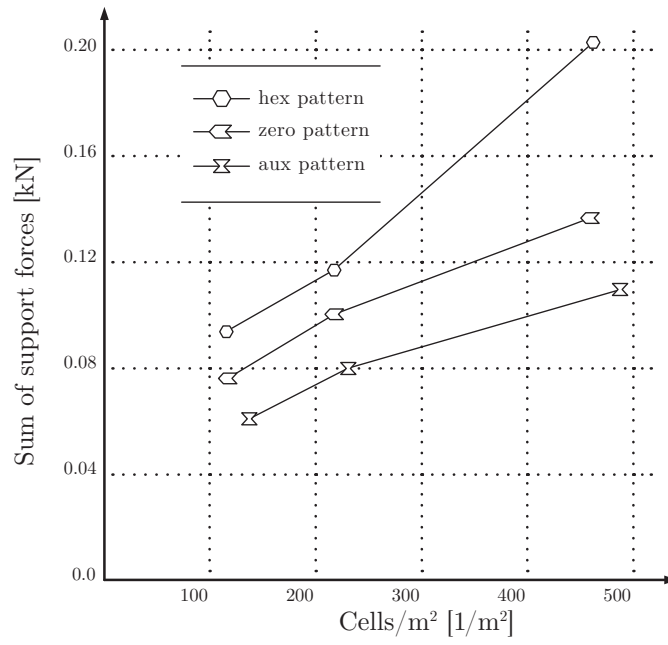
FIG. 6.22

Influence of pattern density over stiffness measured through the sum of support forces
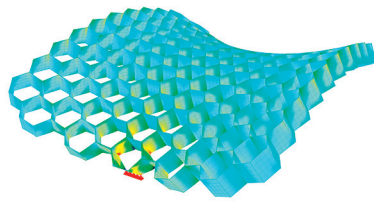
hex pattern
115 cells/m²
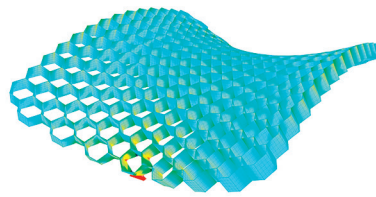
hex pattern
217 cells/m²
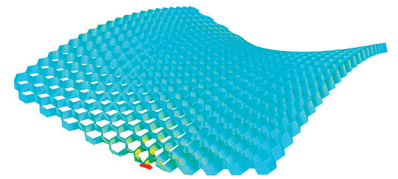
hex pattern
462 cells/m²
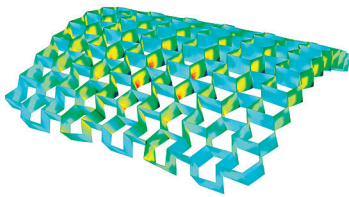
zero pattern
115 cells/m²
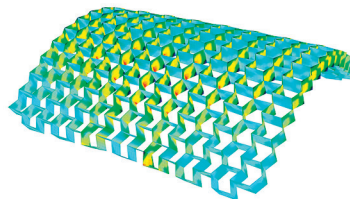
zero pattern
217 cells/m²
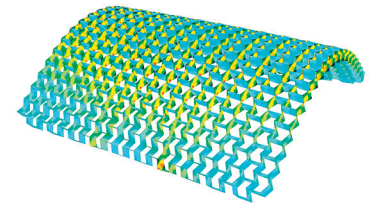
zero pattern
462 cells/m²
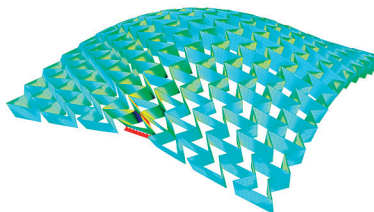
aux pattern
137 cells/m²
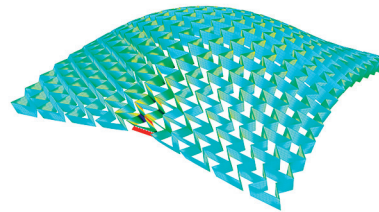
aux pattern
230 cells/m²
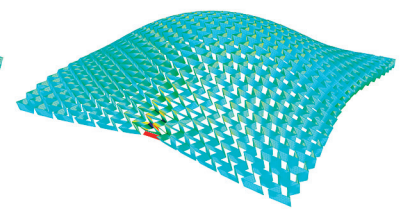
aux pattern
488 cells/m²

The same can be said of the behaviour of the comb under bending which is shown in Fig. 6.22. Here the curvature radius in the transversal direction is of the same magnitude of the bending radius, despite the variation in size of the base cells. This aspect is fundamental as it means that a change in density will not affect the response and the geometry of the structure. To correctly capture the bending and torsion of the plate elements and to obtain an acceptable compromise between accuracy and computation time, a mesh sensitivity analysis was performed with mesh size equal 1/2, 1/4, 1/6 and 1/8 the height of a cell's wall. The results were convergent and four elements were judged sufficient for the analysis. For additional accuracy the simulations of the bending test cases were run with five elements per row distributed over the cell's height. The subsequent simulations presented in this chapter make use of four elements per row due to the complexity of the models and to reduce the CPU time required for the full calculation.

If the type of response is not influenced, what effect does a denser pattern have then? The sum of the support reactions provide a good indication of the effect deriving from a pattern densification. Looking at an example of two springs, with the second one twice as stiff as the first one, for an equal support displacement the support reaction will be twice as big for the stiffer spring compared to the first one. For the regular honeycomb pattern, the summation of the support reactions is reported in Fig. 6.22. Increasing the amount of cells keeping the area constant has the effect of stiffening the specimen. Precisely, the sum of support reactions will be approximately proportional as can be noticed in the graph. This is intuitively obvious as a pattern densification will lead to an increase of matter of the system. The more matter the stiffer the system will be.

The stiffening effect deriving from a densification of cells needs to be taken into account when combining areas of variable density, as the change in stiffness will lead to a change in curvature of the system. Activating through support displacement a specimen with areas of changing density will induce different curvature radii in the structure, as under the same amount of displacement the softer area will deform and bend more than the stiffer part which will tend to oppose larger resistance to the bending. This needs to be taken into account for changing curvature radii.

In terms of structural behaviour, the deformed spatial patterns can be considered similar to grid shells with elements extruded in the normal direction of the base surface. The topology of the grid will be dependent on the local Gaussian curvature of the shell, and will depart substantially from the typical cell geometries employed for grid shells, these normally being either triangular or square. Recent research work has being focusing on

the influence of the grid's geometry on the structural capacity and buckling behaviour of the grid shell [Malek and Williams 2013, Pietroni et al. 2014, Tonelli et al. 2016]. These works have shown that hexagonal and pentagonal free-form grid shells can be as effective in structural terms as a quadrilateral regular grid, and under certain circumstances perform even better.

In comparison to a classical grid shell typology, the bending active cellular structures object of this study present a few, fundamentally different characteristics which strongly influence the global mechanical behaviour. Topologically the two types of structures might look similar, but the differences in their constituent elements heavily influence their mechanical response. In the first place the cells are made of plate-like elements, with thickness considerably smaller than the other two dimensions, giving origin to an assembly of planar, 2d elements. This differs from the members of typical grid shells which tend to be one dimensional elements acting as beams rather than plates. The larger cross-sectional height of the elements increases the load bearing capacity of the grid, as loads will be carried more effectively as a consequence of the higher sectional inertia.

This positive effect is counterbalanced by the increased sensibility to torsional buckling of the webs. Thin, slender cross-sections which extend in two dimensions are more prone to torsional buckling, as opposed to linear elements which are mainly affected by axial buckling due to their geometry. Moreover, in its deformed and final state the plates of the cellular core will have already undergone a certain degree of torsional rotation as a consequence of the actuation mechanism. This means that the loading in the deformed state will not happen purely in the plane of the plate elements, but will act directly on the buckled elements. These are the two main aspects which characterise the mechanical response of the bending active honeycombs. Although not ideal in terms of load-bearing capacity, this might be an acceptable trade-off for the morphing abilities that these structures offer.

To gain further insight on the effects of pattern densification, the first eigenvalue of the test geometries was also calculated. Fig. 6.23 shows the results of the analysis. Just as in the case of the form conversion spheres studied in chapter 5, the eigenvalues of the patterns are a good indicator of the global stiffness and the quality of the structural behaviour. Following the bending process seen in Fig. 6.22, the edges of the bent geometries are then kept in place by adding a series of simple supports for each edge node. By doing so we force the whole structure to be activated and in this way gather a better understanding of the global effects that influence the mechanical response. Otherwise, by keeping only the edge supports used for displacing the objects the structures almost

FIG. 6.23

First eigenfrequency values for
patterns with varying density
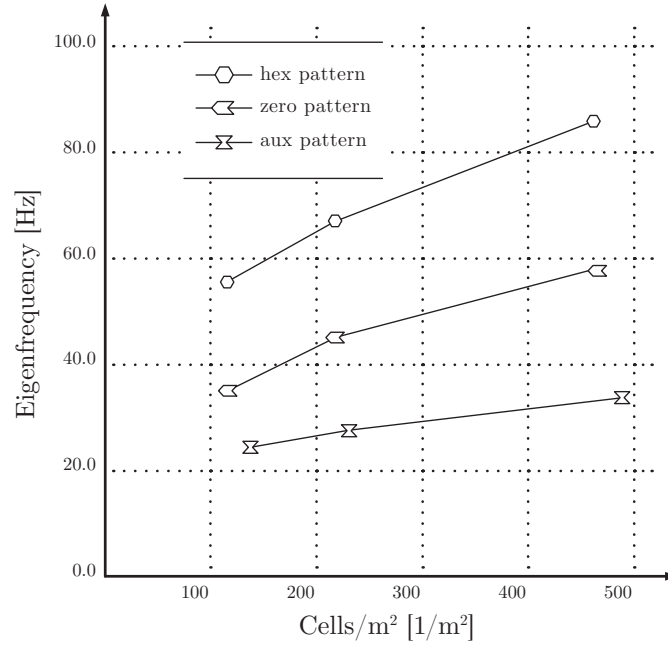
rotate rigidly around their axis of support and the internal
walls of the cells do not get activated at all.

The results of the eigenvalue analysis are consistent
with the ones seen for the sum of support reactions. A denser
pattern delivers higher eigenvalues from which we can conclude
that also the stiffness grows accordingly. Comparing the curves
of Fig. 6.23 with those in Fig. 6.22 we notice that the slope
of the increasing curves is less steep in the case of the eigen-
value analysis. This was also noticed for the study in chapter
5. Nonetheless, the growing trend is still well visible from both
diagrams. Interestingly, also the difference in stiffness between
the three patterns is recognisable from the graph. Just as in
the case of the support displacement analysis, the hex pat-
tern shows to be the stiffest one, followed by the zero pattern
and the auxetic one. This confirms the observations that were
made so far on the mechanical qualities of the single patterns.

Similarly to the analysis performed on the sphere ge-
ometry for the form conversion approach, major differences
between the dead geometry and the bent geometry are not
noticeable. In the case of the eigenvalue analysis performed
here, the difference between the two cases resulted almost im-
perceptible and it was omitted from the graph. A probable
explanation for this phenomenon is that the deformation of
the individual plates of the cells is so minimal that the inter-
nal stress state influences the structural response only mini-
mally. In conclusion, the influence of prestressing actions can
be safely disregarded, as the geometry of the structure plays
a more important role compared to secondary effects deriving
from the form-finding.

6.4   Methodology

Having identified a mechanism most likely appropriate for the sought purpose, a general principle guiding the pattern design needs to be developed. The fundamental question here is: given a double curved surface, what is the best pattern design which returns the original surface under bending. To be more specific, the sought design is that which minimises the strain energy of the system, as the strain energy is a measure of how much the undeformed configuration deviates from the final geometry. In chapter 4 it has been demonstrated that bending deformations minimise the strain energy in comparison to membrane deformations, and are also responsible for the large deflections the structure experiences when bending a sheet of material. Following the same train of thought, we seek for patterns which will induce only bending and torsional actions in the honeycomb, avoiding membrane strain in the material. These are the primary actions responsible for the large deformations and shape changing mechanisms of the structure.

The problem needs to be broken down in several steps. These can be summarised as following:

1.   Analyse the Gaussian curvature of the base surface.
2.   Flatten the base surface keeping track of the position of the original curvature values.
3.   Create a corresponding pattern which matches the curvature values.
4.   Map the pattern to the flattened domain.
5.   Define the actuation mode and place the actuators if necessary on the flattened pattern.
6.   Bend.

The first step involves a simple Gaussian curvature analysis of the base surface. Depending whether the geometry is an implicit surface, i.e. NURBS, or explicit surface, i.e. mesh, the analysis can be performed using commands often provided by the 3d-modelling software in the case of implicit surfaces, or in the case of meshes by using the discrete curvature algorithm discussed in chapter 3.

The flattening of a double curved surface is a complex challenge which has been providing topics of research for generations of mathematicians and geometers. Probably the best known field of application is map projections. A map projection is a systematic transformation of the latitudes and longitudes of locations on the surface of a sphere into locations on a plane [Snyder 1989]. As seen from Gauss's Theorema Egregium, a sphere's surface cannot be represented on a plane without distortion. This also applies to any other double

curved surface, which cannot be unrolled into a plane without sacrificing certain properties of the source surface. In general, map projections can be constructed to preserve at least one or a combination of properties of the base surface. These include area, shape, direction, distance, scale to name a few. The well-known Mercator's projection is the most used map of the globe and can be seen almost in every textbook and hanging from walls of schools. Developed for navigation purposes, Mercator's projection is the most prominent example of conformal mapping. Conformal maps preserve angles locally, meaning that they map infinitesimal circles of constant size anywhere on the Earth to infinitesimal circles of varying sizes on the map. In contrast, mappings that are not conformal distort such small circles into ellipses, therefore the relative angle between two points is not preserved. The most important property of conformal maps is that relative angles at each point of the map are preserved, and locally in the neighbourhood of any point the direction of scaling is constant, although the direction varies smoothly throughout the whole surface map. Equal-area and equidistant projections also exist, which respectively preserve the area of the surface in the first case and the distance between two points in the latter.

In chapter 3, along with the derivation of Gauss's Theorem, an important remark was made on the change of Gaussian curvature and the change in length of material fibres. The Theorem demonstrates that bending deformations leave the Gaussian curvature unchanged, and that to change the curvature of a surface stretching or shortening of material is required. Therefore, a change in Gaussian curvature is inevitably accompanied by strain of the material fibres. In the previous paragraphs of this chapter, we've seen that due to Poisson's effect a strip of material will change its curvature also in the direction perpendicular to the direction of bending. This is due to the stretching and expansion that transversal portions of material undergo under bending. Following the curvature analysis of the base surface, we can consider the network of principal curvature directions as being the privileged directions for bending. Specifically, the principal curvature direction with the maximum absolute value will be the main direction of bending, whilst the orthogonal direction will be the one that bends as a consequence of Poisson's effect.

Having identified a general rule that relates the principal curvature directions of the base surface with the directions of bending and the orthogonal directions affected by Poisson's effect, we now need to find a transformation which maps the double curved base surface onto the plane by preserving the properties described in the rule seen above. In synthesis, the mapping has to preserve the length of the principal direction

of bending whilst concentrating the strain (either compression or expansion) in the orthogonal direction. Without entering superfluous mathematical details, we mention that the NURBS 3d-modelling software Rhino implements a 'Squish' command which approximates well the task described above. For the command a series of options are available to assign different properties to the surface to unroll, therefore defining areas which have to behave as an inextensible material (the principle directions of bending), and areas that are allowed to change length and undergo strain (the transversal directions under Poisson's effect). The details of this scheme are shown in Fig. 6.24. Here a torus and its principle curvature directions are shown. The flattened pattern (Fig. 6.24b) maintains the correspondence between the principal curvature directions on the three-dimensional surface and its planarised version. The radial directions, being the ones of main bending, are preserved in length during the flattening operation. Despite relying on predefined algorithms for this operation, the results behave well and have been used for the following phases of the pattern definition and simulations. Improvement for this step is nonetheless still required and object of study for the future.

The pattern generation has proven to be a challenging task with no easy solution. The sought result is supposed to be a graded cellular pattern which transitions without discontinuities from auxetic to regular honeycomb cells according to the Gaussian curvature values of the flattened outline geometry. A necessary requirement is that the cell orientation stays consistent with respect to the principal directions of bending. Moreover, the pattern necessarily needs to be a hexagonal mesh with regular cells and valence 3 vertices, an aspect which adds an additional layer of complexity to the required properties of the pattern. Meshing algorithms create meshes which perfectly fit the domain boundaries. Unfortunately these meshes are not suitable for our purposes as the degree of mesh refinement is hard to control and there is often very little or no control at all over the internal angle of the elements. These aspects inevitably lead to the creation of unstructured meshes which do not comply with the required properties.

To overcome these limitations, other meshing strategies had to be devised. The adopted approach makes use of a transformation of the plane known as *Schwarz-Christoffel mapping*. In complex analysis, a Schwarz–Christoffel mapping is a conformal transformation of the upper half-plane onto the interior of a simple polygon. Being a conformal mapping between two domains, it means that the angles between elements contained in the first domain will be exactly preserved under the transformation. In its original form it was devised by Elwin Bruno Christoffel and Hermann Amandus Schwarz as a
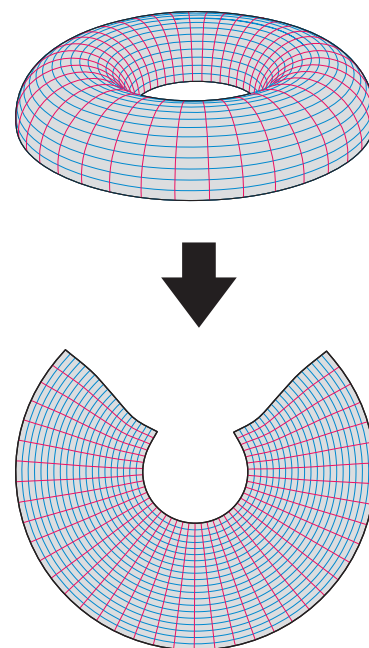
FIG. 6.24

Flattening map of the torus. The flattening operation preserves the length of the principal direction of bending, in this case the radial curves of the torus

FIG. 6.25

Schematic view of the Schwarz-Christoffel mapping. The mapping is conformal as the angle between two points in the canonical domain are preserved upon transformation

canonical domain   physical space
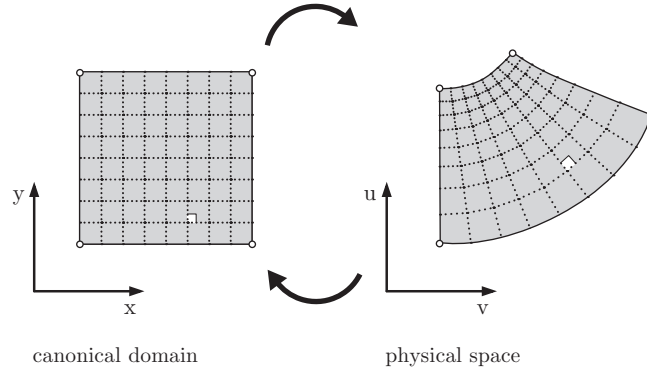
conformal mapping between the lower bounded half-plane and a closed polygon. Recent developments in the theory and implementation of Schwarz-Christoffel mappings have extended their application abilities to transformations between closed polygonal domains [Driscoll and Trefethen 2002]. Therefore the mapping does not necessarily occur only between the half-upper plane and a closed arbitrary polygon, but also from an arbitrary closed polygon to another arbitrary closed polygon.

Without further ado on the hairy mathematical details of the underlying theory and numerical solutions for Schwarz-Christoffel mappings, we point out that for the implementation a specific tool for Matlab was employed. The tool is called Schwarz-Christoffel Toolbox for Matlab and is being actively developed by Driscoll and Trefethen and available for free at the time of this writing. The functioning of the SC Toolbox is fairly simple: given a domain, in our case the outline of the flattened surface, this is mapped conformally to a target domain of choice along with everything contained within the source domain. This operation works in both directions, from the source to the target domain and vice versa (Fig. 6.25). In this way a curvilinear source domain can be mapped onto a rectangle which can then be easily tiled following the requirements discussed above. The target domain, along with its meshed interior is then mapped back onto the source domain. As the transformation is conformal, the internal angles of the elements contained in the target domain will be preserved during the mapping back to the source domain. This operation provides the base mesh of the graded cellular structure.

Fig. 6.26 shows the complete pattern generation process for the embedded approach method in the case of a torus. The surface of the torus is first flattened and mapped to a rectangular domain, the so-called canonical domain. The canonical domain is then populated with the elements of the pattern (Fig. 6.26a-b) and interpolated depending on their curvature value (Fig. 6.26c). From Fig. 6.26a and Fig. 6.26b it can clearly be seen that the same domain can be populated

canonical domain

$\kappa < 0$

$\kappa = 0$

$\kappa > 0$

131
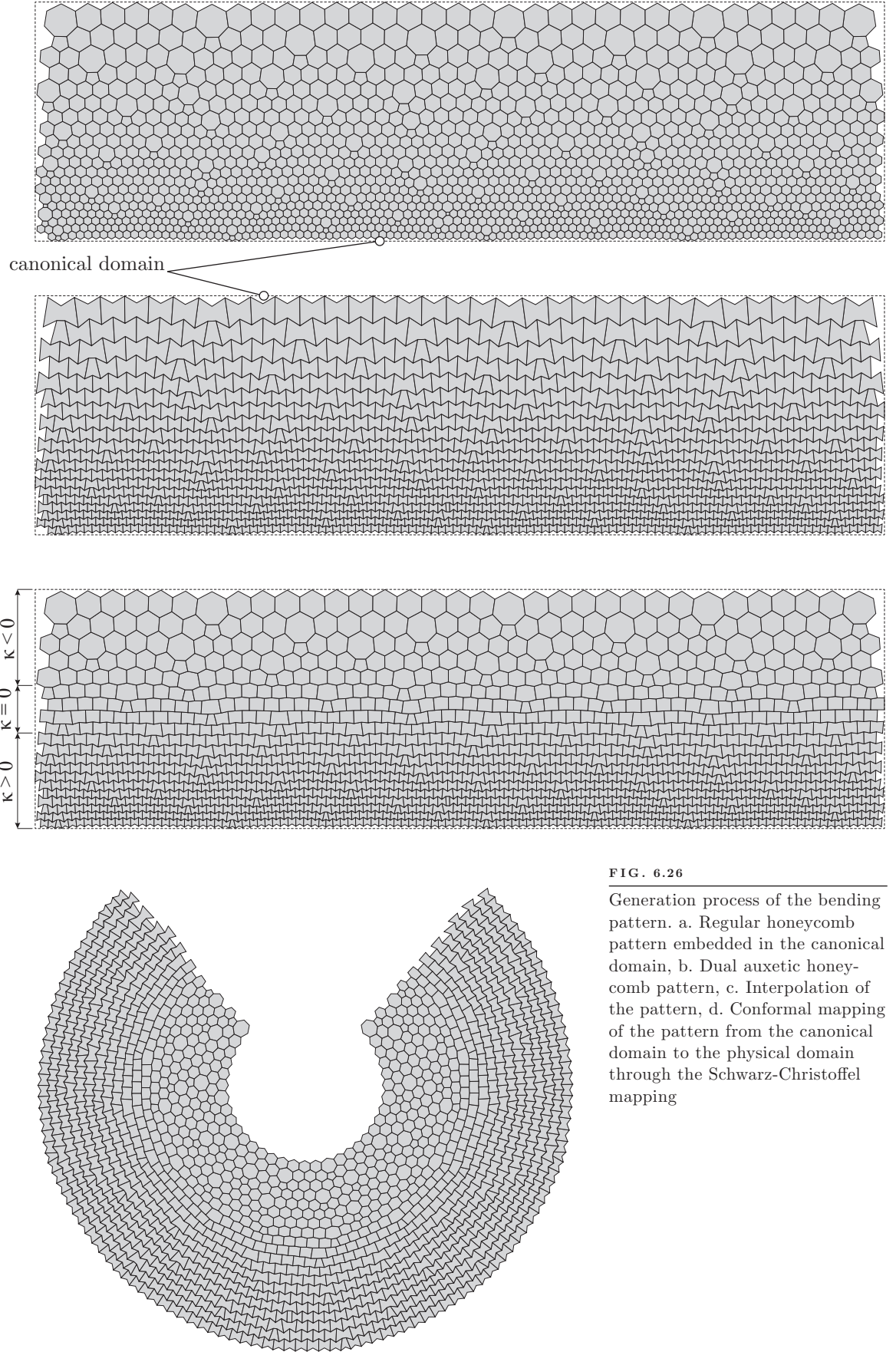
with either pattern, as long as the proportions between the individual cells are maintained. This is an important property as both patterns can be used to completely tile the plane, or in our case any polygonal domain. The interpolation between the two patterns follows the process described in Fig. 6.13. The values of the Gaussian curvature of the target surface are mapped onto the flattened domain, providing a one to one correspondence between the surface and the mapping and uniquely defining the expected curvature in a specific area of the canonical domain. Depending on this value the vertices of each element are shifted into the correct position, guaranteeing a smooth transition between the elements. In this way a seamless combination of cell elements is achieved as seen in Fig. 6.26c. The pattern obtained in this way is then mapped back onto the curvilinear flattened domain of the torus by using the Schwartz-Christoffel mapping tool that was previously described (Fig. 6.26d).

6.5 Method testing

The method presented was tested numerically and physically. Due to the manufacturing complexity, 3d printing technology was employed to fabricate the test pieces. The reduced size of the prototypes required the use of flexible materials to test the deformation of the cellular structures. As curvature scales inversely with respect to the radius of bending, a smaller size means higher curvatures and therefore higher bending stresses. Hence the use of flexible materials to compensate the reduced size of the printed prototypes. The specimens were realised using the PolyJet process for multi-material 3d printing. The PolyJet printing process jets layers of curable photosensitive polymer resin onto a build tray, which is hardened layer by layer by exposure to the light of a UV lamp. The employed 3D printing machine was an Objet Connex 500 by Stratasys, made available by Autodesk's Pier 9 in San Francisco as part of the author's residency. Owing to the fact that the materials are in liquid form prior hardening, it is possible to mix different materials to create intermediate properties between the two resins. The machine has a maximum printing envelope of 500mm x 400m with a nominal precision of 0.1mm. The high precision and the ability of mixing materials with different properties, also allows a granular control on the type of deposited material over targeted areas and along the cross-section of the specimens. Despite these advanced printing capabilities, tests have shown that a material variation within the same specimen does not modify noticeably the mechanical response.

132

The printing process is similar to many other commercially available machines for which a discretised mesh model of the geometry is required for processing and slicing. Compared to FDM (Fused Deposition Modelling) and filament printing, Polyjet printing requires additional support material to stabilise the structure during the process. Support material is partially soluble in water and does not influence the properties of the final 3d print. Besides, in the present case the printed geometries are simply extruded in the vertical direction, which is also the direction of printing, therefore requiring almost no support material at all. No additional curing or post-processing is then needed at the end of the printing process.

In the following sections the numerical Finite Element simulations of the developed test cases are presented along with the realised 3d-printed prototype that served as a physical assessment of the method. An analysis of the deviation between base surface and simulated model is presented in the closing section of the chapter.

6.5.1 Torus test case

For the physical prototyping the chosen geometry was a half torus sectioned along the horizontal plane with an external diameter of 323 mm and an internal radius of 117 mm. This specific geometry was chosen as the most representative as its smooth Gaussian curvature transition between the external synclastic part and the internal anticlastic part poses a challenging geometrical problem. Another interesting aspect of this geometry is its closed configuration. Topologically, a torus is a surface of genus 1, the genus being the number of handles. This forces the original shape to be split along the direction of the generatrix to avoid overlapping of material when flattening. Otherwise, the bending transformation would not be topologically acceptable as it would require material points to fuse together. This can be seen in Fix. 6.24 where the outline of the flattened torus is shown. The pattern generation follows the method described in paragraph 6.4 using Schwarz-Christoffel's transformation. The flattened torus is mapped onto the canonical rectangular domain which serves as a simplified base for the generation of the pattern. The pattern in the canonical domain is then mapped back to the torus outline using the inverse transformation delivering the pattern in Fig. 6.26d.

Having generated the fitting 2D pattern, a volumetric model for 3D printing was created. Each cell is thickened with a wall thickness of 1 mm, which is just above the recommended minimal thickness of 0.7 mm to make sure that no printing flaws might affect the performance of the specimen. The bending behaviour is heavily influenced by the torsional mechanism

of the individual plates of each cell. For this reason a minimal height of roughly the size of the cell is required to properly capture this effect. The specimen was therefore extruded in the direction orthogonal to the plane for 1 cm, which is within the height requirements given the minimum size of the cells.

The choice of material was mainly dictated by the type of materials available for the Connex printer. For the given size of the flattened torus (445 mm x 385 mm) and the smallest cell size, the maximum Young's modulus that would have been compatible with these size parameters would have been roughly 300 MPa. This is due to the fact that bending and torsion stresses scale linearly with respect to the bending radius and the torsional angle respectively, meaning that tighter curvatures will induce a stress state proportional to the stiffness of the material. Polyjet printers distinguish between so-called rigid materials and rubber-like materials. Rigid materials are named Vero materials, whilst rubber-like materials are a mixture between the base resin of the rigid material and varying percentages of a second flexible component named Tango. Rigid Vero polyjet materials available for the printer have an elasticity modulus which starts from 3000 Mpa. Tango rubber-like materials are defined by their Shore value and range from A60 to A95 Shore. As the starting values of stiffness for rigid materials would have been beyond the acceptable range required for the size of the prototype, rubber-like materials were employed for the realisation of the specimen. In this case the rubber-like material with the highest stiffness (i.e. Shore A95) was selected as having acceptable mechanical properties for the prototype. In this way it was possible to qualitatively test the structural response of the prototype.

Fig. 6.27-29 show the final printed prototype. The torus is presented in its flat state, intermediate deformation state and fully bent state. From the images, the bent cellular pattern is clearly assuming the shape of the torus. Both negative and positive Gaussian curvatures of the internal and external portions of the donut are visible, as well as the zero curvature transition between the two zones. A clarifying remark concerning the test case is due though. The pattern was created and the prototype printed before having identified the correct transitioning zero Gaussian curvature pattern discussed in paragraph 6.2.3. For this reason, the printed prototype slightly departs from the ideal configuration that would have been generated with the knowledge and the findings developed subsequently. Nonetheless, the prototype still behaved as expected despite slight deviations from the ideal surface, and delivered the expected results.

Besides assessing the embedded approach through physical prototyping, the results were tested also numerically
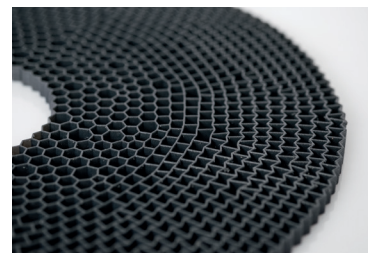
3d-printed pattern of the flattened torus
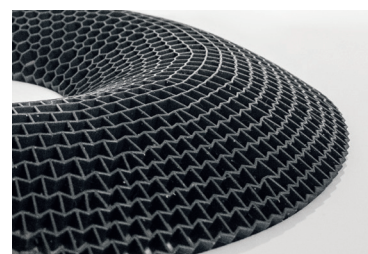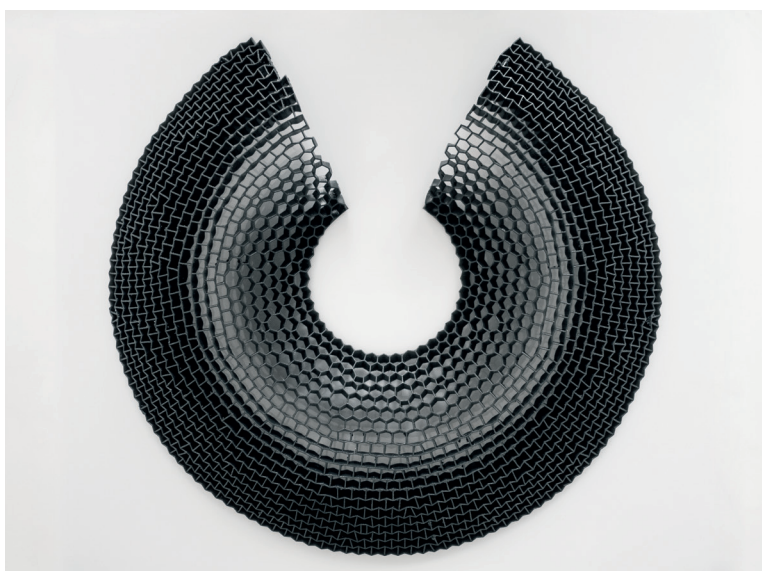
Intermediate bending stage

Torus in its fully bent configuration

von Mises stress
N/mm²

10.0

5.0
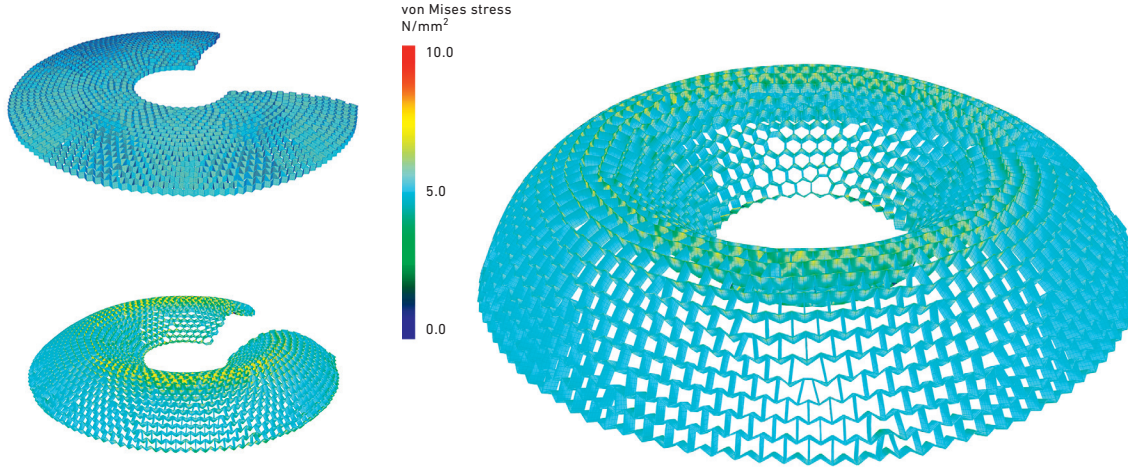
0.0

Von Mises stress plot of the form-finding process of the torus
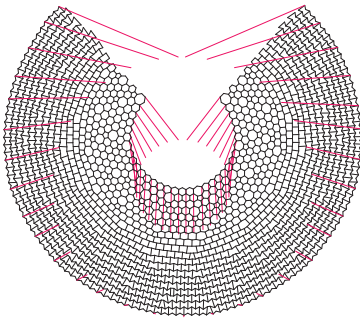
View of the arrangement of the contracting cables

with a full Finite Element simulation of the torus test case. Several actuation methods of the pattern had to be tested to identify the best simulation strategy. In general, an actuation by support displacement is to be preferred as introducing more constraints on the nodes has the effect of stabilising the numerical convergence of the model as it reduces the total degrees of freedom of the system and also the stiffness matrix of the structure is better conditioned. Especially in the case of flexible systems which undergo large deformations, the correct setup of the system is crucial for the convergence of the simulation. The most critical aspect derives from the fact that the shell elements already find themselves in a post critical buckled state, which coupled with the geometrically nonlinear large deformations that the elements undergo makes them extremely sensitive to numerical ill conditioning. Most of the times this translates into a negative value of the determinant of the stiffness matrix, which indicates a sudden loss of load-bearing capacity of the system and a dynamic behaviour which cannot be analysed unless other methods are employed, for instance the arc-length method described in earlier chapters. As SOFiSTiK does not implement methods for path tracing of post-critical states, the convergence of the results is a strong indicator that the structural system during actuation remains stable and within its elastic limits.

Different attempts of actuating the donut via a linear interpolation of the supports from the flat configuration to the bent one, failed to convey the expected results. This is due to the fact that the actuating mechanism clearly violates the natural way the structure would want to deform, leading to excessive torsion and bending in the elements. The high stress state and the buckling of the elements inevitably led to failure of the simulation. The alternative solution was to employ the contracting cable approach developed by Lienhard and the author. Using contracting cables to actuate the structure, the ac-

tual deformation path does not need to be known in advance. This method has the advantage of automatically actuating the structure by following the path of least resistance, although this might be unknown to the analyst. The contraction of the cable elements follows the path of the connecting nodes without introducing parasitic stresses or deformations in the system, drawing the privileged path for the moving nodes. Each edge node is connected with the corresponding end position via a cable element which is contracted through a strain load until the length of each cable has approached zero. In this way the nodes are free to move along their preferred trajectory. Details of the simulation setup are shown in Fig. 6.31.

The results of the simulation are reported in Fig. 6.30. As in the case of the physical prototype, also the form-found geometry well approximates the toroidal surface used as a base for testing the embedded approach. The von Mises plot shows an even and constant stress distribution over the elements of the structure. An area of higher stress concentration is recognisable in the transition zone where the Gaussian curvature of the surface is supposed to vanish. As mentioned in the opening of this paragraph, the tested geometry made use of a slightly different zero Poisson pattern compared to the optimal one described in chapter 6.2.3. For this reason, the area of transition is stiffer than the interior and the exterior of the torus where the correct regular and inverted honeycomb patterns were employed. Nonetheless, the simulation results show agreement with the physical prototype, besides demonstrating the validity of the developed embedded process for the generation of bending-active cellular patterns.

6.5.2 Downland test case

To further prove the validity of the embedded approach, a second test case was analysed. As this test case was developed after the author's residency at Pier 9, the results presented refer exclusively to the numerical simulations as a physical prototype was not realised. The geometry mimics the shape of the well-known Downland gridshell built by architect Edward Cullinan with the support of Buro Happold for the engineering [Harris et al. 2003].

Just like the torus, also the Downland gridshell lends itself well to geometric explorations because of the smooth curvature transition between different areas. For this reason it was chosen as a representative test case for the assessment of the embedded approach. The geometry of the Downland gridshell is technically less demanding than the torus, as the transition between negative and positive areas happens more gently and also because the surface does not have closed loops
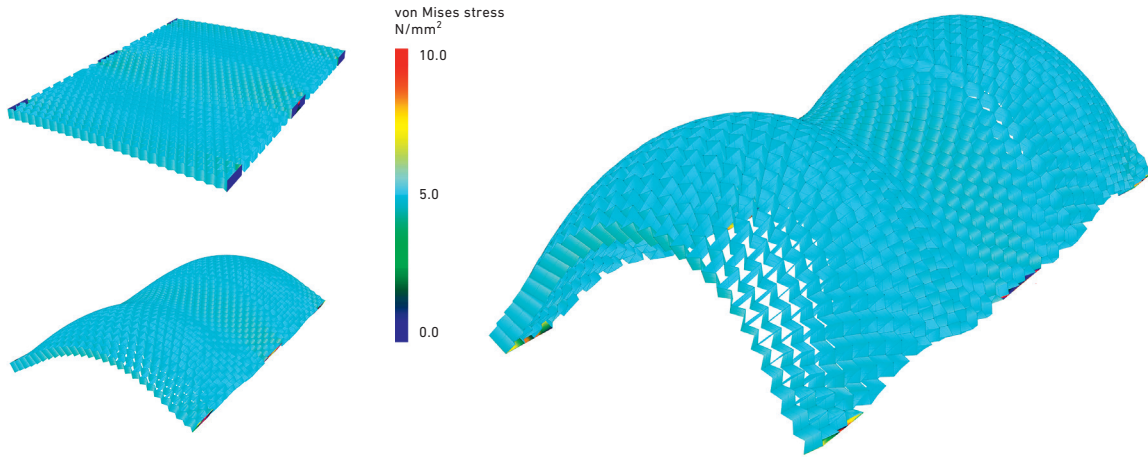
FIG. 6.32

Von Mises stress plot of the form-finding of the Downland test case

which obviously add a layer of complexity to the system. It is still a perfect case to test how the embedded approach performs and its validity. For consistency with the results seen in the case of the torus, the size of the two geometries are comparable. The analysed geometry of the Downland gridshell measures 50 cm x 150 cm. The material parameters employed for the simulation are the same as the ones of the torus and reflect the same A95 Shore material used for the 3d-printed prototypes.

The pattern is generated following the methodology explained in the previous sections of this chapter. In the first place, the flattened outline of the master surface is populated with hexagonal elements which are then modified to interpolate the values of Gaussian curvature derived from the base surface. This is visible in Fig. 6.32a. The pattern is then extruded in the vertical direction for 1 cm, and the cells walls are given a thickness of 1 mm. With this setup the structure is then meshed using five rows of finite elements in the vertical direction per cell wall. The flat pattern is then simulated by applying a horizontal support displacement at the marked areas seen in Fig. 6.32. In this case it was not necessary to use the elastic cable approach as the displacement path of the supports is clearly defined by the geometry of the structure. As the geometry presents a linear axis of symmetry, the supports are constrained to move perpendicularly with respect to this line. The definition of the motion of actuation is therefore very straightforward to define.

In Fig. 6.32 the results of the form-finding for the Downland gridshell pattern are depicted. The geometry shows two positively curved bays of the shell bridged by the intermediate transition zone with negative Gaussian curvature. From the simulation geometry in Fig. 6.32c, it can be seen that the initial base surface is well approximated by the generated cellular pattern. Compared to the results of the torus, the transition between the two areas is less critical here, as

the stress values in the elements are lower. Even in this case the von Mises stress plot is even and constantly spread over the elements of the structure. This means that under form-finding the elements of the pattern react more or less equally to the support displacement. Stress concentrations are found in proximity of the supports as in this area the nodes of the structure are forced into shape by a rigid displacement. Despite these minor variations in terms of peak material stress, the differences between the two test cases are negligible.

Concerning the simulation process, to make sure that the entire structure buckles in the correct direction, either a slight precambering is required or in alternative the application of deadload in the direction that helps the deformation to take place. For the Downland test case the latter method was sufficient to provide enough eccentricity in the elements to follow the correct path of actuation, as opposed to the torus which, due to its complexity, had to be modelled with a global precambering of the pattern.

6.6 Results assessment

The geometries extracted from the simulation models were compared to determine the deviation from the base surfaces. This is done by measuring the distance of the mesh central nodes of each cell wall from the surface. The results are reported in absolute deviation percentage compared against the maximum size of the geometry's bounding box.

In the case of the torus, a comparison between the simulated geometry and the base surface (Fig. 6.33) highlights the errors and deviation between the two models. The heatmap in Fig. 6.33 shows that the maximum deviation between the two geometries reaches almost 10% of the total size of the model. Considering the experimental nature of the developed method and the uncertainties deriving from the pattern generation, as well as deviations due to numerical discretisation, the error between the models is definitely acceptable. The two models present a very low geometrical deviation and are almost coincident. This confirms that the developed embedded approach method and the Finite Element simulations adequately capture the elastic behaviour of the graded cellular core, guaranteeing that the results are consistent with the real, physical behaviour.

Looking at the base surface of the torus and comparing this with the geometry of the simulation highlights a series of important aspects that were not captured so far. The maximum deviation between the two models is concentrated at the seam of the donut where the open edges meet. This is due to

FIG. 6.33

Plot of the percentage of deviation between the base surface and the simulated geometry of the torus

Deviation percentage

10%

5%

0%
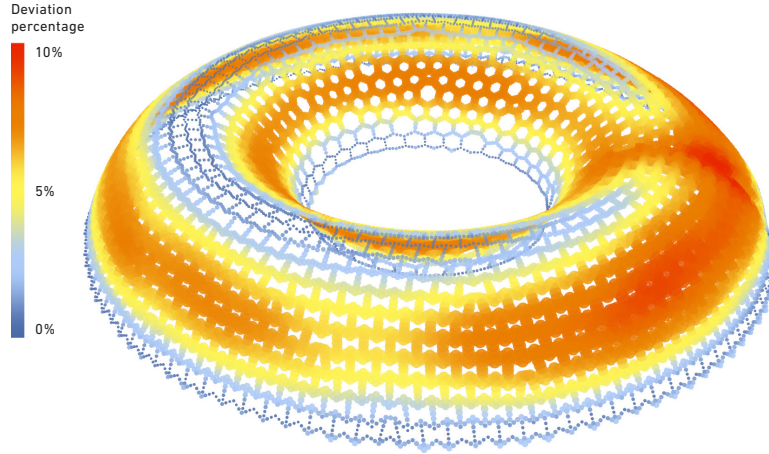
the fact that free edges are not entirely constrained into the final shape as the surrounding elements around those areas are missing. Therefore the edges are free to spring back elastically. This effect can be compensated by pulling together the edges via elastic cables in a second simulation step. In the case of the simulations run for the torus in Fig. 6.33, this was omitted, hence the higher deviation from the base surface in that zone. Higher values of divergence between the two models can also be recognised in the internal anticlastic part of the torus. A closer analysis of this area of the bent model shows that the Gaussian curvature is less pronounced than expected. This fact is imputable to the slightly higher stiffness that the regular honeycomb has in comparison to the inverted honeycomb pattern. Focusing on the axial stretching simulation tests reported in the diagrams of Fig. 6.23 and Fig. 6.22 we recognise that the sum of the support reactions in the first graph and the eigenvalues in the latter indicate that the regular honeycomb is slightly stiffer compared to the other two, despite the support displacement being the same for all structures. To achieve a smoother transition of stiffness values between the two patterns, either a reduction of density would be required or alternatively a reduction of cross-section of the cells walls. In this way a higher degree of control over the bending behaviour of the individual areas of the pattern can be exerted. Moreover, by bending the pattern through a simple support displacement, the configuration that is achieved in this way closely follows the elastica rather than a perfect circular arch, i.e. the curvature changes throughout the development of the cross-section instead of staying constant. From the printed specimens in Fig. 6.15 it can be seen that the zero Poisson pattern indeed presents a deformed shape which resembles the elastica curve. To steer the radius of curvature along the principal direction of bending, it would be necessary to further refine the pattern by taking into account the bending stiffness of the individual

Deviation
percentage

10%

5%

0%
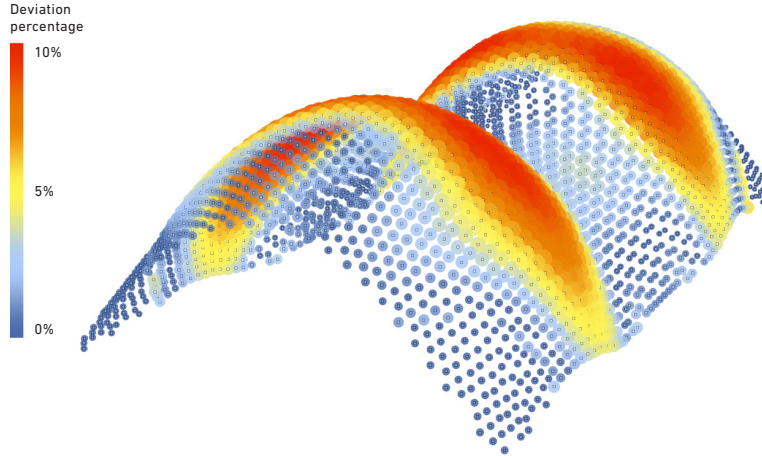
FIG. 6.34

Plot of the percentage of deviation
between the base surface and the
simulated geometry of the Down-
land test case

areas and modifying accordingly. In alternative, the principal
curvature can be controlled by placing a series of internal lin-
ear actuators which force the geometry in the correct place.
Although this strategy was not explored further, it could easily
solve the problem of differential curvature along the develop-
ment of the structural surface. The areas corresponding to the
support edges of the donut are perfectly coincident with the
base surface as the actuation of the structure forces the pat-
tern exactly into shape. On the other hand, if the pattern is
not designed correctly the constraining effect on the supports
might induce unwanted high stress concentrations. In general
this can be avoided by choosing the appropriate pattern distri-
bution to minimise the straining effects on the cells.

The deviation map for the Downland model is shown
in Fig. 6.34. The major deviation from the base surface is
highlighted in the graph and reaches a maximum value of 10%
the total length of the geometry. The areas of maximum devi-
ation are mainly concentrated between the transitioning area
of the two patterns and the unconstrained edges. This was
also noticed in the case of the torus, where the free edges tend
to spring back elastically. As the Downland geometry presents
two free edges at its extremes, a necessary modification to
compensate the local deviation in that area would require a
rigid edge beam to restore the correct position. Despite these
zones of geometrical variation between the two models, even
in this case the maximum deviation is still within acceptable
limits. Contrary to the torus test case, the curvature of the
Downland model in the direction of bending is not constant,
but it rather follows more closely the natural configuration
that the patterns assume under constant support displace-
ment. For this reason the deviation from the ideal surface is
concentrated at the transition between the two areas of dif-
ferent Gaussian curvature, as the curvature in the principal
direction is well replicated by the bending process.

The embedded approach for bending-active plate-based systems developed as part of this research was tested for two ideal study cases which present a challenging geometry due to the smooth Gaussian curvature transition between different areas of the surface. The simulation methods employed for the analysis of large elastic deformations of these structures has been proven to be adequate to capture the geometrical changes in the elements and the stress levels induced in them. From the analysis of the deviation from the base surface, the major areas of divergence between the two models were highlighted. A series of observations were made to explain the nature of these errors and potential corrections to the method were suggested with the aim of further improving the embedded approach presented. Future developments of the process would include further material prototyping to test different kinds of geometries and the generation strategy of the cellular patterns. An important aspect which was already mentioned in previous chapters is the necessity to stiffen the cores due to their flexibility. This is an inherent contradiction that plagues all types of structural systems which employ large deformations as the main form-giving method. For the flexible cellular cores presented here, the most obvious stiffening method would be the lamination of both sides to produce stiff, double curved sandwich structures. This aspect was not treated in this work, although further developments would necessary require detailed research in the behaviour of laminated flexible cores. In terms of fabrication, further research should concentrate on improving the scale of the systems to test the structural and mechanical behaviour of the structures at larger scales. To the knowledge of the author, at the time of writing this kind of approach to functionally graded cellular structures with complex bending behaviour still has not been extensively researched nor put into practice. The design explorations conducted here served as a starting point for future developments which will hopefully lead to new and exciting applications.

7. Conclusions and future directions

This thesis has explored different strategies for the induction of curvature through the means of elastic bending of plate-based systems. The essential aspects that were covered in the development of this work focussed on the relationship between geometry and structure and how these influence and complement each other. Geometry lies at the core of engineering and architecture, and is the fundamental basis from which scholars of these disciplines must depart to be successful in their research and exploration. Owing to this idea, geometry permeates the spirit of this work, and is accompanied in parallel by the study of structures as real manifestations of abstract entities. Structures are physical objects described by geometry, and geometry can be manipulated through structures if one comprehends how to make this happen. This synthesis summarises the spirit of this work and sets the main objectives for the development of the thesis.

The work opened with an overview of structural systems that employ form-finding as a form-giving strategy. Embedded in the context of engineering and architectural pioneers that realised structures through the means of physical form-finding and applied geometry, the introduction of this thesis offered a review on fundamental experiences of the past and more recent examples mostly relevant to the development of this work. Bending-active structures are introduced discussing the genesis of the terminology and recent experiences, especially conducted in academic environments that spawned the field of research. The nature and scope of bending-active structures as systems that employ bending, and more in general large deformations to induce form were discussed along with existing classifications. A further distinction was drawn by focusing on the dimension of the elements that compose the structure. In this way it was possible to identify 1d and 2d systems, with bending-active structures made of combinations of bidimensional elements being the objective of this research. This led to the definition of bending-active plates, as flat 2d elements are commonly known as plates in engineering. Through this classification the scope of the work was defined. Concentrating on recent prototypes and experiences in building construction that employed actively bent thin plates or strips, a further distinction was proposed based on the type of mechanical action that is used in those cases to induce form.

In this way three conceptual strategies were identified, namely pure bending, torsion and multidirectional bending. These actions completely define the deformation space of bending-active structures, where bending is used here as a broader term to speak about structural systems that actively employ the large deflections of their elements to achieve form.

In the continuation of the work, fundamental quantities known from the differential geometry of surfaces were reviewed. A particular focus was set on a central quantity used to describe the shape of surfaces embedded in space, i.e. the Gaussian curvature. The Gaussian curvature plays a significant role in the further development of this thesis. The common theme that ties the chapters together is, in fact, the Gaussian curvature and ways to induce it by means of elastic bending of plate elements. The centrality of this quantity was deemed so important that in the section dedicated to the differential geometry of surfaces the full derivation of it was presented. By doing so fundamental concepts from differential geometry are introduced by adopting the tensor notation commonly used in the exposition of such topics. The derivation of the mathematical formalism of the Gaussian curvature is then completed by discussing the concept of isometric transformations and their privileged role in the large deformation of plates. It was seen that the plane only possess three isometries, namely the cylinder, the cone and a third class known as tangent developables, and that these are the only configurations into which a plane can be transformed without exceeding the material's stress limits. The proof of this was given by presenting Gauss' Theorema Egregium, which says that bending leaves lengths on the surface unaltered, and conversely that a change in Gaussian curvature can only be achieved by stretching of the material fibres. The chapter on differential geometry is then completed by introducing concepts from a fairly new branch of mathematics, namely 'discrete differential geometry'. Some important tools from discrete differential geometry were presented, which were later used in the further developments of this thesis to analyse the discrete curvature of mesh elements derived from the numerical form-finding simulations.

The introduction to the geometry of surfaces is then completed by the discussion on the mechanics of plates. Here, a strong connection to the previous chapter on geometry is sought in order to close the gap between the mechanics and the geometry of plates. An introductory distinction between plate bending and membrane stretching is made at the beginning of the chapter to explain how the behaviour of a plate changes and is influenced by these actions. The classic theory of plates is then presented, along with the assumptions and

fundamental quantities that are involved in the calculation of plates in the membrane and bending approximation. The classic theory of plates is then completed by introducing the nonlinear treatment of plates for large deflections, in order to highlight an important aspect that is otherwise missed in the classic theory. The results demonstrated through Gauss' Theorema Egregium are shown to have their mechanical counterpart in the nonlinear description of plates. It is shown here that the Gaussian curvature enters the equations of mechanics in the nonlinear description of plates in the membrane approximation. This confirms that, also from a mechanical point of view, a change in Gaussian curvature is possible exclusively through stretching of the material fibres of the surface. Bending, as seen previously, leaves this quantity unchanged. The chapter on the mechanics of plates is then completed by discussing a few concepts on numerical simulations and specifically the Finite Element Method. A brief introduction to the method is followed by a discussion on the additions made by the author to improve the simulation routines and the calculation time for the analysis of large geometrically nonlinear systems.

Chapter 5 presented the form conversion approach that was specifically devised as part of this research. The limits on the deformation of plates was highlighted in the previous chapters and showed that other strategies are necessary to induce Gaussian curvature in the system. The form conversion approach provides a general method for the discretisation and construction of bending-active plate based structures. The main ideas guiding this method showed that the continuity of the surface has to be partially sacrificed in order to be able to build a double curved surface using exclusively flat strips of material. By manipulating the topology of the base surface, the form conversion approach guarantees the bendability of the elements and in this way the ability for two-dimensional elements to span multiple directions and therefore cover the whole space. The validity of the developed approach was tested on several geometries, and it demonstrated to be applicable to any surface, as long as the bending and torsion of the elements are kept within the material parameters. A series of prototypes were realised to test the form conversion approach at bigger scales. These have shown to scale well in terms of deformation of the elements, as at architectural scale the curvatures are generally less pronounced than at model scale. Nonetheless, the inherent contradiction of bending-active structures, which need to have slender elements to be able to be bent into shape at the expense of the structural stability, is still not resolved. This can be partially compensated by the coupling of multiple elements to create multi-layered

structures as it was tested in some of the realised prototypes. The geometries obtained through the form conversion method were tested numerically to assess the structural potential of the structures created in this way. The simulations showed that the introduction of discontinuities takes a toll over the capacity of the structure, partially weakening it due to the interruption of the force flow in the elements. This trade-off is compensated by the ease of construction that the method ensures and the ability of building double curved shell structures out of flat, off-the-shelf materials.

The form conversion approach still showed its limitations in terms of material formability. The elements that compose a form conversion shell are limited to axial bending and torsional effects at the most, meaning that the double curvature of the base surface is artificially created by approximation. To overcome these limitations, another strategy was devised and aptly called embedded approach. This refers to the fact that the behaviour of the structure is directly encoded in its design. Belonging to the class of metamaterials, the embedded approach exploits the deformation properties of cellular structures to closely replicate the curvature of the base surface. The chapter relative to the embedded approach demonstrated these phenomena by showing how different values of Gaussian curvature can be derived by interpolating between different patterns. This surprising feature of graded cellular structures offered a valuable alternative to the question on how to couple bending and Gaussian curvature. By considering the cellular cores as an assembly of vertically oriented plates, the mechanics of the global pattern is nothing else but the sum of the mechanical response of individual plate elements. The embedded approach was tested both physically and numerically. The physical tests were created using 3d-printing technology as the intricacy of the structural patterns required advanced manufacturing techniques to overcome this complexity. The tested geometries showed how, indeed, the Gaussian curvature can be tailored to meet the needs of the designer by adjusting the pattern configuration. Despite requiring further improvement, the method demonstrated its validity and potential for future applications.

The form conversion approach has demonstrated its universal applicability and versatility, as the complexity of the base surface does not affect the generation of the decomposed pattern. Limitations mainly derive from the maximum thickness of the material that needs to necessarily be thin enough to allow the bending deformation to take place. Future developments should point towards fabrication and assembly strategies to couple multiple layers together and therefore ensure a composite action of the structure. Only in this way the

compromise on the material's cross-section and the structural capacity might be resolved. The realised prototypes attempted to provide an answer to this riddle, showing that indeed this might be the best strategy to overcome these limitations. Nonetheless, further work is definitely required to improve the quality of the connections and their fabrication. Assembly also plays a central role in the development of the form conversion approach. Considering that a higher number of elements better approximate the base surface, it is clear that scaling up the system might require substantial work to get the whole structure properly built. Research on automated assembly pipelines are currently under development on behalf of various research communities. The structural types generated through the form conversion approach lend themselves well to this kind of explorations, and automated assembly of full scale structures is definitely foreseeable in the near future. The form conversion approach has shown to scale well with an increase in size, as it is only dependent on the underlying geometry. Still, scalability of structures is notoriously known to be a rough topic in engineering circles, and this case makes no exception. Further studies on scalability will be required if the structural systems are meant to increase in size in future application scenarios.

The embedded approach took an alternative take on the topic of bending and form generation. The fascinating deformation abilities of cellular structures have provided a new and fresh approach to the quest of wrapping a planar surface over a double curved surface. Applications for such a technology are numerous, ranging from morphing structures for aerospace engineering to smart building components in building construction. In this work only the surface of a very vast field has been scratched, mainly concentrating on the effects rather than the applications. Future developments will definitely point towards this direction, devising application scenarios that were yet unthinkable of. The topic was developed from a point of view that only recently has started showing growing interest on behalf of the research community. Further improvements on the theory are needed to provide a solid pipeline between the definition of the base surface, the generation of the pattern and the control of the stiffness over the gradient core. The ideas presented in the chapter on the embedded approach partially serve as a base to provide a starting point for future developments. The steps involved in the design and generation of the patterns require further investigation to assess the validity of the method, not only experimentally as has been done in this work, but also theoretically by considering more intimate mathematical aspects that were disregarded in the development of the thesis. The surface unfolding is the

first of those steps in need of improvement, as the structural implications of choosing an unwrapping algorithm over another have not been touched upon in this work. The pattern generation might benefit from more solid mesh generation algorithms currently being actively developed in various fields. Fabrication constraints play a crucial aspect in the realisation of proper prototypes to test the validity of the ideas presented. 3d-printing has shown its advantages in dealing with complex geometries, but the size limits are quickly reached in that case. Other manufacturing technologies are required to perform the scale jump that would bring the embedded approach towards impressive future applications.

This work has dealt with the limits of bending-active structures in terms of shape inducing potential. The geometrical and mechanical motivations were demonstrated in the introductory chapters of the thesis and served to establish a solid basis onto which the further developments were built. Two novel approaches to bending-active plate-based systems were devised and presented. Both methods aim to overcome the limitations seen so far on the formability of plates, and by doing so open up the possibilities for these structural typologies to future applications. The principal aim of this work was to free the design of bending-active structures from the limiting constraints of the material's deformation capabilities, devising strategies that could compensate these aspects and by doing so providing a universal method that can be applied to a larger spectrum of double curved surfaces. Improvements are still necessary to overcome aspects that were only briefly discussed in the development of the thesis. Nonetheless, this thesis was conceived as a departing point rather than the concluding chapter of a topic. In this spirit, this work is meant to be a launching pad for future research yet to come.

Bibliography

Adriaenssens, S., Block, P., Veenendaal, D., Williams, C. (2014). *Shell Structures for Architecture: Form Finding and Optimization.* Routledge, London, New York.

Ajdari, A., Nayeb-Hashemi, H., Vaziri, A. (2011). *Dynamic crushing and energy absorption of regular, irregular and functionally graded cellular structures.* International Journal of Solids and Structures, 48:506-516.

Akleman, E., Chen, J., Gross, J.L. (2010). *Paper-Strip Sculptures.* Proceedings of the IEEE International Conference on Shape Modelling and Applications.

Audoly, B., Pomeau. Y. (2010). *Elasticity and Geometry: From Hair Curls to the Non-Linear Response of Shells.* Oxford University Press, Oxford, New York.

Bathe, K.J. (1996). *Finite Element Procedures.* Prentice Hall, Upper Saddle River, New Jersey.

Bechert, S., Knippers, K., Krieg, O.D., Menges, A., Schwinn, T., Sonntag, D. (2016). *Textile Fabrication Techniques for Timber Shells: Elastic Bending of Custom-Laminated Veneer for Segmented Shell.* Advances in Architectural Geometry 2016, 154-169.

Bischoff, M. (2012). *Lectures on nonlinear Finite Element Analysis.* University of Stuttgart.

Bischoff, M., Wall, W.A., Bletzinger, K.U., Ramm, E. (2004). *Encyclopedia of Computational Mechanics. Volume 2: Solids and Structures.* John Wiley & Sons, New York.

Bletzinger, K.U. (2016). Private conversation.

Block, P., DeJong M., Ochsendorf, J. (2006). *As Hangs the Flexible Line: Equilibrium of Masonry Arches.* Nexus Network Journal, Vol. 8, No. 2, 9.

Bobenko, A.I., Schröder, P., Sullivan, J.M., Ziegler, G.M., (2008). *Discrete differential geometry.* Birkhäuser, Basel, Berlin.

Chilton, J.C., Isler, H. (2000). *Heinz Isler.* Thomas Telford, London.

Crane, K. (2015). *Discrete Differential Geometry: An Applied Introduction.* Course notes

Cui, L., Kiernan, S., Gilchrist, M.D. (2009). *Designing the energy absorption capacity of functionally graded foam materials.* Material Science and Engineering A, 507:215-225.

Driscoll, T.A., Trefethen, L.N. (2002). *Schwarz-Christoffel Mapping.* Cambridge Monographs on Applied and Computational Mathematics, Cambridge University Press, Cambridge.

Engel, H. (1999). *Tragsysteme – Structure Systems.* Hatje Cantz Verlag, Stuttgart.

Evans, K.E., Alderson, A. (2000). *Auxetic Materials: Functional Materials and Structures from Lateral Thinking!.* Advanced Materials, 12, No. 9, 617-628.

Evans, K.E., Nkansah, M.A., Hutchinson, I.J., Rogers, S.C. (1991). *Molecular Network Design.* Nature, 353, 124.

Farahi, B. (2016). *Caress of the Gaze: A Gaze Actuated 3D Printed Body Architecture.* Proceedings of the 36th Annual Conference of the Association for Computer Aided Design in Architecture (ACADIA) 2016, Ann Arbor, 352-361

Felippa, C. (2012). *Nonlinear Finite Element Methods.* Lecture material, University of Colorado, Boulder.

Föppl, A. (1907). *Vorlesungen über technische Mechanik.* B.G. Teubner Verlag, Leipzig, 5, p. 132.

Fuller, R.B. (1959). *Self-Strutted Geodesic Plydome.* U.S. Patent 2,905,113, issued September 22, 1959.

Galilei, G. (1638). *Discorsi e dimostrazioni matematiche, intorno à due nuove scienze.* Appresso gli Elsevirii, Leiden.

Garlock, M.E.M., Billington, D.P. (2008). *Félix Candela: Engineer, Builder, Structural Artist.* Yale University Press, New Haven.

Germain, S. (1826). *Remarques sur la nature, les bornes et l'étendue de la question des surfaces élastiques, et équation générale de ces surfaces.* Imprimerie de Huzard-Courcier, Paris.

Gibson, L.J., Ashby, M.F. (1999). *Cellular solids: structure and properties.* Cambridge University Press, Cambridge.

Gibson, L.J., Ashby, M.F., Harley, B.A. (2010). *Cellular materials in nature and medicine.* Cambridge University Press, Cambridge.

Greaves, G.N., Greer, A.L., Lakes, R.S., Rouxel, T. (2011). *Poisson's Ratio and Modern Materials.* Nature Materials, 10:823-837.

Green, A.E., Zerna, W. (1968). *Theoretical elasticity – 2nd edition.* Clarendon P, Oxford.
Grima, J.N., Caruana-Gauci, R., Attard, D., Gatt, R. (2012). *Three-dimensional cellular structures with negative Poisson's ratio and negative compressibility properties.* Proceedings of the Royal Society A: Mathematical, Physical and Engineering Science, 468:3121-38.

Happold, E., Liddell, W.I., (1975). *Timber lattice roof for the Mannheim Bundesgartensschau.* The Structural Engineer, Volume: 53, Number 3.

Hernandez, E.A.P., Hu, S., Kunga, H.W., Hartl, D., Akleman, E. (2013). *Towards Building Smart Self-Folding Structures.* Computers & Graphics, Volume 37, Issue 6, 730-742.

Heyman, J. (1998). *Structural Analysis: A Historical Approach.* Cambridge University Press, Cambridge.

Harris, R., Romer, J., Kelly, O., Johnson, S. (2003). *Design and Construction of the Downland Gridshell.* Building Research and Information, 31 (6), 427-454.

Hou, Y., Tai, Y.H., Lira, C., Scarpa, F., Yates, J.R., Gu, B. (2013). *The bending and failure of sandwich structures with auxetic gradient cellular cores.* Composites: Part A, 49:119-131.

Ju J., Summers J.D. (2011). *Compliant hexagonal periodic lattice structures having both high shear strength and high shear strain.* Material Design, 32:512-524.

Kirchhoff, G.R. (1850). *Über das gleichgewicht und die bewegung einer elastischen scheibe.* Journal für die reine und angewandte Mathematik, 40:51–88.

Kirugulige, M., Kitey, R., Tippur, H. (2005). *Dynamic fracture behavior of model sandwich structures with functionally graded core: a feasibility study.* Composite Science and Technology, 65:1052-1068.

Krieg, O.D., Menges, A. (2013). *Prototyping robotic production: development of elastically bent wood plate morphologies with curved finger joint seams.* Rethinking Prototyping, Proceedings of the Design Modelling Symposium, Berlin.

Kshetrimayum, R.S. (2004). *A brief intro to metamaterials.* IEEE Potentials – Volume: 23, Issue 5.

Knippers, J., Cremers, J., Gabler, M., Lienhard, J. (2011). *Construction Manual for Polymers + Membranes: Materials, Semi-Finished Products, Form Finding, Design.* Birkhäuser, Basel, Berlin.

Knippers, J., Scheible, F., Oppe, M., Jungjohann, H. (2012). *Bio-inspired Kinetic GFRP-façade for the Thematic Pavilion of the EXPO 2012 in Yeosu.* Proceedings of the International Association for Shell and Spatial Structures (IASS) Symposium 2012, Seoul, South Korea.

Lakes, R. (1987). *Foam structures with a negative Poisson's ratio.* Science, 235, 1038-1040.

La Magna, R., Schleicher, S., Knippers, K. (2016). *Bending-Active Plates: Form and Structure.* Advances in Architectural Geometry 2016, 170-186.

Lienhard, J., Schleicher, S., Knippers, J. (2011). *Bending-active Structures – Research Pavilion ICD/ITKE.* Proceedings of the International Association for Shell and Spatial Structures (IASS) Symposium 2011, London, United Kingdom.

Lienhard, J., Alpermann, H., Gengnagel, C., Knippers, J. (2013). *Active Bending, A Review on Structures where Bending is used as a Self-Formation Process.* International Journal of Space Structures, 28:187-196.

Lienhard, J. (2014). *Bending-Active Structures – Form-finding strategies using elastic deformation in static and kinetic systems and the structural potentials therein.* Ph.D. Dissertation, University of Stuttgart.

Lienhard, J., La Magna, R., Knippers, J. (2014). *Form-Finding Bending-Active Structures with Temporary Ultra-Elastic Contraction Elements.* Mobile and Rapidly Assembled Structures IV, DOI: 10.2495/mar140091.

Lim, T.C. (2002). *Functionally graded beam for attaining Poisson-curving.* Journal of Materials Science Letters, 21:1899:1901.

Lira, C., Scarpa, F. (2010). *Transverse shear stiffness of thickness gradient honeycombs.* Composites Science and Technology, 70:930-936.

Loukaides, E.G., Seffen, K.A. (2015). *Multistable grid and honeycomb shells.* International Journal of Solids and Structures, 59:46-57.

Love, A.E.H. (1888). *On the small free vibrations and deformations of elastic shells.* Philosophical transactions of the Royal Society, London, vol. A, 17:491–549.

Malek, S., Williams, C. (2013). *Structural Implications of using Cairo Tiling and Hexagons in Gridshells.* Proceedings of the International Association for Shell and Spatial Structures (IASS) Symposium 2013, Wroclaw, Poland.

Mansfield, E.H. (1964). *The bending and stretching of plates.* Pergamon Press, Oxford.

McGuire, W., Gallagher, R.H., Ziemian, R.D. (2000). *Matrix Structural Analysis – Second Edition.* Wiley & Sons, New York.

Menges, A. (2012). *Material Computation: Higher Integration in Morphogenetic Design.* Architectural Design 82, 2: 14–21.

Meyer, M., Desbrun, M., Schröder, P., Barr, A.H. (2003). *Discrete Differential-Geometry Operators for Triangulated 2-Manifolds.* Visualization and Mathematics III, 35–57. Springer, Berlin, Heidelberg.

Mindlin, R.D. (1951). *Influence of rotatory inertia and shear on flexural motions of isotropic, elastic plates.* ASME Journal of Applied Mechanics, 18:31–38.

Mott, P.H., Roland, C.M. (2013). *Limits of Poisson's ratio in isotropic materials – general result for arbitrary deformation.* Physica Scripta, 87.

Naicu, D.I. (2016). *Theoretical and numerical investigation of the equilibrium shape of curved strips and tapered rods.* Ph.D. Dissertation, University of Bath.

Otto, F. (2005). *Frei Otto: Complete Works: Lightweight Construction, Natural Design.* Edited by Winfried Nerdinger, Birkhäuser, Basel, Berlin.

Pagitz, M., Lamacchia, E., Hol, J.M.A.M. (2012). *Pressure-actuated cellular structures.* Bioinspiration & Biomimetics, 7:1-19.

Pagitz, M., Bold, J. (2013). *Shape-changing shell-like structures.* Bioinspiration & Biomimetics, 8:1-11.

Pietroni, N., Tonelli, D., Puppo, E., Froli, M., Scopigno, R., Cignoni, P. (2014). *Voronoi Grid-Shell Structures.* ACM Transactions on Graphics, 1:10.

Pottmann, H., Schiftner, A., Bo, P., Schmiedhofer, H., Wang, W., Baldassini, N., Wallner, J. (2008). *Freeform surfaces from single curved panels.* ACM Transactions on Graphics, 27:3.

Pressley, A. (2012). *Elementary Differential Geometry – 2nd edition.* Springer, London, New York.

Reissner, E. (1945). *The effect of transverse shear deformation on the bending of elastic plates.* ASME Journal of Applied Mechanics, 12:68-77.

Schleicher, S., Lienhard, J., Poppinga, S., Speck, T., Knippers, J. (2014). *A methodology for transferring principles of plant movements to elastic systems in architecture.* Computer-Aided Design, 60:105-117.

Schönbrunner, A., Haberbosch, N., La Magna, R., Schleicher, S., Lienhard, J., Knippers, K. (2015). *Design strategies for bending-active plate structures out of multiple cross-connected layers.* Proceedings of the International Association for Shell and Spatial Structures (IASS) Symposium 2015, Amsterdam, Holland.

Snyder, J.P. (1989). *Album of Map Projections, United States Geological Survey Professional Paper.* United States Government Printing Office.

SOFiSTiK (2013a). *Benchmark Example No. 7: Large Deflection of Cantilever Beams I.*

SOFiSTiK (2013b). *Benchmark Example No. 8: Large Deflection of Cantilever Beams II.*

Struik, D.J. (1988). *Lectures on classical differential geometry.* 2nd edition, Dover, New York.

Ting, T.C.T., Chen, T. (2005). *Poisson's ratio for anisotropic elastic materials can have no bounds.* The Quarterly Journal of Mechanics and Applied Mathematics, 58 (1), 73-82.

Tonelli, D., Pietroni, N., Puppo, E., Froli, M., Cignoni, P., Amendola, G., Scopigno, R. (2016). *Stability of Statics Aware Voronoi Grid-Shells.* Engineering Structures, 116:70-82.

Ventsel, E., Krauthammer, T. (2001). *Thin Plates and Shells. Theory, Analysis and Applications.* Marcel Dekker Inc., New York, Basel.

Vincent, J.F.V. (2002). *Survival of the cheapest.* Materials Today - Volume 5, Issue 12, 28–41.

von Kármán, T., (1910). *Festigkeitsproblem im Maschinenbau.* Encyklopädie der mathematischen Wissenschaften, IV, 311–385.

Williams, C. (2014). *Appendix B - Differential geometry and shell theory.* In: Adriaenssens, S., Block, P., Veenendaal, D., Williams, C. *Shell Structures for Architecture: Form Finding and Optimization.* Routledge, London, New York, 281-289.

Xing, Q., Esquivel, G., Akleman, E., Chen, J. (2011). *Band Decomposition of 2-Manifold Meshes for Physical Construction of Large Structures.* Proceedings of the Siggraph Conference, Vancouver.

List of Figures

Chapter 4

Chapter 5

Chapter 6

160

Curriculum Vitae

since 2016   Freelance engineer

2016 – 2017   University of the Arts Berlin, Germany

2015   Artist in Residence at Autodesk Pier 9, San Francisco, California, USA

2012 – 2015   DAAD Scholarship (Deutscher Akademischer Austauschdienst)

2011 – 2016   University of Stuttgart, Germany
Research associate and doctoral candidate at the
Institute of Building Structures and Structural Design (ITKE)
Thesis advisor: Prof. Dr.-Ing. Jan Knippers

2010 – 2011   Studio on-a, Barcelona, Spain

2008   Studio Jakob+MacFarlane, Paris, France

2004 – 2005   Karlsruhe Institute of Technology, Germany
Visiting student

2002 – 2009   University of Bologna, Faculty of Engineering, Italy
Dipl.-Ing. Structural Engineering

1982   Born in Verona, Italy